PIEZOELECTRIC MEMS DEVICES IN CMOS-COMPATIBLE PLATFORM

by

Yanbo He

A Dissertation

Submitted to the Faculty of Purdue University

In Partial Fulfillment of the Requirements for the degree of

Doctor of Philosophy

School of Electrical and Computer Engineering

West Lafayette, Indiana

May 2021

THE PURDUE UNIVERSITY GRADUATE SCHOOL
STATEMENT OF COMMITTEE APPROVAL

Dr. Dana Weinstein, Chair

School of Electrical and Computer Engineering

Dr. Sunil Bhave

School of Electrical and Computer Engineering

Dr. Dimitrios Peroulis

School of Electrical and Computer Engineering

Dr. Jeffrey Rhoads

School of Mechanical Engineering

Approved by:

Dr. Dimitrios Peroulis

To my parents

ACKNOWLEDGMENTS

First of all, I would like to express my deepest gratitude to my research advisor, Prof. Dana Weinstein for her endless patience, support, and encouragement over my Ph.D. years. I would like to thank her for introducing me into the world of MEMS and microfabrication, for always standing by my side during ups and downs, for providing constructional technical support for all the research topics, and for being instructive for the decisions I make not only in all my researches but also in my career. I would also like to thank my committee members: Prof. Sunil Bhave, Prof. Dimitrios Peroulis, and Prof. Jeffrey Rhoads for your time and efforts in providing helpful input in my research and this thesis.

A great number of my Ph.D. works are accomplished by collaborating with Kilby labs at Texas Instruments. Especially, I would like to express my sincere gratitude to Dr. Bichoy Bahr, who has great passion and knowledge. I am lucky to have his selfless support, insightful discussions on the research project, and tremendous help in my career. It is also a great privilege to work with Swaminathan Sankaran, Baher Haroun, Benjamin Cook, Huiyao Chen, and Ernest Ting-Ta Yen. I thank them for all the fruitful discussions and support during my internship at TI.

Also, my research work will not be possible without the support from my colleagues in HybridMEMS and OxideMEMS labs. Particularly, I would like to thank Dr. Shreyas Shah, Dr. Umesh Bhaskar, Chengzi Huang, Imtiaz Ahamed, Jackson Anderson, Udit Rawat, Dr. Pen-li(Ben) Yu, Dr. Mert Torunbalci, Dr. Noah Opondo, Dr. Keivan Asadi, Hao Tian, Yiyang Feng, Boyang Jiang, Sen Dai, Ozan Erturk. I thank them for all the insightful discussions as well as selfless support and friendship over these years.

Additionally, I would also like to thank my collaborators from Prof. Dimitrios Peroulis', Prof. Zhihong Chen's, Prof. Peide Ye's and Prof. Shreyas Sen's research groups, especially Prof. Yi Xuan, Dr. Mengwei Si, Dr. Runqi Zhang, Dr. Wesley Allen, Dr. Abhishek Srivastava and Baibhab Chatterjee for sharing their knowledge and helpful discussions.

Part of my research works is closely related to microfabrication at Purdue Birck nanotechnology center. Therefore, I would also like to thank all the staffs at Birck, especially Xingtao Liu, Michael Bayless, Richard Harlan, Matthew Hayes, Richard Hosler, Dan Hosler, Stephen Jurss, Dave Lubelski, Francis Manfred, Tim Miller, Joon Park, Ron Reger, Bill Rowe, Jeremiah Shepard, Michael Sinanis, Guy Telesnicki, Mary Jo Totten, Jaime Turner, Mark Voorhis,

Justin Wirth, Nancy Black, Rosa Diaz Rivas, Nithin Raghunathan. I thank them for their training and invaluable suggestion on developing my fabrication processes.

I am also grateful to all my classmates and friends outside the lab. I could never imagine myself going through all the hardships without their accompany. I am particularly grateful for Xianwei Li, Dongji Gao, Cong Huang, Xuefeng Bao, Shabnam Ghotbi, Jinhyun Noh, Peng Wu, Shouyuan Huang, Suki Zhang, Chin-Sheng Pang, Chun-li Lo, Shengjiao Zhang, Xiangkai Liu, Liwei Guo, Guanhong Tao.

Last but not least, no words can express my love and gratitude to my parents Dan Chen and Yongcheng He. Without their encouragement, support, and guidance throughout my life, I would never imagine one day I would come to a foreign country and obtain my advanced degree. This work is dedicated to them.

TABLE OF CONTENTS

LIST OF TABLES

LIST OF FIGURES

ABSTRACT

Integrating piezoelectrics with the standard complementary metal-oxide-semiconductor (CMOS) process presents new opportunities for monolithic microelectromechanical systems (MEMS) with scaled size, weight, and power (SWaP). Unlike traditional electrostatic transduction in CMOS platform, piezoelectric actuation allows higher sensitivity and electromechanical coupling, and as such, has been recently adopted by foundries like TSMC and Globalfoundries in their standard CMOS lines for commercial MEMS applications. In this research, a tunable ferroelectric capacitor (FeCAP)-based unreleased RF MEMS resonator is presented, integrated seamlessly in Texas Instruments' 130nm ferroelectric random-access memory (RAM) process. To achieve high-quality factor (Q) of the resonator, acoustic waveguiding for vertical confinement within the CMOS stack is studied and optimized. The FeCAP resonator is demonstrated with fundamental resonance at 703 MHz and Q of 1012. This gives a frequency-quality factor product $f \cdot Q = 7.11 \times 10^{11}$ which is 1.6x higher than the most state-of-the-art Pb(Zr, Ti)O_3 (PZT) resonators. Moreover, ferroelectric poling parameters are investigated to demonstrate bias-dependent pole/zero transitions accompanied by 180° phase shift in multiple mechanical modes of the device. The resonator's Butterworth-Van Dyke (BVD) model is modified to capture this unique switching and frequency-hopping mechanism. The designs are monolithically integrated into solid-state CMOS technology, with no post-processing or release etch step which is typical of other MEMS devices. These novel switchable resonators may have promising applications in on-chip timing, ad-hoc radio front ends, and chip-scale sensors.

In order to best leverage these new CMOS-MEMS resonators for RF signal processing, synchronized clock arrays, and on-chip sensors requiring a network of such resonators working together, we require the ability to route and manipulate mechanical signals within the CMOS stack. At high frequencies of operation, it is particularly important to minimize propagation losses and control the dispersion of elastic waves. Therefore, this research also proposes the design of new acoustic metamaterials in order to localize, guide, and split elastic waves with low dispersion. These designs will be prototyped in an AlN piezoelectric platform for the proof of concept but can translate with small modifications to direct CMOS implementation.

1. INTRODUCTION

1.1 Motivation

Signals can be superimposed upon various types of analog waves, the two most promising and widely used waves are electromagnetic waves and mechanical waves. With high wave velocity and high attenuation in air, it raised challenges for deploying electromagnetic waves in most recent short-distance applications including 5G cellular, infrastructure, or multiple machine-to-machine communication [1], [2]. Compared to their electromagnetic counterparts, mechanical waves have low velocity and low propagation loss in high-quality materials. Mechanical signals can therefore be transmitted, confined, or processed on-chip with short distances. Some examples of the various functions provided by MEMS for mechanical signal processing include: resonators [3]–[7], filters [8]–[11], circulators [12], [13], correlators [14], oscillators [15]–[18], delay lines [19]–[23] etc.

However, one challenge of mechanical signal processing lies in the efficiency of conversion between the electrical and mechanical domains. Complex systems that require multiple processing elements typically use each electromechanical component independently- input and output signals are provided in the electrical domain. Signals are typically transmitted or received via metal wires between components. However, each time when the signal is transferred from one domain to the other, there is unavoidably some inefficiency and therefore energy loss. Instead, to increase the energy efficiency of the overall system, it is desired to reduce the number of conversions – keeping the signal in the mechanical domain for more signal processing steps. Therefore, in this chapter, we will start with assessing some conventional approaches of superimposing analog signals upon mechanical waves.

1.2 Conventional Approach

Mechanical waves have been extensively explored and studied over the past few decades. Generally, depending on the location of the mechanical wave motion, on-chip mechanical waves can be categorized as either bulk acoustic wave (BAW) where the wave is propagating through the entire bulk of the structure, or surface generated acoustic wave (SGAW) [24] where the wave motion is only at the surface.

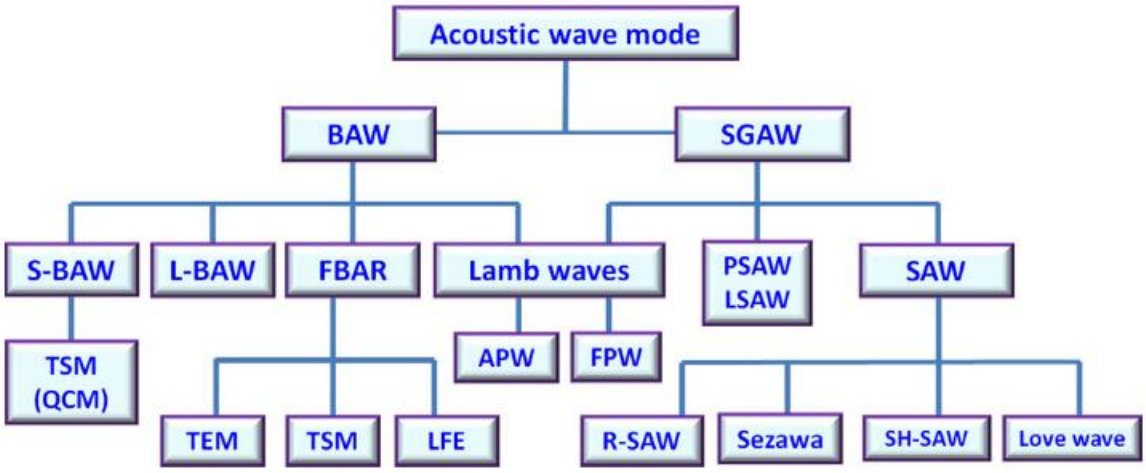

Figure 1.1 Classification of different on-chip acoustic wave modes [24].

As shown in Fig. 1.1, BAW can be further divided into shear BAW (S-BAW), longitudinal BAW (L-BAW), thin-film bulk acoustic wave (FBAR), and lamb waves. Depending on the coupling of the motion along thickness direction with other directions, FBAR can then be further split into thickness extensional mode (TEM), thickness-shear mode (TSM), and lateral field excitation (LFE) mode [24]. As such, SGAW can also be categorized into multiple groups. Except for SAW, other key types include pseudo-surface acoustic waves (PSAW) or leaky SAWs (LSAW). Again, depending on the wave motion on the surface, SAW can be further categorized into Rayleigh SAW (R-SAW), Sezawa mode, Shear-horizontal SAWs (SH-SAWs), and Love wave[24].

Upon the invention of interdigitated transducers (IDT), on-chip acoustic waves can then be actuated and sensed effectively [25]. Depending on the specific wave motion, on-chip mechanical signals can be superimposed and processed through either SAW or BAW. Therefore, in the following subsections, we will review few applications of SAW and BAW in signal processing.

1.2.1 SAW Devices

Surface acoustic waves can be generated on any free surface of the elastic solid, but it was not until 1965 before the first demonstration of SAW transduction using IDTs [25]. One of the major benefits of the SAW-based devices would be the capability of controlling elastic waves using planar structures. In addition, with no releasing or post-processing requirements, it also has

a relatively simple and high-yield fabrication process [26]. Therefore, in the past few decades, SAW transduction has been successfully implemented in 3G and 4G RF front end, especially as RF resonators [27], filters [28], [29], oscillators [30], [31], delay lines [32], waveguides [33], etc.

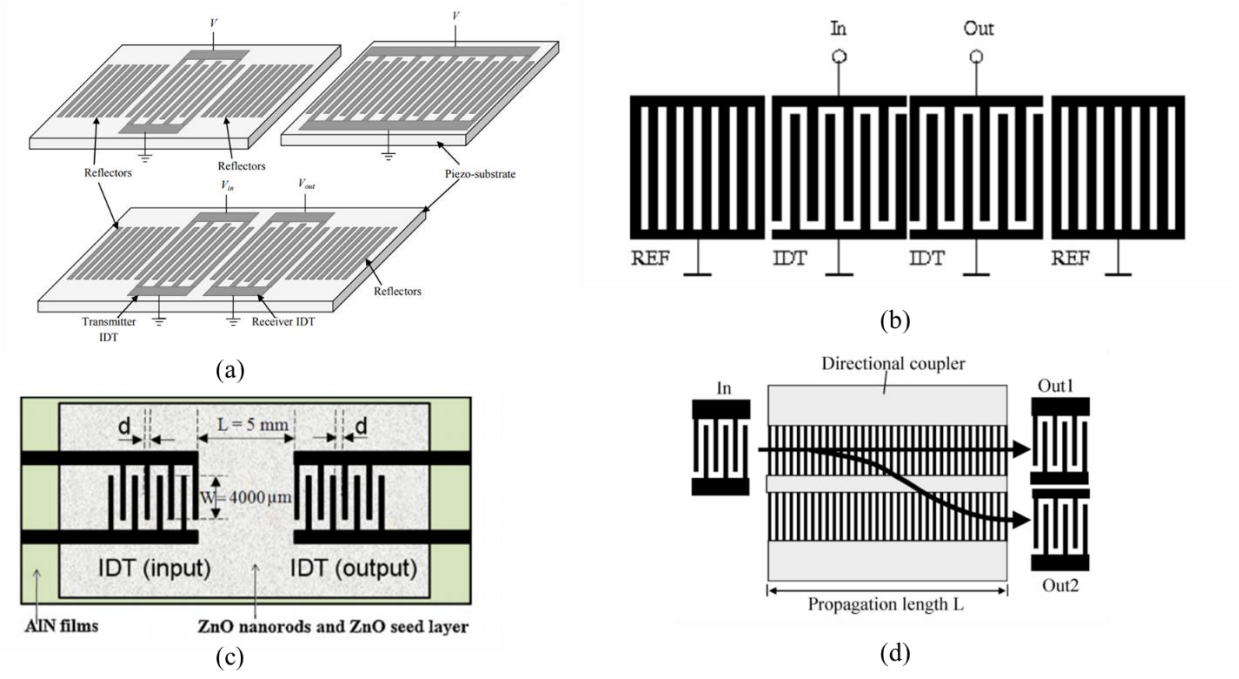

Figure 1.2 Examples of SAW implemented in piezoelectric materials for (a) resonators [27], (b) filters [28], (c) delay lines [32] and (d) waveguides [33].

Shown in Fig. 1.2 are few successful implementations of SAW in major piezoelectric materials (AlN, ZnO, PZT etc) as resonators (Fig.1.2 (a)), filters (Fig. 1.2(b)), delay lines (Fig. 1.2(c)) and waveguides (Fig. 1.2(c)). Despite its different functionalities, the surface elastic waves are all actuated and sensed by IDTs. However, with the recent development of wireless communication, it is desired to deploy the mechanical devices to obtain higher processing speed (5G or Wifi 6 for example), namely, to superimpose the mechanical waves at a higher frequency. However, the surface acoustic wave velocity is typically larger than the bulk acoustic wave velocity. Also, the pitch size of the IDT is inversely proportional to the resonant frequency ($d \propto \frac{1}{f}$). The dimension of the actuation or sensing IDTs needs to be very small to operate at ultra-high-frequency (UHF) range. On the contrary, while the mechanical wave propagates at the surface of the structure, part of the energy also leaks into the bulk with amplitude exponentially decaying. As

the attenuation decreases with the increasing wavelength, the devices need to be fabricated in large size to compensate for this wave propagation loss [34]. Therefore, these contradictory requirements determine the current limitation on the operating frequencies for SAW devices [29].

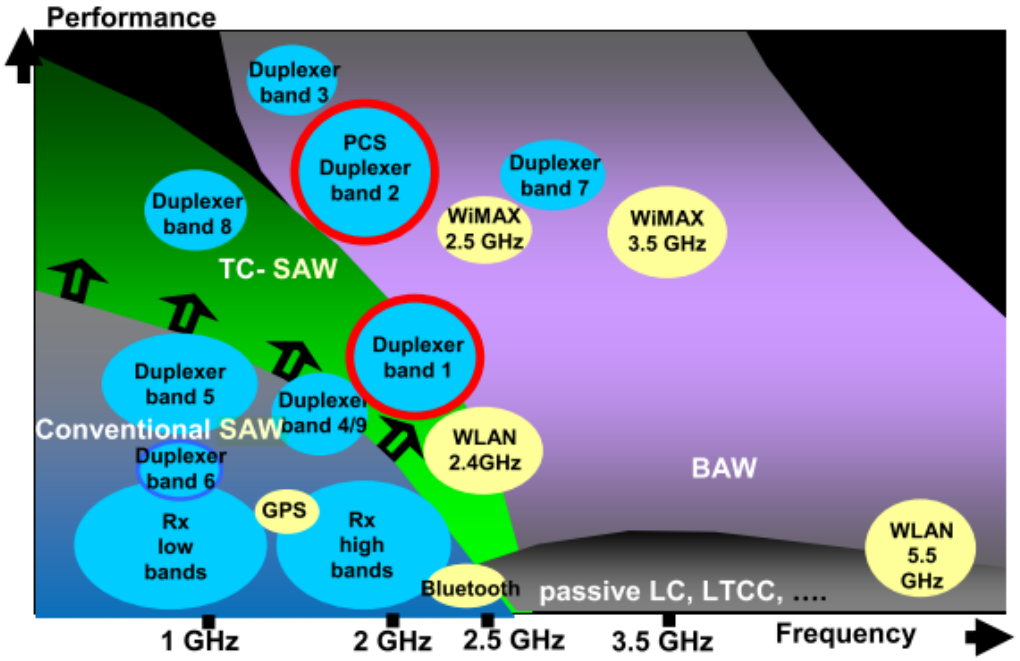

Figure 1.3 Commercial applications mapped to SAW and BAW [35].

1.2.2 BAW Devices

To overcome the drawbacks for SAW-based devices, instead of wave propagates only at the surface, manipulating the wave motion within the entire bulk of the solid is actively investigated these days [15], [35], [36]. As mentioned in the previous subsection, the bulk wave velocity is typically lower than the surface wave velocity, thus it provides the potential of GHz frequency operation. Few successful examples of BAW resonator design using piezoelectric materials have already been illuminated in the literature. Here we specifically demonstrate two system-level examples of BAW devices successfully implemented as RF filters and oscillators [3], [18].

As shown in Fig. 1.4(a), leveraging GlobalFoundries 200 mm RF silicon-on-insulator (RFSOI) technology and integrate piezoelectric AlScN at the BEOL, a switchable ladder-type filter composed by lamb mode resonators is demonstrated, operating at 2.4 GHz Bluetooth band as well

as 3.5 GHz B42 band [3]. The standalone BAW resonator achieved a corresponding Q and k_{eff}^2 of around 1500- 3000 and 6.7%, which translates to full coverage of Wifi and B42 bands. The corresponding overall insertion loss is less than 1.5 dB[3].

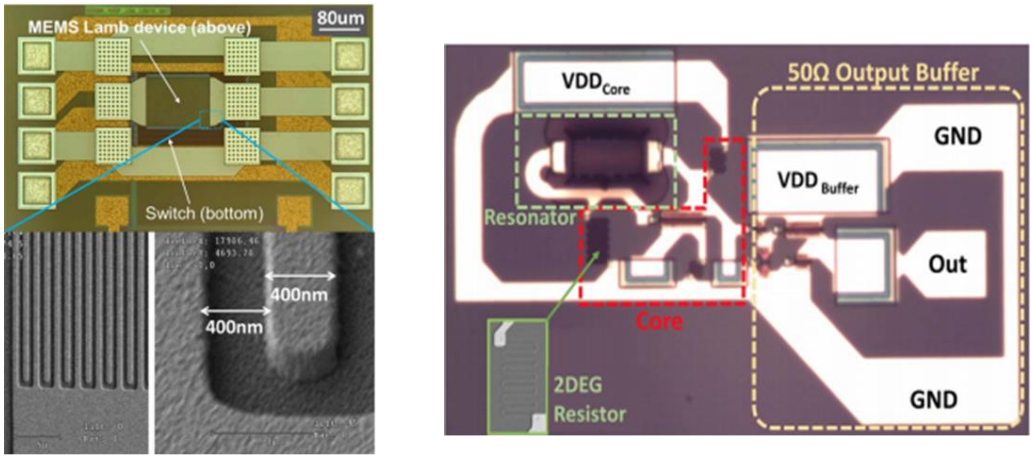

(a) (b)

Figure 1.4 Examples of BAW devices implemented as RF (a) filters [3] and (b) oscillators [18].

Besides, leveraging the in-house GaN technology, a Pierce and Colpitts type switchable GaN oscillator is shown in Fig. 1.4(b). The standalone Lamb mode resonator is operated at 1 GHz with corresponding Q and k_{eff}^2 of 4250 and 0.24% respectively [18]. The oscillator is operated at 1GHz with a maximum FOM of -205.9 dBc/Hz in an area of 0.057 mm^2. Both devices are switchable but under different mechanisms. The GlobalFoundries' filter utilized the front-end transistors as "real" RF switches while the GaN oscillators directly operate the 2D electron gas (DEG) at the AlGaN/GaN interface. Both devices can be seamlessly integrated with the standard CMOS process, which will greatly save the footprint and budget in large arrays, increase the yield, reduce the parasitic and power consumption.

The R&D efforts on BAW devices had been very active over the past decade and will remain active as new technologies including 5G, Wifi 6, internet of things (IoT), wearable radars [37], mm-wave imaging [38], and high-resolution actuators, sensors [39], [40], etc. come into being, focusing on the high-frequency operation while maintaining reasonable temperature stability, electromechanical coupling coefficient k_{eff}^2 and resonant Q [36]. The demanding performance of these systems alongside requirements for miniaturization, lower power consumption, and lower

cost have pushed the limits on what conventional technology can currently achieve [41]. With a high-*Q* and small footprint, integrate traditional MEMS resonators in the standard CMOS process, namely a CMOS-MEMS resonator, can provide ideal RF building blocks for large bandwidth, low insertion loss filters, low phase noise clocks, sensitive and accurate sensors, and beyond.

1.3 CMOS-MEMS Resonators

Even though MEMS has developed over six decades, challenges still remain as to how to properly integrate MEMS with standard IC. Mainly, there are two approaches to integrate MEMS with standard CMOS – either fabricate MEMS and CMOS on separate dies with independent fabrication processes or monolithically integrate MEMS within standard IC processes. The separated fabrication approach would unavoidably require additional wire-bonding processes to properly connect the CMOS die with MEMS die, thus introducing extra stress and impedance mismatch into the system, which would be the dominant barrier, especially for high-frequency RF applications.

On the other hand, the monolithic integration approach has become one of the mainstreams in CMOS technology to reduce power and cost. Mainly, the MEMS steps can start either before the CMOS process (MEMS-first) or after the CMOS process (MEMS-last). Apart from the newly established MEMS-CMOS filter design by Globalfoundaries (as shown in Fig. 1.4), TSMC has also released a process that successfully integrates metal-insulator-metal (MIM) capacitor after standard CMOS process[42]. Besides, S.S. Li's and G.K. Fedder's groups have also devoted a lot of efforts, demonstrating a couple of resonators[43]–[45]. Typically, no matter whether it is MEMS-first or MEMS-last process would require additional lithography masks and fabrication steps. This would then increase the overall complexity of the process, increase the risk of yield reduction, and would dramatically increase the cost.

Therefore, in recent years, more and more researches, including this dissertation, has focused on directly integrating the MEMS design with standard CMOS process with few if not breaking any of the design rules. The first pioneering work of the unreleased MEMS resonators integrated into commercialized standard CMOS technology was demonstrated by Radhika et al. in 2012. This work is directly integrated within IBM's 32nm SOI technology without any releasing, assembly, or postprocessing [4]. This demonstrated resonator incorporates a longitudinal-mode bar driven electrostatically and sensed using standard FET. The gate voltages are applied on two gates of

the independent-gate FinFET forcing the active region into inversion and accumulation. The RF signal is applied on top of the accumulation gate, forming an electrostatic force. The other channel is biased in inversion, forming a flowing drain current. At mechanical resonance, leveraging the piezoresistive effect, the drain current modulated by the elastic waves can be picked up.

Followed by this internal dielectric transduction, a new class of CMOS-MEMS resonators working at frequencies ranging from 3 GHz [46] to 32 GHz [47] have been put forward.

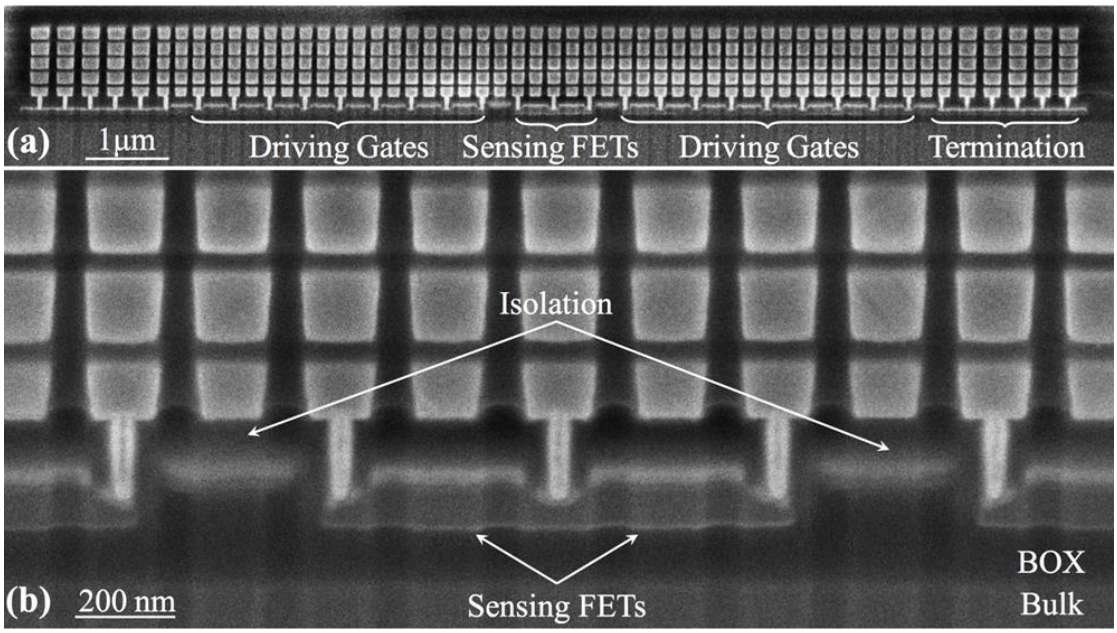

Figure 1.5 SEM of the unreleased resonant body transistor (RBT) in Globalfoundaries' 32nm SOI technology. The figure is adapted from [46].

Indicated by Fig. 1.5 is an unreleased RBT integrated within Globalfoundaris' 32nm SOI technology where the unreleased resonators were leveraging the MOS capacitors inherent to the process for electrostatic actuation to drive acoustic resonance in a solid-state acoustic 'cavity' defined using the CMOS layers.

A waveguided mode was found at 3.2GHz with an estimated *Q* of around 13,500, which marks 1000x higher *Q* than an LC resonator in a 10,000x smaller footprint. As this is fully integrated within the standard CMOS process, no post-processing of any kind is needed [48]. However, the electromechanical transconductance g_m in this case is on the order of 100nS. This high insertion loss (IL) would make oscillator or filter design very challenging. Thus, instead of traditional planar sensing transistors, the Globalfoundaries' 14LPP FinFET technology is leveraged to reduce the IL

and boost the g_m(the SEM is shown in Fig. 1.8). More recently, continuous sheets of copper in all BEOL layers were used to form an acoustic reflector. A waveguided mode at 33.7 GHz is found below the sound cone, which prohibits the elastic wave from propagating into the bulk, allowing only evanescent modes.

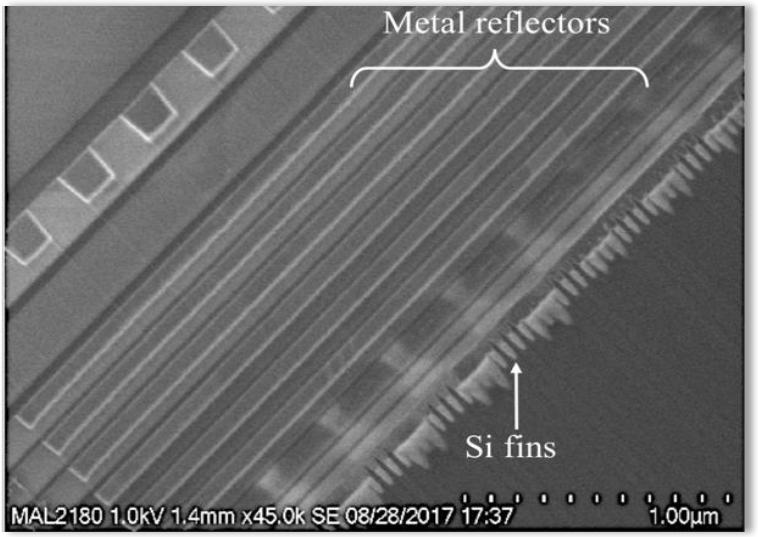

Figure 1.6 SEM of the resonant fin transistor (RFT) based on Globalfoundaries 14LPP technology [47].

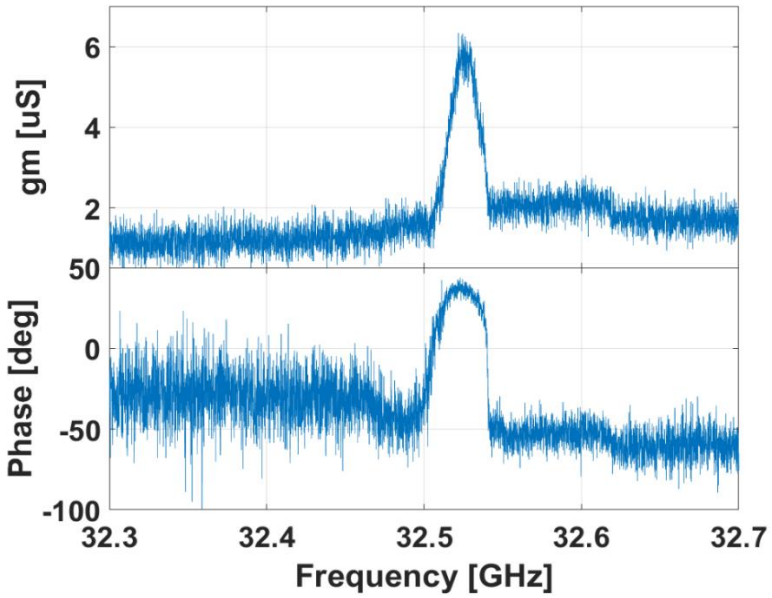

Figure 1.7 Measurement of the 32.5 GHz resonance with an estimated *Q* of about 1,200.

The characterized g_m is shown in Figure 1.9 where a 32.5 GHz resonance was found with an estimated Q of about 1,200. Compared with resonators on 32 nm SOI technology, g_m is increased to a few uS. While this has proved the effectiveness of FinFET to maximize output signal despite electrostatic drive [47], the IL is still at a high level especially for integrating these resonators in filters or oscillators operating at high frequencies. Therefore, to fundamentally increase the return loss and bandwidth of electrostatic transduction, thus increasing the driving force density, piezoelectric transduction is selected as a replacement.

1.4 Piezoelectric Transduction

The piezoelectric effect is first demonstrated by Jacques and Pierre Curie in 1880 [49]. Piezoelectricity refers to the effect where electric charges are accumulated at a certain area of a solid material under mechanical deformation and vice versa. The coupling between electrical and mechanical domain can be characterized by the following equation:

$$\boldsymbol{S} = \boldsymbol{s_E} \cdot \boldsymbol{T} + \boldsymbol{d^t} \cdot \boldsymbol{E}$$

$$\boldsymbol{D} = \boldsymbol{d} \cdot \boldsymbol{T} + \boldsymbol{\epsilon_T} \cdot \boldsymbol{E}$$

where, $\boldsymbol{S}, \boldsymbol{T}, \boldsymbol{E}, \boldsymbol{D}$ represent the strain, stress, electric field, and electric displacement respectively [5], [36]. The high energy density, low power configuration, ease of frequency scaling makes piezoelectric transduction mechanism a widely used solution for the past few decades in various situations, including actuators, sensors, resonators, etc. [36].

Due to the large transduction efficiency between electrical and mechanical domain, piezoelectric materials have been widely used in MEMS resonator design as well, widely used piezoelectric materials include aluminum nitride (AlN) [50]–[52], gallium nitride (GaN) [53], [54], zinc oxide (ZnO)[55], [56], lithium niobate ($LiNbO_3$)[57], etc.

While all these are good candidates for the RF front end (RFFE) applications, to utilize the RF bands more efficiently, the unused components are expected to turn off when unused. Hence, there would unavoidably be additional RF switches placed side-by-side with those piezoelectric components, which would lead to additional cost, footprint, and losses. Therefore, a tunable RF MEMS resonator is greatly desired and invaluable for RFFE application.

1.5 Ferroelectric Transduction

One of the promising candidates for realizing a tunable RFFE component is through the ferroelectric transduction mechanism.

As suggested by Fig. 1.7, all ferroelectric materials are essentially piezoelectric materials with an additional feature of polarization been built within the structure due to the lack of crystal central symmetry. This generated polarization can then be adjusted either heated or cooled [58]. In particular, ferroelectric material refers to a class of certain materials of which the spontaneous electric polarization can be reversed by applying an external electric field [59].

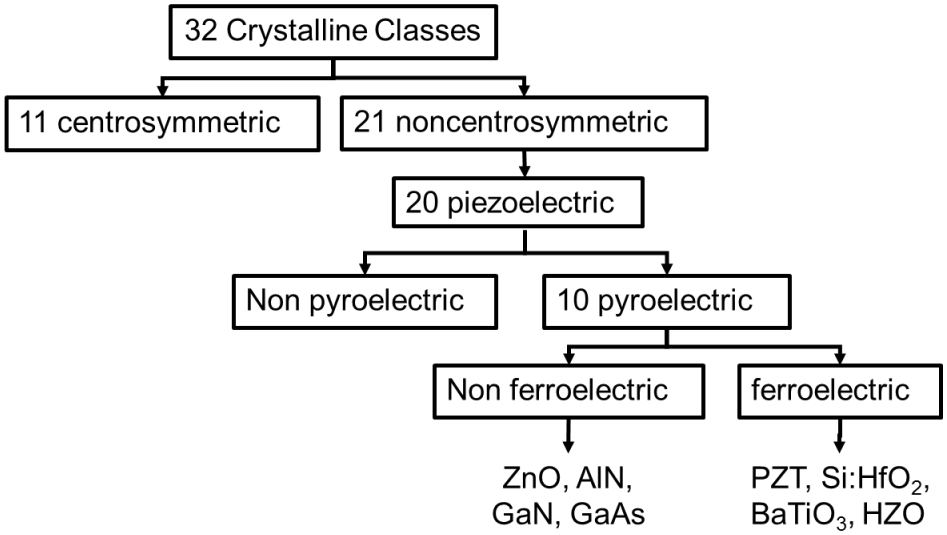

Figure 1.8 Crystalline material classification [60].

A typical hysteretic variation of polarization with respect to the changing electric field is plotted by Fig. 1.8.

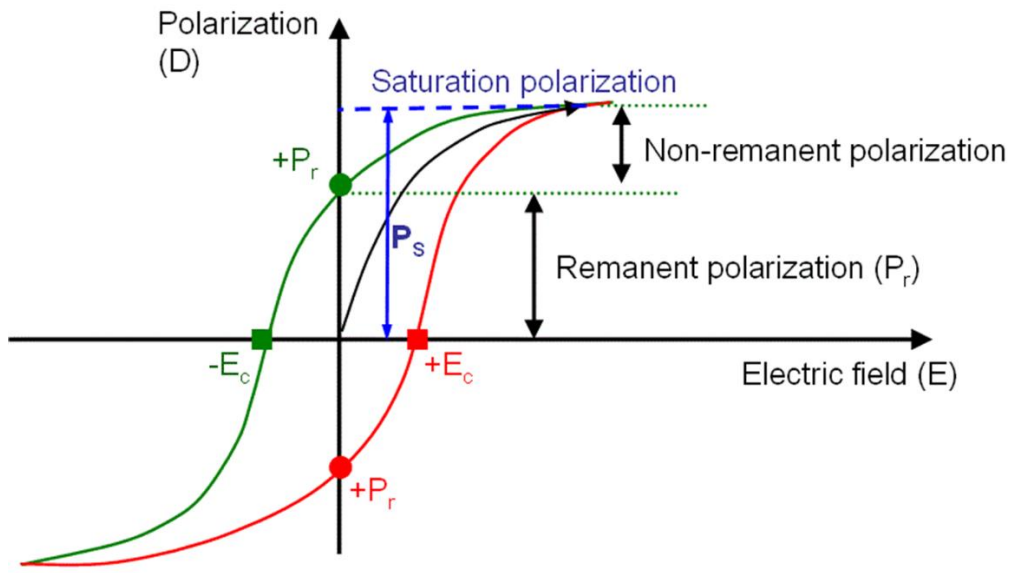

Figure 1.9 Typical hysteretic variation between the polarization and external electric field for ferroelectric materials [61].

When the electric field is applied on the ferroelectric material from zero to maximum, the polarization is first increased following the black curve from minimum towards the maximum/saturation polarization. Then, when the electric field is changing from the max positive to the max negative and vice versa, the polarization is varied in a non-linear manner and formed a hysteresis closed loop. Several important terms should be defined here and will be used in the later sections:

P_r: Remanent polarization. This is the term defined as the residue of the polarization when the electric field is removed from a poled ferroelectric material.

E_c: Coercive electric field or coercive field. This is the electric field where the ferroelectric material is no longer polarized.

P_s: Saturation polarization. This is the maximum polarization that the ferroelectric material can reach.

Therefore, if a ferroelectric material is formed as a metal-ferroelectric-metal (MFM) capacitor, upon operation, the ferroelectric material can be poled at the saturation polarization, inducing the electric field within the stack. Once a small signal v_{RF} is applied at the resonant frequency, a corresponding mechanical resonance can be obtained. Moreover, once the ferroelectric material is biased at E_c, the material is no longer poled and thus no internal electric

field is built. Hence, the MFM resonator could have the potential to demonstrate some switching capabilities.

In the rest of this section, we would like to introduce few widely used ferroelectric materials.

1.5.1 Scandium Doped Aluminum Nitride ($Al_{1-x}Sc_xN$)

Doping the wurtzite crystalized AlN has become a hot topic in the past years. Without breaking the crystal structure, the fundamental motivation of doping the AlN is to increase the electromechanical coupling coefficient (k^2) herein while maintaining the full compatibility with standard IC. The maximum k^2 reported so far is around 19% and it is achieved when the Sc/Al concentration is approximately 43% near the phase boundary between wurtzite and cubic crystal [62]. Yet, incorporating Sc within AlN usually leads to non-uniformly distribution of Sc, possibly as a consequence of preferential phase separation of the ScN rocksalt and AlN wurtzite crystals [24]. The heavier the doping of Sc within AlN, the larger the non-uniformity within the crystal. This would possibly lead to higher internal material losses and lower Q on the AlScN based devices.

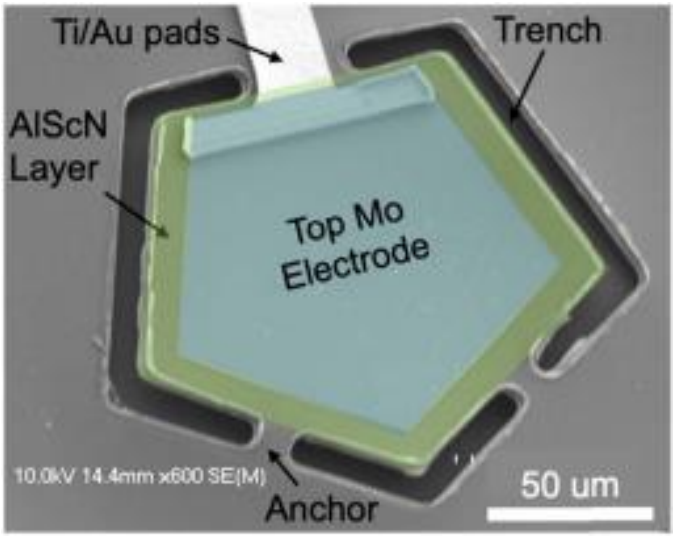

Figure 1.10 SEM for the AlScN resonator [63].

More recently, a ferroelectric behavior is found with $Al_{1-x}Sc_xN$ when x>27% [64]. The AlScN grown at VTT technical research center in Finland has been used to form a metal-ferroelectric-metal (MFM) resonator. The demonstrated k_t^2 is about 18.1% with a Q_m of 328.5 [63].

1.5.2 Hafnium Zirconium Oxide (HZO)

The discovery of ferroelectricity in HfO_2-based thin films can be traced back to 2011[65]. Due to similar chemical and physical properties between Hf and Zr, doping the HfO2 with Zr (~50%) can illustrate very stable and robust maximum ferroelectric polarization with a very thin film (< 50 nm). In the meantime, HZO can be annealed at around 400℃ to 600℃, making it fully compatible within BEOL of standard CMOS flow [66], [67].

Due to its strong ferroelectric properties, thin-film HZO has been widely used in ferroelectric memory devices like FeFET or FeRAM [67]. Leveraging the large piezoelectric coefficient, fully conformal deposition, and full integration within standard CMOS, ALD deposited thin-film HZO has also been applied to piezoelectric transducers[68], [69].

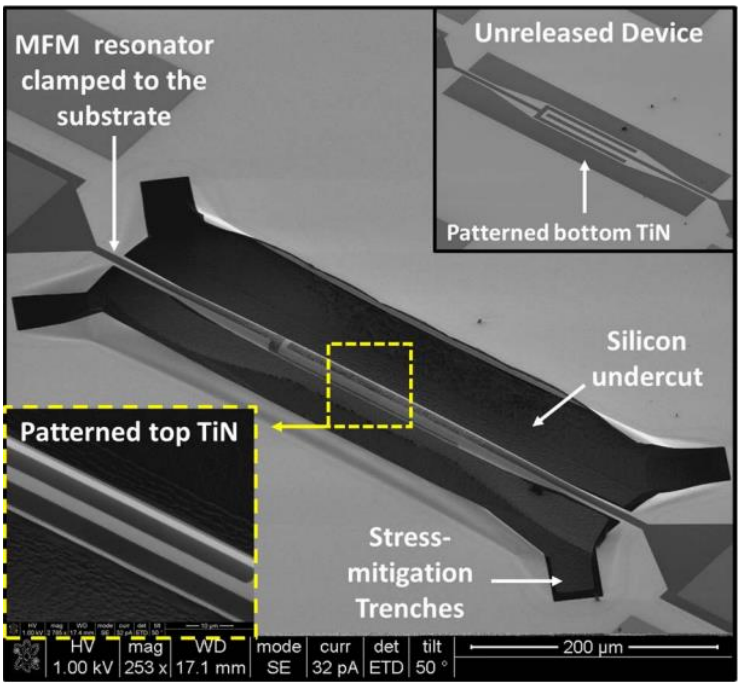

Figure 1.11 SEM of a doubly-clamped HZO based resonator [69].

Figure 1.10 demonstrated a most recent clamp-clamp beam HZO based resonator where the central material stack is formed by 10nm TiN/10nm HZO/10nm TiN[68]–[70]. A *Q* of 1930 was observed at 195 kHz flexural mode resonance [69].

1.5.3 Lead Zirconate Titanate (PZT)

Compared with more recently discovered AlScN or HZO, PZT is a more conventional material that has been widely used in various fields. The first lead zirconate titanate ceramic was discovered by researchers at the Tokyo Institute of Technology around 1952 [71]. Due to its high piezoelectric coupling efficiency as well as wide operating temperature range, PZT has become a popular piezoelectric material since then. The maximum electromechanical coupling coefficient for bulk PZT can reach up to 70%. Inspired by the discovery of bulk PZT, in the microelectromechanical community, thin-film PZT can be grown by sol-gel, RF sputtering, MOCVD, or jet vapor deposition processes and is widely utilized as actuators, sensors, energy harvesters, and piezoelectric micromachined ultrasound transducers (pMUT) [72].

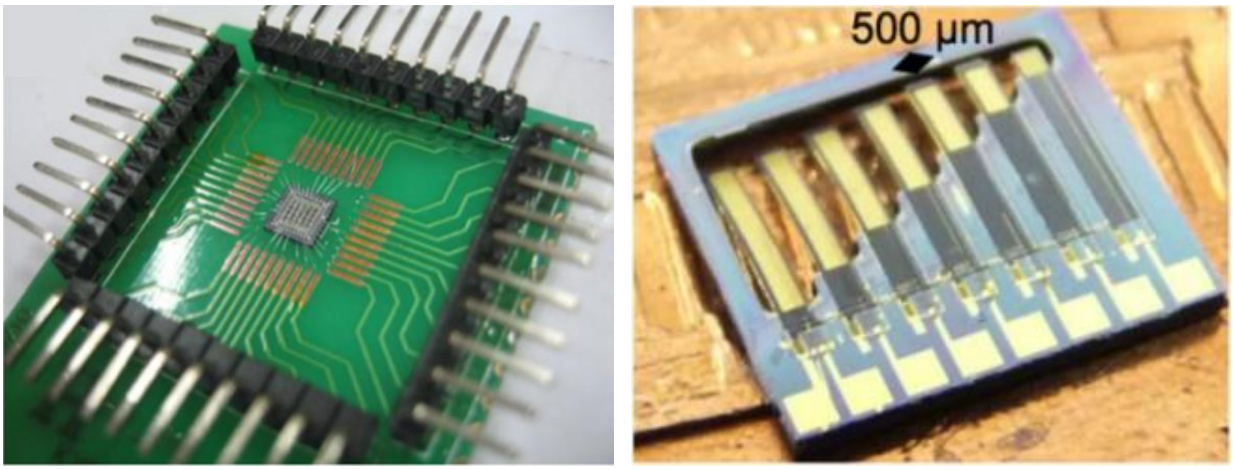

Figure 1.12 Schematic of PZT based pMUT and cantilever actuators [72], [73].

Few PZT based piezoelectric transducers are shown in Fig. 1.11, the actuator or transducer is typically formed by sandwiching the PZT by the top and bottom metal electrode. Upon operation, the electrical signal at the pre-designed resonant frequency is applied to the actuator. Due to the large piezoelectric coefficient, strong actuation pulses or displacement can be generated.

At the same time, PZT also has ferroelectric properties that enable tunable structures or devices. Leveraging the ferroelectric characteristics, PZT based FBARs have been demonstrated as switchable and tunable resonators [11], [74]. Specifically, Zinck et al. demonstrated a PZT based FBAR operating at 1.4 GHz with Q of 85 and k_t^2 of 7.3% [74]. Larson et al. compare PZT properties at ultrahigh frequencies from different deposition methods [75]. It is observed that the

elastic attenuation is directly related to the density and surface smoothness of the thin film. From the resonator's point of view, these drawbacks will greatly affect the *Q*. Therefore, a standardized fabrication process is needed to reduce these elastic attenuations and obtain proper *Q*. Unfortunately, lead is regarded as one of the major contamination resources for standardized CMOS process, one of the drawbacks for the PZT related devices was that it could not be integrated with standard IC until the commercially available FRAM came along.

Thanks to the development of ferroelectric random-access memory (FRAM), recently, PZT based nonvolatile FRAM is commercially available from several vendors including Ramtron, Texas Instruments, and Fujitsu. Instead of the front-end process, the PZT thin film can be built by adding additional photomasks at the Back-End-Of-Line (BEOL) process [76]. Hence, FRAM demonstrates successful integration of high-performance PZT ferroelectric thin films within standard complementary metal-oxide-semiconductor (CMOS) technology [76]. Thanks to the Texas instrument's ferroelectric RAM (FeRAM) technology which has successfully integrated ferroelectric PZT in the back-end-of-line (BEOL) process of the 130nm CMOS technology. Leveraging this special IC platform, it is possible to build a CMOS-MEMS resonator with a higher electromechanical coupling coefficient, smaller footprint, and lower cost.

In this thesis, the design, characterization, and discussion of the first tunable ferroelectric capacitor (FeCAP) based unreleased RF MEMS resonator will be demonstrated. The designs are monolithically integrated seamlessly in Texas Instruments' 130nm Ferroelectric RAM (FeRAM) solid-state CMOS technology, with no post-processing or release step typical of other MEMS devices [77].

A wave-guided mechanical resonance is targeted, implemented, tested, and discussed. A comprehensive model for the resonator is developed and analyzed. In the meantime, thanks to the ferroelectric characteristics of the PZT, except for the on/off state, the designed mechanical resonance can switch between resonant pole/off/zero states [78].

1.6 Thesis Outline

This thesis starts with a general introduction of signal processing superimposed upon mechanical devices. Leveraging its slow wave velocity and low loss in high-quality materials, either mechanical SAW or BAW devices have been deployed in cellular or base station radio communication systems. Even though SAW or BAW devices have been massively manufactured

and commercialized in the past few years, new structures or devices aiming at low cost, footprint, loss, complexity, and power consumption but targeting for the high frequency and high yield are still actively explored. One of the promising approaches would be integrating traditional piezoelectric MEMS resonators within standard CMOS processes. Hence, this thesis demonstrates the first of its kind of piezoelectric PZT MEMS devices successfully integrated within Texas Instruments' ferroelectric RAM standard process. Implementing piezoelectric PZT within standard process not only greatly reduced footprint, parasitic as a standalone single device but also reduced the budget as well as power consumption dramatically in a large array.

The thesis includes 6 chapters including this introductory chapter. Chapter 2 described the FeCAP based resonator's design process in detail. The FeCAP array is split into multiple periodic sections with each section designed as a waveguide in which the mechanical motion is mostly confined at the piezoelectric thin layer. Multiple approaches of boosting Q are applied including uniform vias and uniform terminations at the sides.

Chapter 3 demonstrates an interesting phenomenon obtained from those FeCAP based resonators. If the FeCAP is biased in a standard two-port manner, the mechanical resonance in transmission S_{21} can be tuned between zero, pole, and zero states. An equivalent circuit has been developed to model the mechanical resonator and to understand the switching mechanism. This chapter explores the potential of the FeCAP resonator being implemented as a promising switchable RF front-end component.

While the first 3 chapters demonstrate a new piezoelectric resonator as a BAW device that can be used to manipulate mechanical waves traditionally. Starting from Chapter 4, an acoustic metamaterial-based mechanical signal processing approach is introduced and explored. As an artificial periodic material, acoustic metamaterial has demonstrated few unexpected physical phenomena, namely, the mechanical bandgap and negative refraction.

Chapter 5 presents the mechanical resonance induced by asymmetric AlN-based acoustic metamaterial. The obtained mechanical resonance is very localized so that the corresponding band within the dispersion relationship is flat with group velocity close to zero.

Chapter 6 illustrates a new guided negative refraction effect induced by the asymmetric acoustic metamaterials. The elastic wave is guided along the diagonal of the unit lattice and split into three branches at the acoustic metamaterial and bulk AlN interface. Leveraging this unique

structure design, this chapter explores the ability to guide, trap, and split elastic waves with low dispersion.

2. FERROELECTRIC CAPACITOR BASED UNRELEASED RESONATORS

A version of the chapter has been reprinted with permission from Nature Microsystems & Nanotechnology.

Y. He, B. Bahr, M. Si, P. Ye, and D. Weinstein, "A tunable ferroelectric based unreleased RF resonator," *Microsystems Nanoeng*., vol. 6, no. 1, pp. 1–7, Dec. 2020

As illustrated by section 1.4, the nonlinear hysteretic behavior of the ferroelectric electric polarization has driven fundamental investigation and commercial development for IC memory and has sparked a class of devices termed ferroelectric RAM (FeRAM or FRAM). Texas Instruments (TI) E035 FeRAM technology has integrated ferroelectric PZT in the back-end-of-line (BEOL) process of their 130nm CMOS technology. Leveraging this IC platform, we can realize ferroelectric-based CMOS-MEMS resonators with higher electromechanical coupling coefficient (k^2) than their electrostatic counterparts. The boost in performance facilitates larger bandwidth filters, lower power oscillators, and higher frequency tolerance to fabrication variations.

In this chapter, the piezoelectric resonators designed in Texas Instruments' Ferroelectric RAM (FeRAM) process will be demonstrated [79]. The technology contains ferroelectric PZT capacitors integrated within the metal layers of the CMOS stack, utilizing the hysteresis characteristics for memory devices (shown in Figure 2.1 [80]).

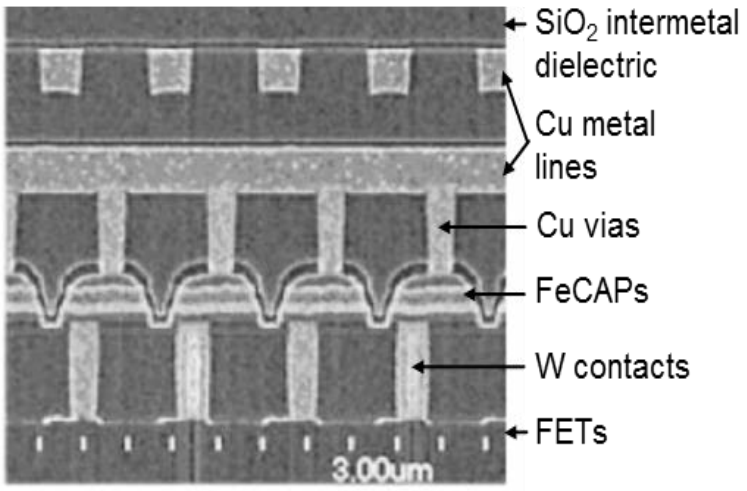

Figure 2.1 Schematic of the cross-section of Texas Instruments FeRAM device [79].

2.1 Simulation and Design

2.1.1 Dispersion relations

In order to define the resonance mode with the highest Q and transduction efficiency, acoustic waves must be well confined vertically in the CMOS stack with stress maximized in the PZT layer within the ferroelectric capacitors. Analogous to optical waveguide design, this is achieved using acoustic waveguiding within the CMOS stack. Assuming an infinitely long translationally invariant structure, we first determine the dispersion relations of the CMOS stack to define modes restricted to propagation in the plane of the wafer.

The device is first divided into multiple periodic unit cells with lattice constant a (with the schematic shown in Fig. 2.2(a)). To impose lateral (x-direction) translational symmetry, the left, and right boundaries are defined as Floquet periodic boundary conditions

$$\vec{u}_R(\vec{r}) = \vec{u}_L(\vec{r}) \cdot e^{-i\vec{k}\cdot\vec{r}} \tag{2-1}$$

where $\vec{u}_L$ and $\vec{u}_R$ are the displacement field at the left and the right boundaries of the single unit cell. $\vec{k}$ is the wave-vector which, due to the periodicity of the lattice, can be determined from the reciprocal lattice with a periodicity of π/a. This corresponds to the lateral width of the first irreducible Brillouin zone in the reciprocal lattice (shown in Fig. 2.2(a)). The corresponding schematic of the unit cell is shown in Fig. 2.2(b).

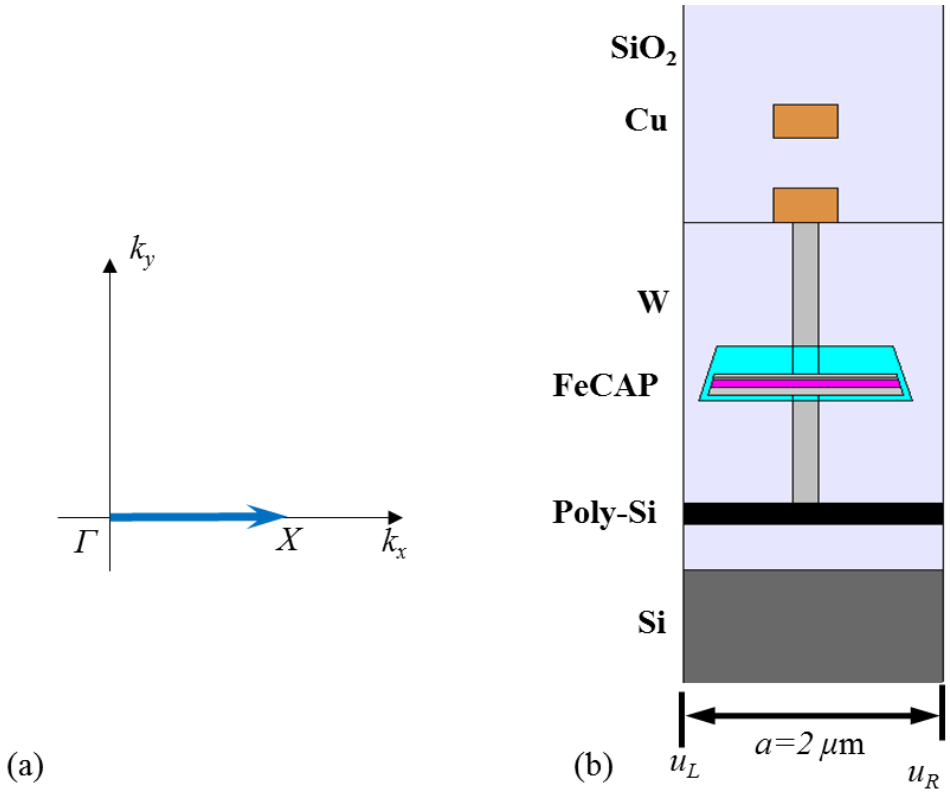

Figure 2.2 (a) Schematic of the first irreducible Brillouin zone in 1D case. (b) Schematic of the corresponding unit cell.

Two-dimensional finite element analysis is then performed in COMSOL Multiphysics® to map these waveguided modes. By applying Perfectly Matched Layers (PML) at the top and bottom of the device, no reflections from these boundaries are considered, approximating an infinitely thick Si substrate as well as a thick, acoustically lossy dielectric layer in the BEOL. By searching the eigenmodes along the first irreducible Brillouin zone, the dispersion relations can be mapped.

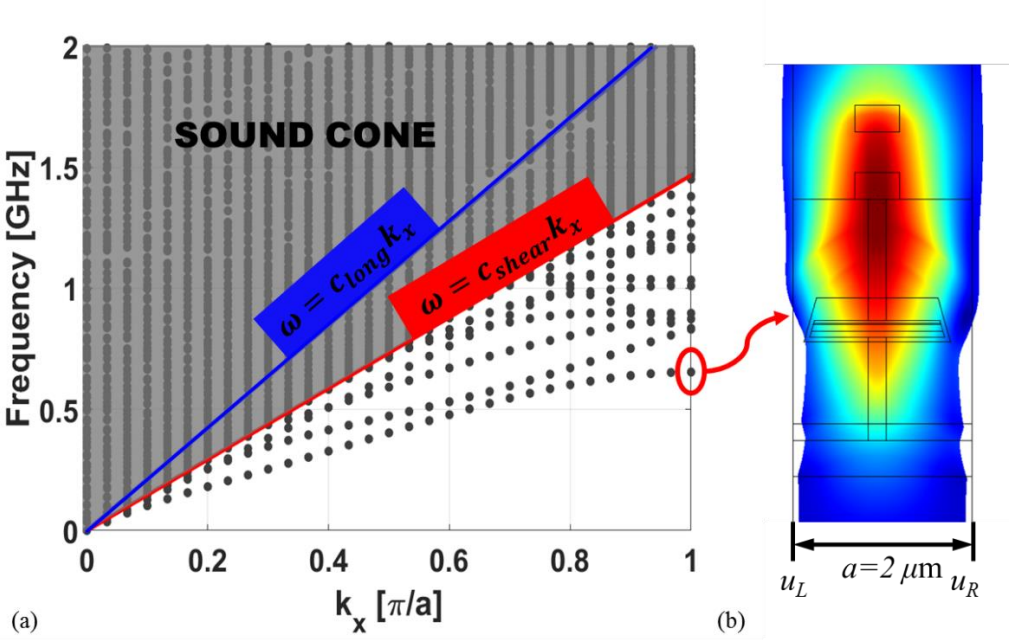

Figure 2.3 (a) Dispersion relation showing the vertically confined mode. Modes in the sound cone are free to propagate into the bulk Si substrate and cannot be well confined. (b) The corresponding displacement field of the localized mode shape of the unit cell FeCAP.

The resulting dispersion relation for the acoustic modes in the CMOS stack is shown in Fig. 2.3(a). Each point in the dispersion relation corresponds to an eigenmode of the periodic FeCAP structure. This dispersion relation can be divided into three regions separated by sound-lines (red and blue) represented by $\omega = c \cdot k$ where c is the corresponding longitudinal (blue) or shear (red) acoustic velocity in the Si substrate. Above the longitudinal sound-line is a region where all modes are free to propagate, referred to as the "sound cone". Additionally, below the shear sound line exist several discrete modes with sufficiently low acoustic velocity, indicating that the elastic waves are prohibited from propagating in the bulk and the elastic energy is therefore confined in the BEOL region of the CMOS chip. The resulting solid-state acoustic waveguide assumes translational symmetry with a period of a. Any perturbation along the wave propagation direction will generate scattering, which will then result in the coupling of different waveguided modes and decrease the Q [46]. It was previously shown that driving along $k_x = \pi/a$ is beneficial for reducing scattering to the sound cone, enabling higher Q [46]. In the meantime, the farther away the activated mode from the sound line, the better confinement the resonator will achieve. It is found that a device with trapezoidal FeCAP spanning 1.4 μm and two 0.6μm wide metal layers above it exhibits the best vertical acoustic confinement. Hence, Fig. 2.3(b) shows a vertically

confined mode at 700 MHz where the strain is well contained in the FeCAP, W via, and Cu metal[78].

2.1.2 FeCAP Design

Several designs are put forward and optimized. The details of the optimization process are summarized in Supplementary Information.

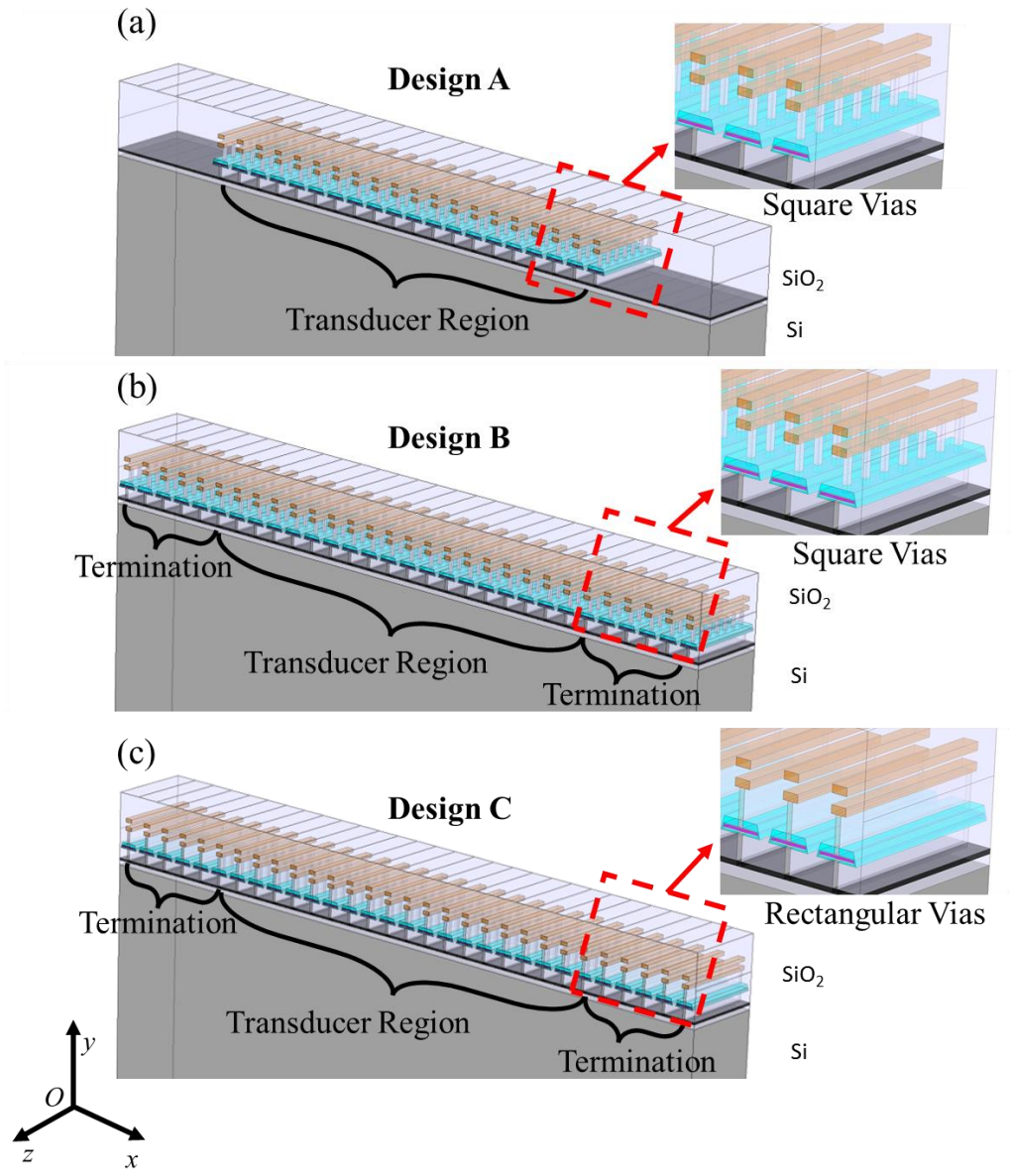

Figure 2.4 (a) Schematics of the resonator with only the main resonant cavity (b) containing both main cavity and two terminations at the sides, and (c) with the main cavity, terminations, and traditional square vias replaced by rectangular vias.

To optimize lateral confinement of the acoustic mode, termination of the acoustic waveguide in the plane of the wafer must be carefully considered. In Design A (Fig. 2.4(a)), the resonator is abruptly terminated at either end of the transducer region, leading to larger impedance mismatch, and subsequent scattering loss. In Design B (Fig. 2.4(b)), dummy FeCAP unit cells are added to either end of the transducers. These elements are spaced with the same period as the FeCAP

transducer region. In this way, the boundaries of the transducers are extended towards the ends and the scattering losses inside the transducer region can be minimized.

The waveguided modes are optimized based on 2D analysis, assuming infinite uniform geometry in the transverse direction $\overrightarrow{oz}$. To make the fabricated device match most closely with this approximation, one would maintain the structure in $\overrightarrow{oz}$ direction as continuous as possible ensuring high Q and minimization of spurious modes. However, as is traditionally found in IC technology, discrete-block vias are used to electrically route the FeCAPs to the first metal layer. Instead, in certain permutations of the FeCAP resonator, discrete ("square") vias are replaced with continuous, rectangular, "wall-like" vias. to avoid scattering losses along $\overrightarrow{oz}$ direction, as shown in Fig. 2.4(c).

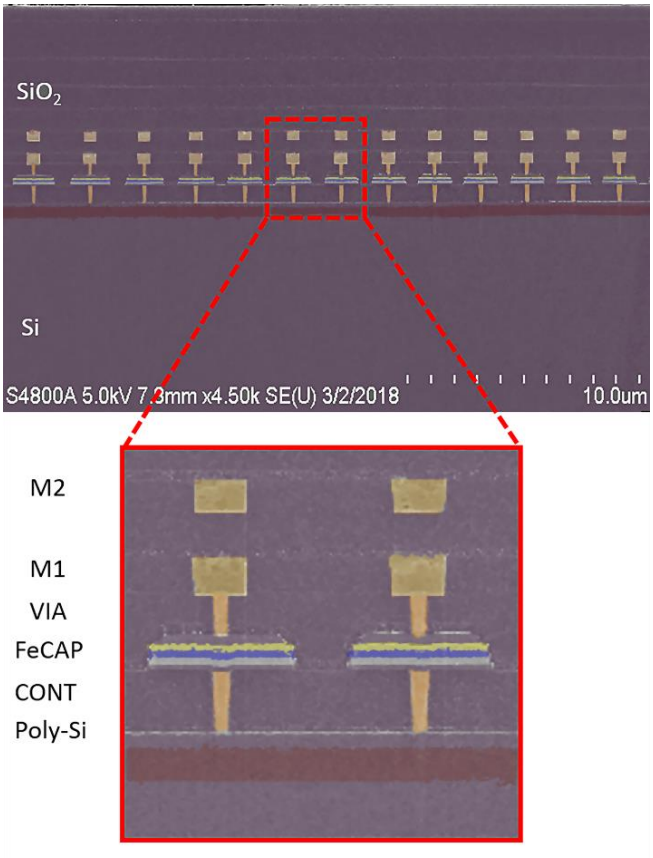

Figure 2.5 Cross-sectional scanning electron micrograph (SEM) of the CMOS-MEMS FeCAP based resonator [78].

The corresponding scanning electron micrograph (SEM) of a side view schematic of the proposed resonator is plotted in Figure 2.5, showing an array of trapezoidal FeCAPs each spanning 1.4 µm in length, connected to Cu strips by W vias. The resonator consists of 20 transducers alternating with 2 µm periodicity to form the resonant cavity. The resonator has an overall footprint of 108 µm by 7 µm.

2.2 Experimental Results and Discussion

2.2.1 Ferroelectric Polarization-Electric Field (P-E) Characterization

The ferroelectric properties of the FeCAP were first characterized to investigate PZT film behavior. Polarization-Electric field (P-E) measurement was carried out on a Radiant Technologies RT66C ferroelectric tester, shown in Fig. 2.6. The operational voltages for the FeCAPs are limited between -1.5 V and 1.5 V by dielectric leakage. A coercive voltage of ±0.3 V is obtained with remnant polarization of 16.86 μC/cm^2. Whenever the applied voltage is beyond the coercive field, the internal electric field direction would be flipped. The saturation polarization, in this case, is 38 μC/cm^2.

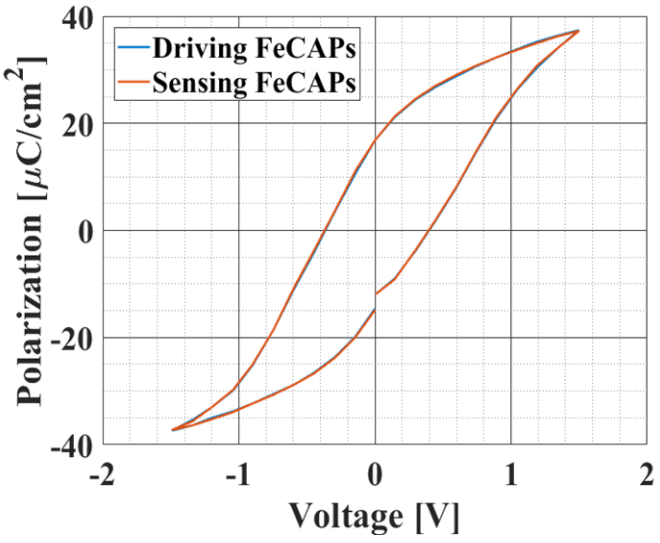

Figure 2.6 Measured hysteresis of ferroelectric PZT FeCAP polarization. For efficient piezoelectric transduction, a polarization voltage V_P between -1.5V and 1.5V is applied across the device.

It should be noted that, as demonstrated by the PE hysteretic loop in Fig. 2.6, there is a discontinuity at $V = 0$. This is believed to be a consequence of the dielectric leakage from the ferroelectric PZT capacitors.

In the P-E measurement, a triangular voltage wave is applied to the ferroelectric capacitor, and then the current is measured simultaneously. The polarization charge can be calculated by the integration of current over time,

$$P = \int I \, dt \tag{2-2}$$

Ideally, the current is due to ferroelectric polarization switching (I_{FE}). However, the non-ideal effect exists like leakage current (I_{LEAK}) or charge trapping current (I_C). So, the total current becomes

$$I = I_{FE} + I_{LEAK} + I_C \tag{2-3}$$

The real measurement includes all currents:

$$P = \int I_{FE} + I_{LEAK} + I_C \, dt = P_{FE} + P_{LEAK} + P_C \tag{2-4}$$

P_{FE} signifies the intrinsic ferroelectric properties while P_{LEAK} and P_C are non-ideal effects. The non-ideal effects can lead to the deviation from the standard loop and the discontinuity observed.

2.2.2 Radio Frequency (RF) Measurement and Discussion

As previously noted, the entire device consists of an array of 20 FeCAPs transducers (shown in Fig. 2.5). This gives a total FeCAP area of 196 μm^2 on the transducers. The experimental setup is shown in Figure 2.7.

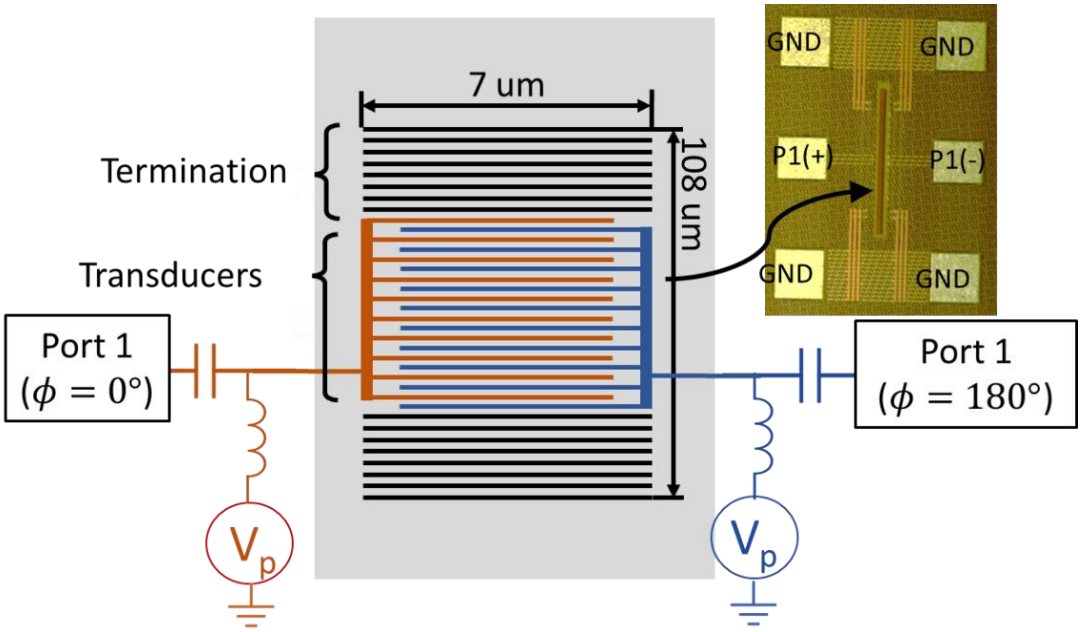

Figure 2.7 Experimental setup to characterize the FeCAP resonator, including a schematic of the port connected to the transducers. Electrically isolated FeCAPs on either side of these transducers (black) are used to terminate the resonance cavity and provide in-plane elastic confinement. Inset shows an optical micrograph of the device.

To enforce the excitation of the desired mode at the Brillouin zone edge ($k = \pi/a$), a differential signal was applied between alternating transducers. Differential 1-port RF measurement was performed in ambient pressure and temperature using a Keysight N5225A PNA. The poling voltage was provided by two Keithley 2400 source measurement units (SMUs), connected to ports $1(+)$ and $1(-)$ through bias tees. All transducers are biased at the same poling voltage (V_p). The RF power is -10 dBm which corresponds to a peak-to-peak voltage of 200 mV. The IF bandwidth (IFBW) is 500 Hz. The differential S-parameters can be obtained by the following equation

$$S_{dd11} = (S_{11} + S_{22} - S_{12} - S_{21})/2 \tag{2-5}$$

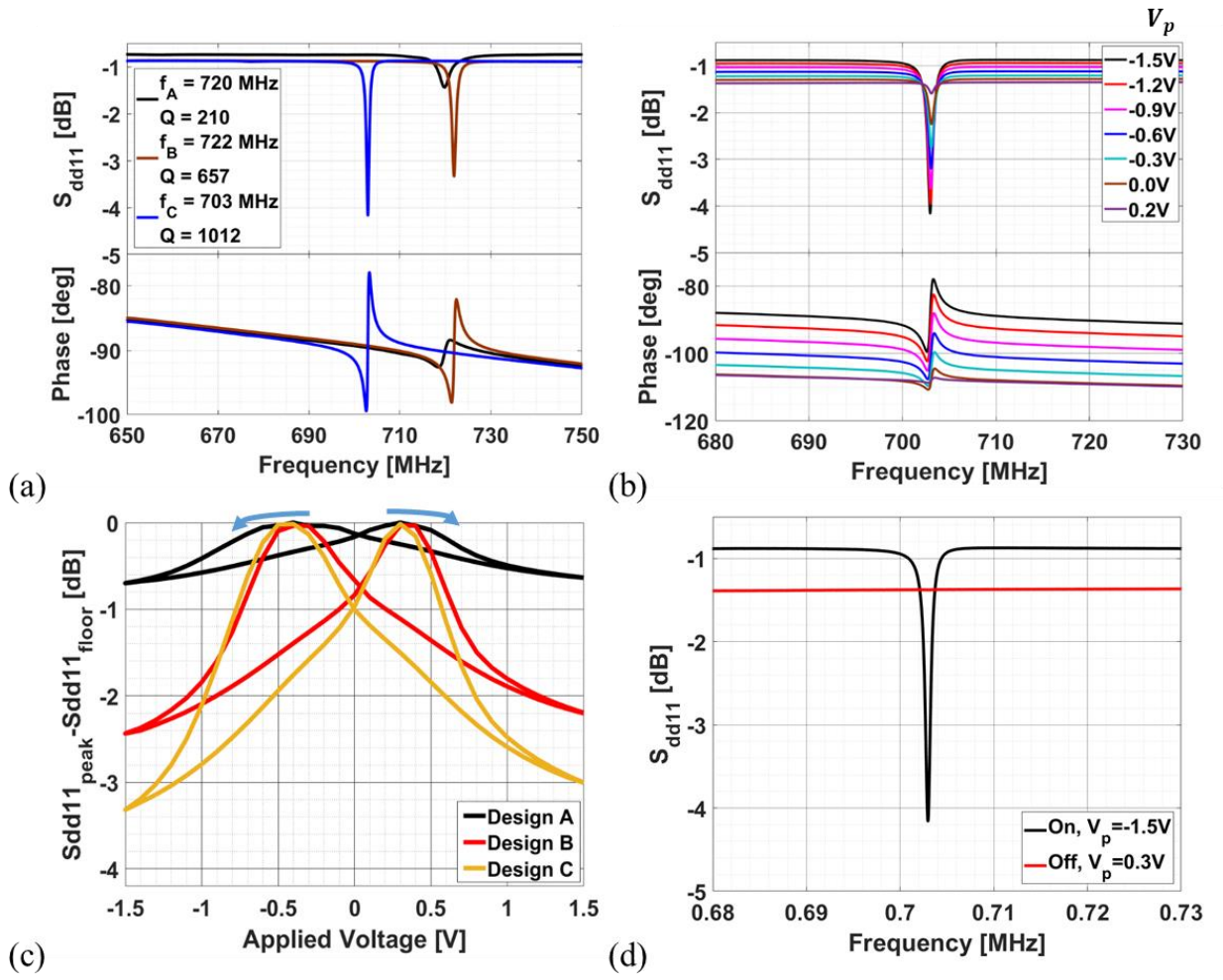

Figure 2.8 RF characterization of the FeCAP resonators. (a) Comparison of S_{21} for all the designs A-C (b) Measured frequency response of design C. (c) Due to the ferroelectric hysteresis, the S_{21} magnitude demonstrates 'butterfly'-shaped variations with changing poling voltage. (d) At coercive voltages of ±0.3V, the FeCAP transducer can be completely switched off.

Figure 2.8 summarizes the measured RF response of the FeCAP resonators. We first consider resonator Design A, a waveguided resonance is observed at 720 MHz with Q of 210 (black line in Fig. 2.8(a)). For Design B, the same resonance mode is found at 722 MHz but Q increased to 657 (brown line in Fig. 2.8(a)). Then, due to mass-loading from the added W volume, the resonance frequency for Design C shifts down to 703 MHz, and Q increases to 1012. With an f·Q product of 7.11×10^{11} (blue line in Fig. 2.8(a)), the performance is 1.6x higher than the most state-of-the-art PZT resonators. In addition, the resonator is monolithically integrable with the CMOS platform[41].

The dependence of S_{dd11} on poling voltage is shown in Fig. 2.8(b) varying V_p from -1.5V to 0.2V on both port $1(+)$ and port $1(-)$. The resulting 'butterfly'-shaped S_{dd11} magnitude variation at resonance with poling voltage is shown in Fig. 2.8(c). The magnitude of S_{dd11} reaches a minimum when all the transducers are biased at ±1.5V. Additionally, piezoelectric transduction is suppressed when the device is biased at the FeCAP coercive voltage of ±0.3V (Fig. 2.8(d)).

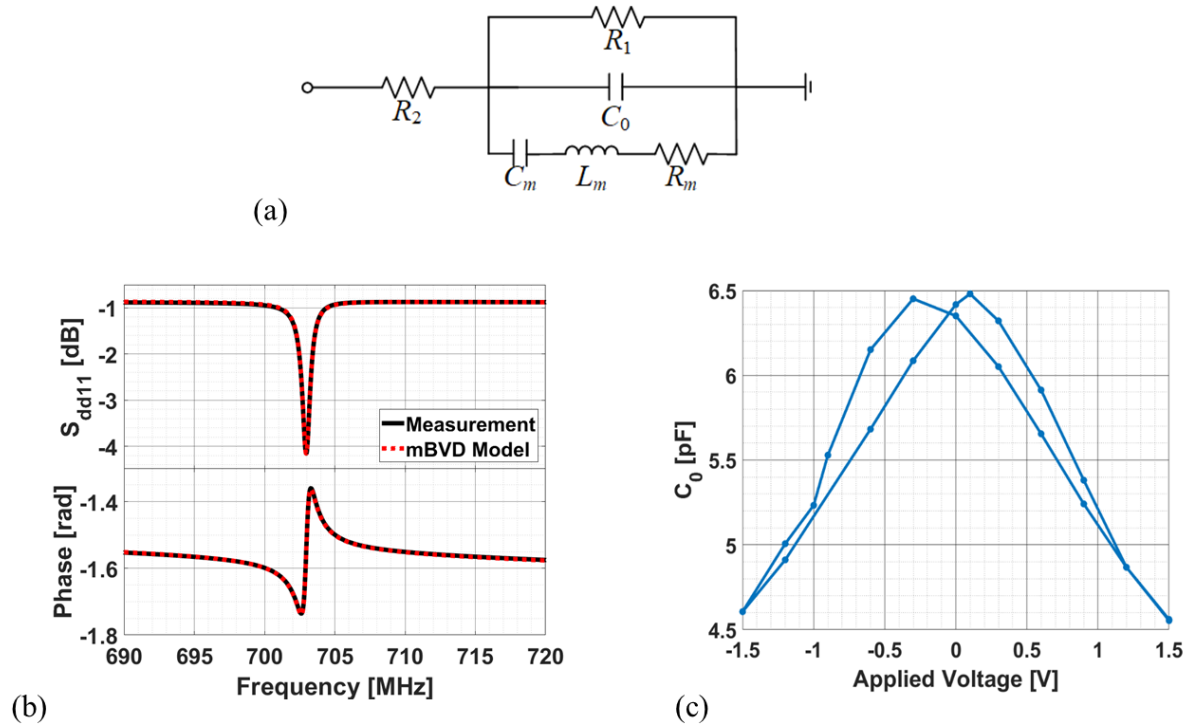

Figure 2.9 (a) Equivalent circuit of FeCAP resonator based on modified Butterworth-Van-Dyke model (b) S_{dd11} of mBVD model and the measurement for the resonator with extensions and rectangular vias. (c) Measured C_0 variation with respect to the changing poling voltage.

A small-signal equivalent circuit of the FeCAP resonator based on a modified Butterworth-Van-Dyke (mBVD) [81]is presented in Fig. 2.9(a), consisting of a mechanical resonance branch that includes a motional resistance (R_m), motional inductance (L_m), and motional capacitance (C_m), in parallel with C_0. Here, C_0 is defined as the geometric capacitance of the structure which is valid for a fixed poling voltage. In the meantime, R_1 and R_2 model any resistive losses from leakage in the FeCAP and routing, respectively. The equivalent circuit parameters fitted to the measured data

for design C under a poling voltage of -1.5V are shown in Figure 2.9(b). The corresponding circuit parameters are summarized in Table 2-1.

Table 2-1 Performance of resonator Design C

Parameters	Value	Unit
R_m	134.5	Ω
L_m	30.8	μH
C_m	1.7	fF
C_0	4.5	pF
R_1	1959.8	Ω
R_2	3.8	Ω
Q	1012	-
k^2	0.047	-

The electromechanical coupling coefficient can be extracted as:

$$k^2 = \frac{\pi^2}{8}\frac{C_m}{C_0} = 0.047\% \tag{3-6}$$

Under the full bias sweep, C_0 varies between 4.6 pF and 6.5 pF as demonstrated in Fig. 2.9(c).

2.2.3 Thermal Stability Measurement

Thermal stability of resonance frequency was characterized for the FeCAP resonators over a temperature range from 23 to 90°C.

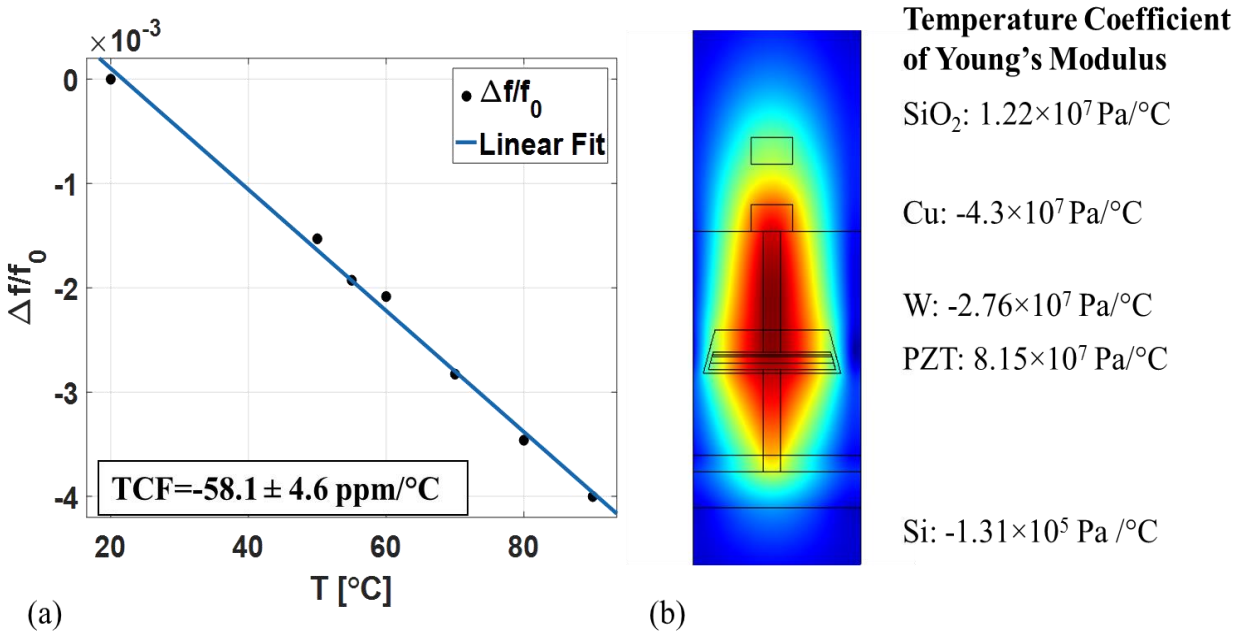

Figure 2.10 (a) Resonant frequency shift under different temperatures (b) Corresponding temperature coefficient of Young's modulus for the main component within the device.

The resonant frequency shift with respect to the temperature variation is shown in Fig. 2.10(a) and the Temperature Coefficient of Frequency was extracted as:

$$TCF = \frac{1}{f_0}\frac{\partial f}{\partial T} = \text{-58.1±4.6 ppm/°C} \quad (4)$$

This measured temperature sensitivity matches well to the predicted values based on the Temperature Coefficient of Young's Modulus ($TCE = \Delta E/\Delta T$) of the constituent materials in the CMOS BEOL.

2.3 Conclusions

This work demonstrates a new class of ferroelectric-transduced RF MEMS resonators embedded seamlessly in CMOS, leveraging TI's 130 nm FeRAM technology. The magnitude of the electromechanical response can be tuned by varying poling voltages on the transducers. Due to the hysteretic effect of the ferroelectric material, the magnitude of S_{dd11} exhibits a hysteresis response with respect to changing poling voltages on the ports. The maximum Q of 1012 is

obtained with optimization of vertical and lateral confinement of the acoustic mode in the CMOS stack. This corresponds to an $f \cdot Q$ of 7.11×10^{11}.

Figure 2.11 has summarized the $f \cdot Q$ for the previous work on both pure-PZT resonators (red dots) as well as the PZT-on-Si resonator (blue dots). This performance is 1.6x higher than the state-of-the-art PZT resonators[82]–[85] with the additional benefit of CMOS integration.

The PZT material itself is typically acoustically lossy in radio frequencies. However, in this manuscript, the thickness of the PZT thin film is only about 70nm while the entire capacitor is about 500nm, and the mode extends as an evanescent tail beyond the FeCAP. From the mode shape diagram in Fig. 2.3(b), the resonant volumetric ratio of PZT to non-PZT material (with 95% strain energy concentration) is about 1%. This will boost Q relative to pure-PZT devices due to the lower viscoelastic losses of surrounding materials. However, the higher Q also trades off the performance with k^2, which is reduced substantially (0.047%) relative to pure PZT resonators.

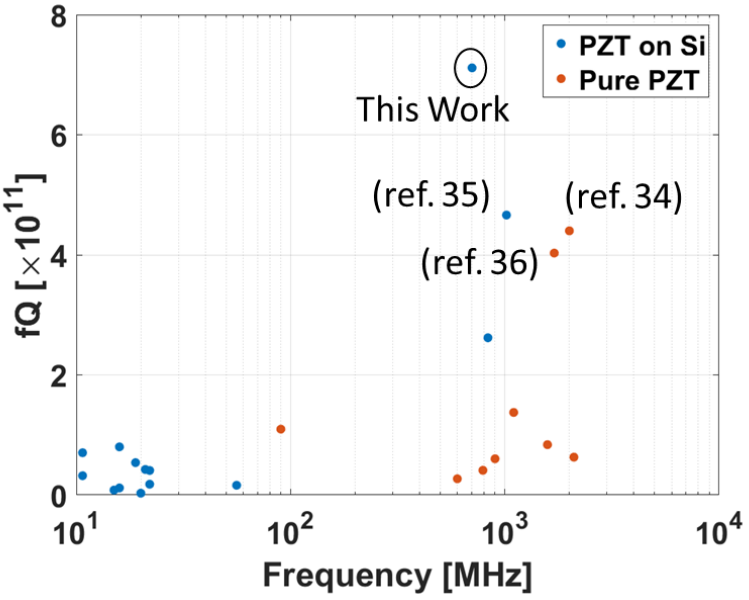

Figure 2.11 Comparison of $f \cdot Q$ with previous work

Suppression of electromechanical transduction is demonstrated when FeCAPs are biased at their coercive voltage of ±0.3V. The extracted TCF is -58.1±4.6 ppm/°C. Therefore, these devices provide a platform for applications that include but are not limited to RF components, timing, sensing, imaging, with CMOS integration.

3. SWITCHABLE MECHANICAL RESONANCE INDUCED BY HYSTERETIC PIEZOELECTRICITY IN FERROELECTRIC CAPACITORS

A version of the chapter has been reprinted with permission from IEEE Transducers 2019
Y. He, B. Bahr, M. Si, P. Ye, and D. Weinstein, "Switchable Mechanical Resonance Induced by Hysteretic Piezoelectricity in Ferroelectric Capacitors," 2019 20th Int. *Conf. Solid-State Sensors, Actuators Microsystems Eurosensors XXXIII (TRANSDUCERS EUROSENSORS XXXIII),* no. June, pp. 717–720, 2019

To address the demands of wireless communication in an increasingly overcrowded and at times hostile spectrum, researchers in the field of RF MEMS have focused on a variety of novel building blocks for opportunistic radio front ends. Next-generation of portable communication devices such as mobile phones and smart watches will require programmable multi-band operation with reduced weight, size, and cost [86]. Low-loss switchable filters composed of high-Q MEMS resonators offer a unique solution under these constraints. Traditionally, switchable filter banks incorporate non-switchable resonators and external solid-state or MEMS switches. However, that will unavoidably add insertion loss, size, form factor, and cost. To overcome some of these challenges, recent works report switchable/tunable resonators based on Gallium Nitride (GaN) [87], Zinc Oxide [88], Strontium Titanate (STO) [89], Barium Strontium Titanate (BST) [90].

As demonstrated by the introduction of ferroelectric transduction in chapter 1. Ferroelectric materials exhibit electrical polarization which can be reversed under an applied external electric field [58]. Due to this unique hysteretic behavior, these materials have been explored extensively for non-volatile memory devices [91] and are offered in production-level CMOS FeRAM processes [80]. In the meantime, this hysteretic behavior would enable the tunability of the device. The corresponding hysteresis of the piezoelectric effect in such devices has previously been investigated in various ferroelectric stacks [92]. However, detailed studies and models of the effect of this hysteresis on transmission S_{21} in 2-port resonators are sparse.

Leveraging Texas Instruments' FeRAM technology (E035), a waveguided mechanical resonance operating at around 700 MHz was demonstrated in the previous chapter [93]. The maximum Q of 1012 is obtained with optimization of vertical and lateral confinement of the acoustic mode in the CMOS stack.

In this chapter, we continue to investigate the effect of poling conditions on the FeCAP resonator RF transmission, demonstrating a bias dependent transformation of resonance peaks to zeroes, alongside an inversion of the resonance phase transition

3.1 Device Design

The cross-sectional SEM of the FeCAP resonators is shown in Figure 2.3, the structural design for which is thoroughly discussed in Chapter 3. The entire resonator is composed of an array of 20 FeCAPs with a 2 μm pitch. Each FeCAP consists of a 70 nm thick PZT layer, sandwiched between the top and bottom Ir electrodes. Two Cu strips are designed in the BEOL metallization to assist in the confinement of the elastic energy to the FeCAP areas, ensuring lower acoustic radiative loss (higher *Q*) and increasing the overlap of the transducer area with the desired mode. Dummy FeCAPs are added to either end of the resonator to reduce elastic wave scattering losses from the ends. The footprint of the device measures 7×108 μm^2.

3.2 Experimental Results

3.2.1 Experimental setup

Figure 3.1 gives a top-view schematic of the device along with the setup for the measurement. The drive (Port 1) and sense (Port 2) transducers are interdigitated along the wave propagation direction, namely, the top electrode of every other FeCAP in the array is electrically connected to one of the two ports, while the bottom electrodes of all FeCAPs are grounded together using the technology's polysilicon (poly-Si) gate layer [78]. The experimental setup shown in Fig. 3.1 differs from the one reported in the previous chapter in that each of the ports (either drive or sense) is connected to an independent DC source so that the driving and the sensing FeCAPs can be manipulated independently.

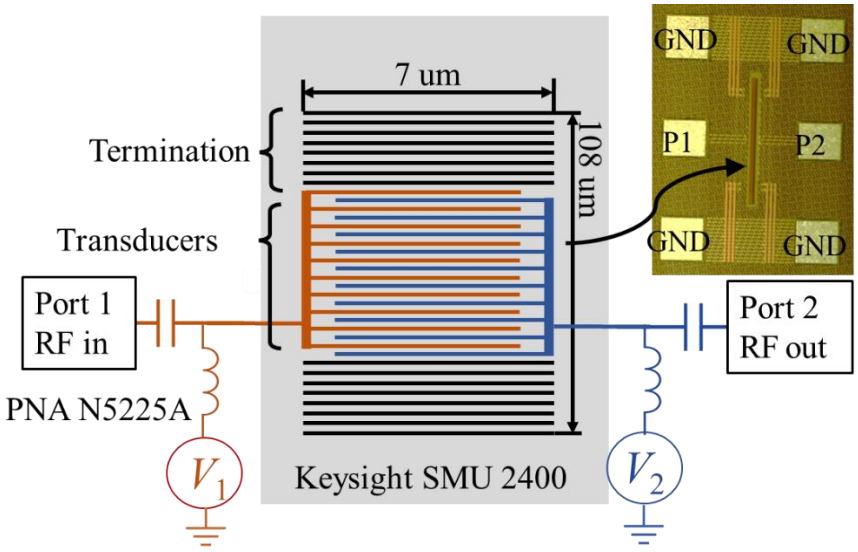

Figure 3.1 Top view schematic of the resonator in single-ended two-port RF measurement configuration [78]

Two-port single-ended *S* parameters are characterized by Keysight Parametric Network Analyzer (PNA) N5225A. Alternating FeCAPs are poled by Keysight Source Measurement Unit (SMUs). Therefore, the resonator may be configured with any combination of poling voltages V_1 and V_2 on alternating FeCAPs.

3.2.2 Resonant Pole/Zero Transition

Based on this P-E measurement (shown in Figure 2.4), two cases are first considered in Figure 3.2 as the two extremes of poling conditions within the resonator. Each square represents one FeCAP unit cell with each arrow indicating the polarization direction of the ferroelectric PZTs. Therefore, every other FeCAP can either be poled uniformly with $V_1 = V_2$ or alternately with $V_1 = -V_2$. It should be noted that alternating poling is not equivalent to periodic poling since adjacent capacitors are not electrically connected.

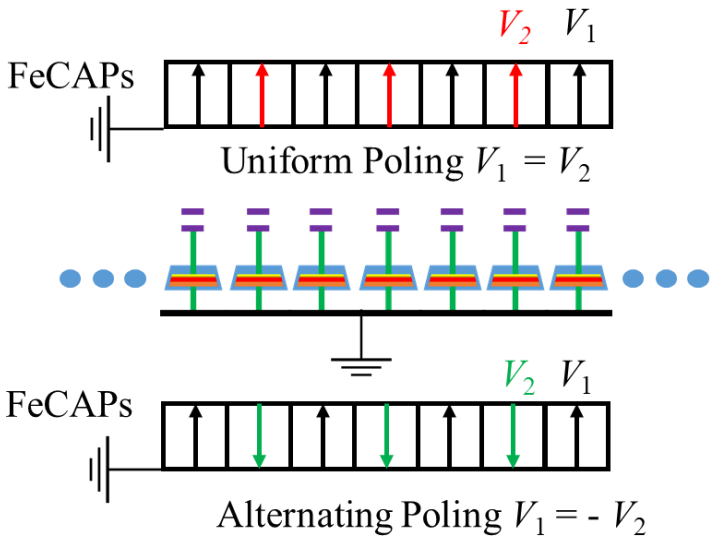

Figure 3.2 Schematic of FeCAP array under uniform poled and alternating poled bias conditions

Under the given uniform and alternating poling conditions, the transmission S_{21} is measured in the range of 650 MHz to 3 GHz (Fig. 3.3). Regions, where the peak amplitude is above the capacitive floor, are referred to as 'poles' and below as 'zeroes'. Pole/zero and zero/pole transitions and the corresponding phase shift inversion are observed for all mechanical modes relative to the capacitive floor. A finite element analysis in COMSOL Multiphysics is carried out to investigate the first pole resonance mode given by each biasing condition. As shown in Fig. 3.4, the frequency response simulation reveals waveguided FeCAP modes at 722 MHz and 1.8 GHz. The corresponding stress distribution perpendicular to the FeCAP plane is also shown to help visualize the elastic energy localization.

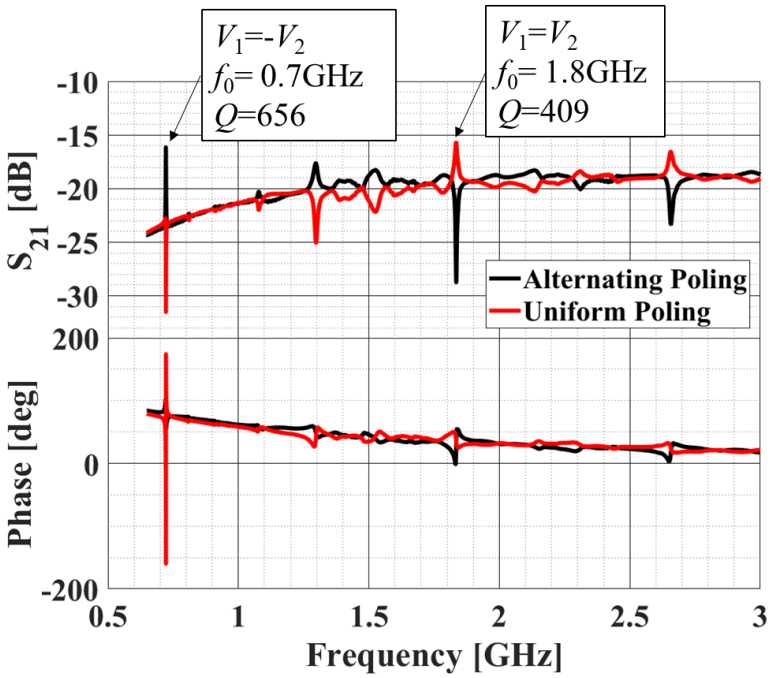

Figure 3.3 Measured S_{21} under uniform vs. alternating poling conditions

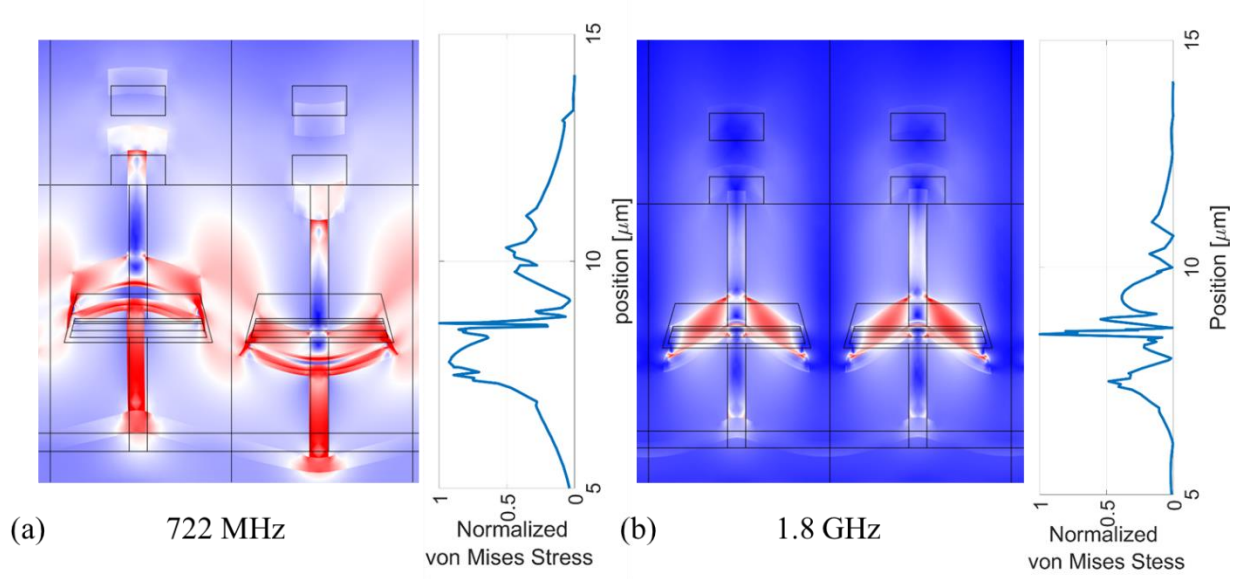

Figure 3.4 Simulated resonance modes corresponding to first measured peaks under (a) alternately poled and (b) uniformly poled resonator biasing

A closer look at the S_{21} resonance at 722 MHz with respect to the changing poling voltages is shown in Figure 3.5. In this case, port 2 is fixed at 1.5 V whereas port 1 is swept from 1.5 V

down to -1.5 V. It is observed from Fig. 3.5 that when V_1 is above the coercive voltage of -0.3 V, the resonance amplitude is above the capacitive floor. On the other hand, when V_1 is below -0.3 V, the resonance amplitude is below the capacitive floor. To quantitatively capture the changing S_{21} amplitude relative to the capacitive floor under different poling voltages, the latter is subtracted from the S_{21} peak amplitude, summarized in Fig. 3.6(a). When port 2 is biased at either 1.5 V or -1.5 V, S_{21} amplitude exhibits a symmetric non-linear "butterfly-shaped" variation with respect to changing V_1. In the meantime, as shown in Fig. 3.6(b), when V_2 is fixed at 1.5V, the S_{11} amplitude also demonstrates a non-linear butterfly-shaped variation while S_{22} gives non-zero hysteresis variation with respect to the changing applied voltages on V_1.

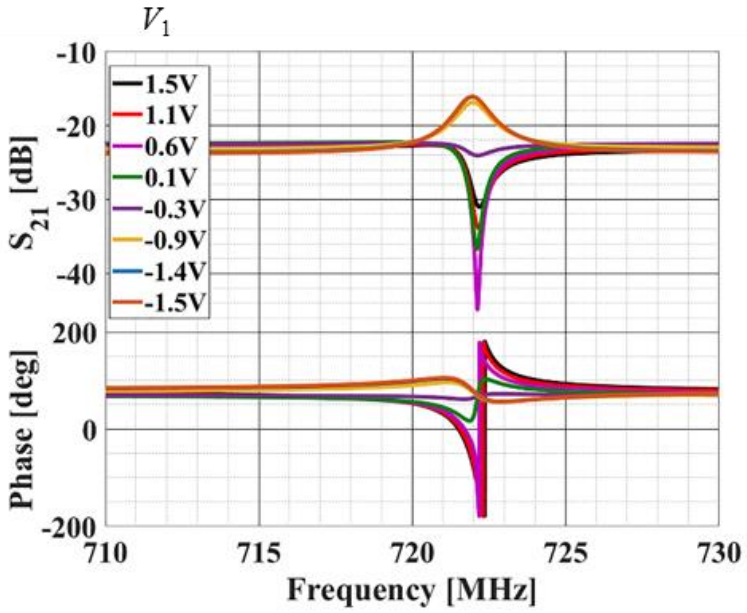

Figure 3.5 Detailed S_{21} variation with respect to the changing poling voltages where V_2 is fixed at 1.5V.

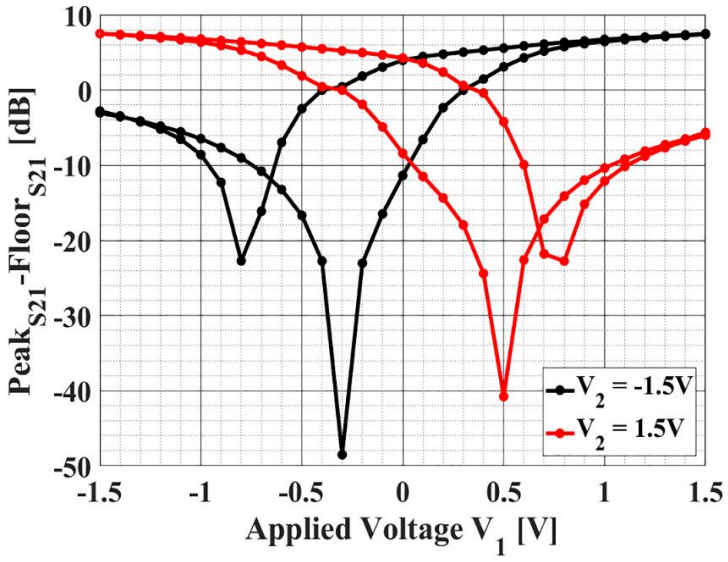

(a)

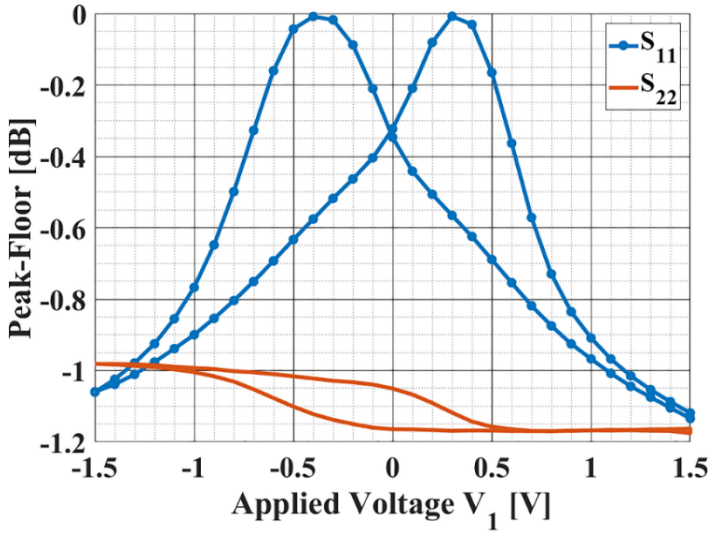

(b)

Figure 3.6 Measured pole-zero transition of 722 MHz resonance. (a) S_{21} hysteresis varying V_1 with V_2 fixed at ±1.5V. PeakS_{21}-FloorS_{21} indicates the amplitude of resonance above the capacitive floor. The transition across 0 signifies the switch from the resonance pole to zero. (b) Reflection S_{11}, S_{22} hysteresis varying V_1 with V_2 fixed at 1.5V.

3.2.3 Equivalent Circuit Model

To better understand this behavior, an equivalent two-port equivalent circuit model is developed and fitted to the experimental results using Keysight Advanced Design System (ADS).

This model is originated from the standard two-port BVD model with modifications to accommodate the voltage-dependent and hysteresis behavior of the transition. The equivalent circuit model is shown in Figure 3.7.

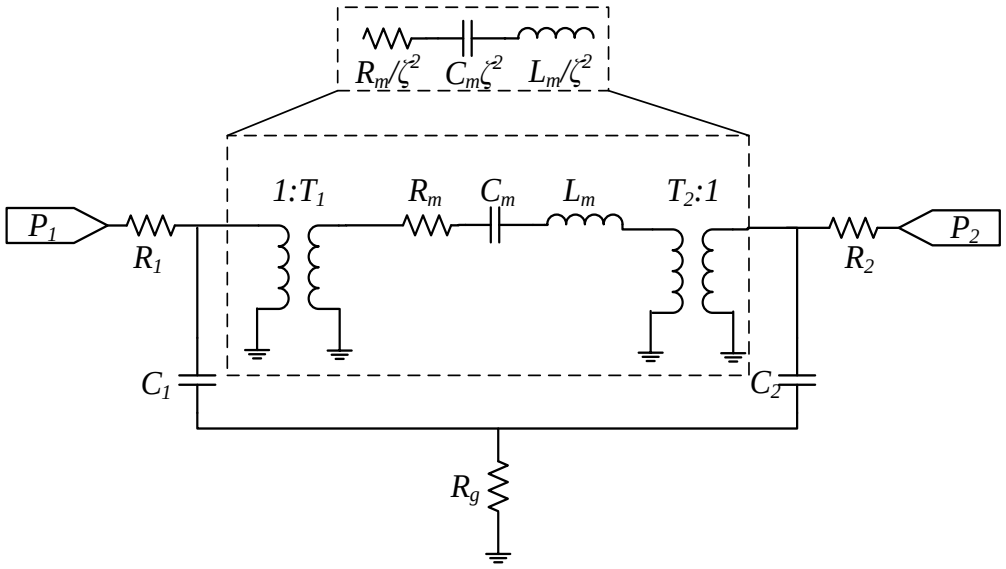

Figure 3.7 Equivalent circuit model of the FeCAP resonator

In this model, R_1 and R_2 model the electrical losses from the routing to the device. C_1 and C_2 represent the bias-dependent PZT thin film capacitance. R_m, L_m, and C_m are the resistance, inductance, and capacitance for the motional dynamics of the resonator, respectively. *Rg* captures the resistance from the poly-Si gate which is then used to ground all FeCAPs together. Two transformers with coupling coefficients T_1 and T_2 are included in the model to capture the difference in electromechanical coupling under changing biasing conditions for the PZTs. Under the circuit model shown in Fig. 3.7, the extreme condition of $V_1 = -V_2$ was first fitted as the base model. As V_2 is kept at a fixed voltage during the measurement, the coupling coefficient from port 2 remains constant across all applied voltages V_1. For simplicity, we normalize the coupling coefficients such that T_i (V_i=±1.5V)≡ ±1 for the i^{th} port (i=1 or 2). Under this assumption, the equivalent motional resistance, inductance, and conductance can be expressed as R_m/ζ^2, $C_m\ \zeta^{2,}$ and L_m/ζ^2 where

$$\zeta = T_1 T_2$$

We assume that R_1, R_2, and R_g are independent of the biasing conditions. The motional RLC branch is modulated by varying ζ. It should be noted that the sign of ζ depends on the superposition of the mode shape with the material polarization. In the case of the anti-symmetric 722MHz mode, alternating poling of the FeCAPs results in $\zeta < 0$. Conversely, the symmetric 1.8GHz mode exhibits $\zeta > 0$ under the same periodic poling conditions. The corresponding values for each circuit component under three different biasing cases are summarized in Table 3-1.

Table 3-1 Key Components for the mBVD model under three poling cases

Biasing Conditions	**V_2=1.5V, V_1=−1.5V**	**V_2=1.5V V_1=1.5V**	**V_2=1.5V, V_1=0.5V**
R_m (Ω)	374		
C_m (fF)	0.85		
L_m (μH)	57.4		
C_1 (pF)	4.47	4.42	5.51
C_2 (pF)	4.51		
R_1 (Ω)	4.43		
R_2 (Ω)	5.48		
R_g (Ω)	3.90		
ζ	1	0.873	0.796
k^2 (%)	0.047	0.036	0.027

Based on the parameters in Table 3-1, a fitted S_{21} to the measurement results under two extreme biasing conditions is shown in Figure 3.8. The S_{21} from the equivalent circuit agrees well with measurement.

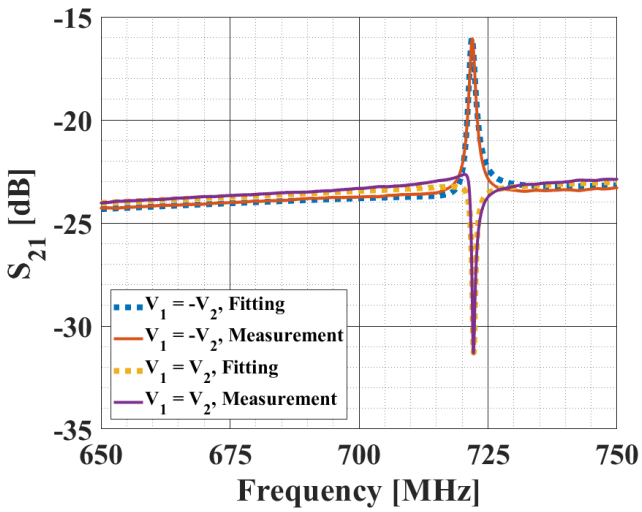

Figure 3.8 Fitted S_{21} parameters under two extreme biasing conditions

3.2.4 Principle of Resonant Pole/Zero Transition

With respect to changing the bias on port 1, the corresponding ferroelectric capacitance exhibits a non-linear variation shown in Figure 3.9(a). When the applied voltage is varied between -1.5 to1.5V, the ferroelectric capacitance changes between 4.4 to 6.4 pF. Figure 3.9(b) summarizes the variation of ζ under different biasing conditions at port 1.

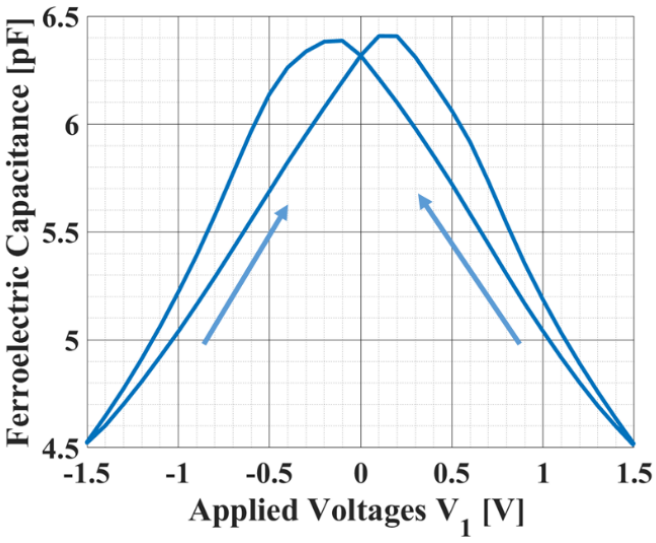

(a)

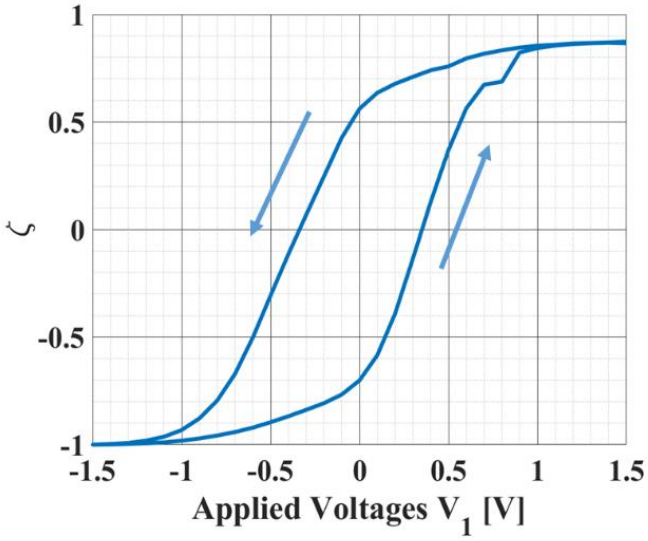

(b)

Figure 3.9 (a) Variation of ferroelectric capacitance and (b) variation of ζ under different applied voltages.

Depending on the polarization direction of the ferroelectric PZTs, ζ changes sign at the coercive voltage of ±0.3V, inducing the cancellation of motional and feed-through currents which leads to the pole/zero or zero/pole transition [94]. The combination of changing C_1 and T_1 defines either motional or the feedthrough currents dominant. If the motional current is larger than the feedthrough current, the transmission S_{21} amplitude exhibits a pole. If on the other hand, the

feedthrough current is greater than the motional current, the transmission S_{21} tends to be flat. When the currents in both branches are out of phase with one another with the same amplitude, they will cancel and generate a zero in the transmission. With V_2 fixed at 1.5V, two additional transition points at 0.5V and 0.8V are obtained. The same explanation can be applied when V_2 is biased at -1.5V, for which transitions at -0.3V and -0.8V are obtained [78].

3.3 Conclusions

We have demonstrated a two-port ferroelectric capacitor-based resonator with a resonance frequency of 722 MHz, Q of 656, and k^2 of 0.047%. The bias-dependent pole/zero transition of the resonance has been studied across the full hysteretic loop of the device. In two extreme cases where $V_1 = V_2$ and $V_1 = -V_2$, pole/zero and zero/pole transitions along with the phase shift inversion are observed. When port 2 is biased at a fixed voltage of ±1.5 V, the transmission S_{21} amplitude demonstrates a symmetrical non-linear "butterfly-shaped" variation with respect to the changing V_1. A modified BVD model is presented to explain the phenomenon. Due to the changing polarization of the PZT, ζ changes sign at ±0.3 V, inducing cancellation of current in motional and feedthrough branches which then leads to the observed pole/zero and zero/pole transition. The combination of the changing ferroelectric capacitance and ζ determines the maximum cancellation of current between two branches, corresponding to the minimum S_{21} or largest zero. This class of ferroelectric resonators offers a dynamically tunable RF building block for various configurable front-end topologies.

4. ACOUSTIC METAMATERIALS FOR ON-CHIP MECHANICAL SIGNAL PROCESSING

4.1 Acoustic Metamaterial (AM)

Chapter 1 has introduced the application of SAW and BAW in mechanical signal processing, especially in cellular or base station RF front-end communications. In the follow-up chapters, we have also demonstrated the first of its kind of piezoelectric mechanical resonator which is seamlessly integrated within standard CMOS processes.

In addition to the traditional SAW or BAW approach, phononic crystal (AM) or acoustic metamaterials (AM) has recently been proved to be an effective approach in mechanical signal processing [36]. Acoustic metamaterial refers to certain types of artificial material or structure which has periodic acoustic properties and present unprecedented physical phenomenon [95]–[97]. The concept of phononic crystals is proposed around 1992 by Sigalas and Economou [98] where materials/structures can be formed in a certain periodic form so that mechanical waves of a certain frequency range can theoretically be prohibited from propagating through. Analogous to the bandgap in an *E-k* diagram in semiconductor physics, that frequency range is referred to as mechanical/elastic bandgap. It was not until 1995 when sound attenuation was found behind a sculpture in Madrid before the existence of a mechanical bandgap is confirmed [99].

Figure 4.1 Sculpture by Eusebio Sempere in Madrid formed by the periodic distribution of hollow stainless-steel cylinders [99].

Upon confirmation of the existence of mechanical bandgap, phononic crystal or acoustic metamaterial has been actively explored both theoretically and experimentally over decades. At the early stage, on the modeling side, different approaches have been put forward to theoretically calculate the mechanical bandgap including transfer matrix method, plane wave expansion method, finite-difference time-domain (FDTD) method, finite element analysis (FEA) method, etc. [100]. Generally, for sufficient small strain, the relationship between the strain and displacement can be expressed as

$$S_{ij} = \frac{1}{2}\left(u_{i,j} + u_{j,i}\right) \tag{4-1}$$

where *S* represents the strain tensor and *u* is the displacement vector.

Moreover, the generalized stress-strain relationship can be given by Hooke's law:

$$T_{ij} = c_{jikl} S_{kl} \qquad \forall i,j,k,l \in \{1,3\} \tag{4-2}$$

Where *T* and *S* represent the stress and strain tensors respectively. Owing to the symmetry of the stress and strain tensors, we could have

$$c_{jikl} = c_{ijlk} = c_{jikl} = c_{jilk}$$

Also, under the elastic energy conversation, one will have

$$c_{ijkl} = c_{klij}$$

Finally, the governing equation for the system assuming zero body force can be expressed as

$$T_{ij,j} = \rho \ddot{u}_i \tag{4-3}$$

Substituting Eqn. (4-1) into (4-2) and then into (4-3), one can obtain

$$\rho \ddot{u}_\iota = \sum_{j=1}^{3} \{ \frac{\partial}{\partial x_i} \left(\lambda \frac{\partial u_j}{\partial x_j} \right) + \frac{\partial}{\partial x_j} [\mu (\frac{\partial u_i}{\partial x_j} + \frac{\partial u_j}{\partial x_i})] \}$$

$$\forall i, j \in \{1,3\} \tag{4-4}$$

Where λ and μ are Lame constants which correlate with the longitudinal and transverse velocity as:

$$C_l = \sqrt{\frac{\lambda + 2\mu}{\rho}}$$

and

$$C_t = \sqrt{\frac{\mu}{\rho}}$$

The Floquet periodic boundary condition can be expressed as

$$\vec{u}_R(\vec{r}) = \vec{u}_L(\vec{r}) \cdot e^{-i\vec{k}\cdot\vec{r}} \tag{4-5}$$

Substitute Eqn. (4-5) into Eqn. (4-4) and expand it along the first irreducible Brillouin zone, one can come up with an equation with the form of

$$(\boldsymbol{K} - \omega^2 \boldsymbol{M})\boldsymbol{U} = 0 \tag{4-6}$$

by searching along the first irreducible Brillouin zone for the eigenfrequency (from Eqn. (4-6)). The corresponding dispersion relationship can be obtained.

However, with more and more complicated and novel devices been proposed, it is not always straightforward to find the analytic solution for the bandgap. Instead, multiple numerical methods including FDTD and FEA are widely deployed [101].

4.2 Mechanical Bandgap

One of the unusual physical phenomena induced by AM is the associated adjustable mechanical bandgap produced by either Bragg scattering or the local mechanical resonance[102].

The observed mechanical modes which satisfy the Bloch periodic boundary condition (Eqn. (4-5)) are typically referred to as Bragg modes generated by Bragg scattering within the lattice. As a result of the phonon-phonon scattering effect, the Bragg scattering induced bandgap generally appear at relatively high frequencies and the bandgap typically has large width.

Besides, by coating hard scatterers with soft materials (or vise versa), Liu et. al.[103] introduced local resonance within the acoustic metamaterial (Fig. 4.2).

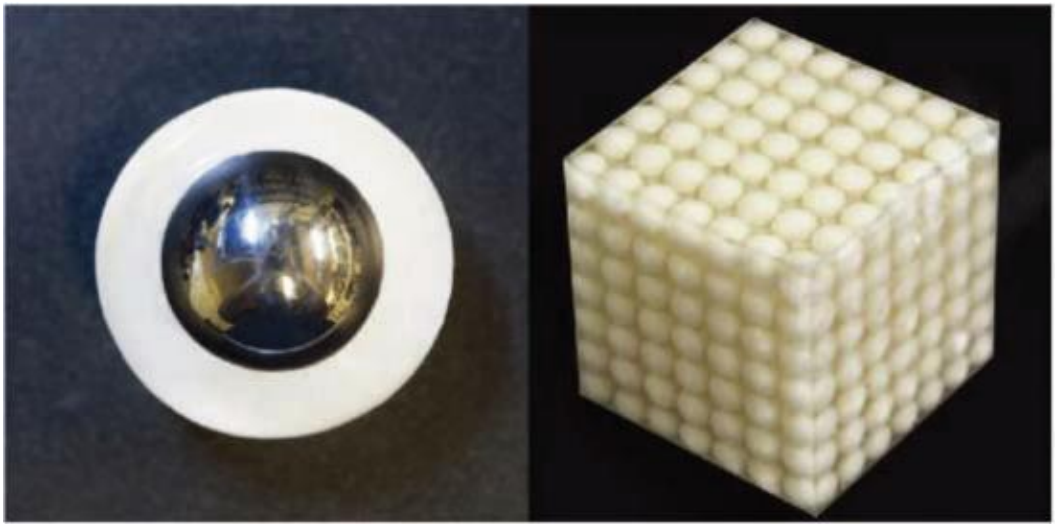

Figure 4.2 Image of acoustic metamaterial with bandgap induced by local resonance [103]

Since these local resonances are induced by the unit cell component, the width and location of the generated bandgap depend more on the unit cell geometry but less on the periodicity of the overall structure. Also, as the corresponding wavelength of the mechanical resonance could be more than one lattice constant, it provides possibilities of generating bandgap at super-low frequencies.

Leveraging both the Bragg scattering and local resonance, acoustic metamaterials have been widely used in RF MEMS communities, especially to boost the energy confinement, reduce the mechanical losses or remove the spurious mode. Therefore, the following subsections will introduce few efforts of integrating AM within traditional RF devices.

4.2.1 AM as *Q* Boosters for Traditional SAW and BAW Resonators

As indicated before, within the mechanical bandgap, elastic waves of certain frequencies are forbidden from propagating but reflected back to the resonant bulk. Therefore, one of the major

applications of acoustic metamaterials in the MEMS field is to collect the leaked energy, thus increase the energy confinement for MEMS resonators - to boost the *Q*.

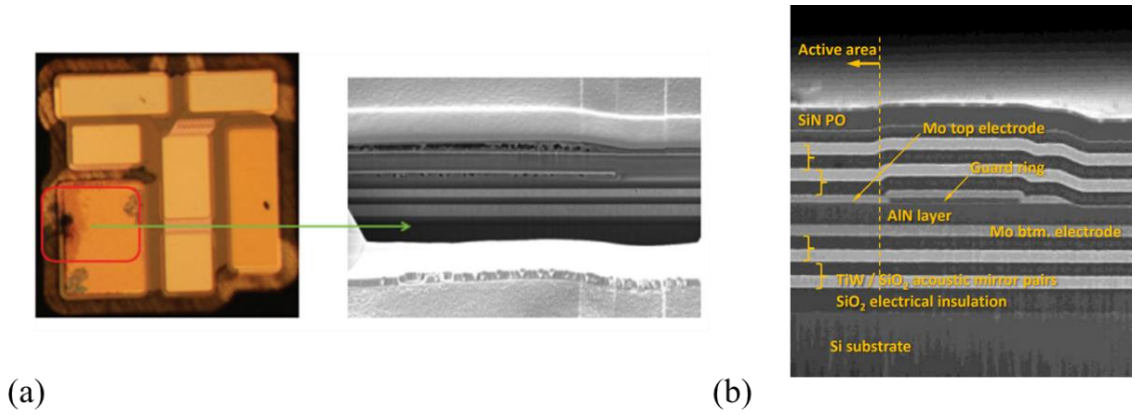

Figure 4.3 Example of integrating 1D acoustic metamaterials – Bragg mirror as reflectors at (a) bottom side of the resonant thin film [104] and (b) both sides of the thin resonant film [105]

To start with, there have been efforts of integrating 1D acoustic metamaterial, namely the Bragg mirror into the traditional resonant thin film. As illustrated by Fig. 4.3, the Bragg mirror is typically formed by multiple alternating layers either at the bottom of thin-film (Fig. 4.3(a)) or on both sides of the thin film (Fig. 4.3(b)). Each of the reflecting layers has a thickness of quarter wavelength. Hence, the incident and reflected wave will cancel with each other and form a mechanical bandgap. Moreover, the adjacent layers typically have a large impedance mismatch between each other, maximizing the amount of energy been reflected from the mirror and thus further increasing the *Q*. So far, the idea has been widely applied in 5G related commercial mass production formed as solidly mounted resonator [105]–[109]. The Bragg mirror technology has released the original fabrication challenges for BAW resonators. Compared to more traditional air gaps, the Bragg mirror integrated resonator would no longer require any releasing steps or vacuum condition for the follow-up packaging.

The 1D acoustic metamaterial has been proved to be effective to confine out-of-plane wave propagation. Besides, there are also a bunch of 2D designs that are capable of confining in-plane wave motion.

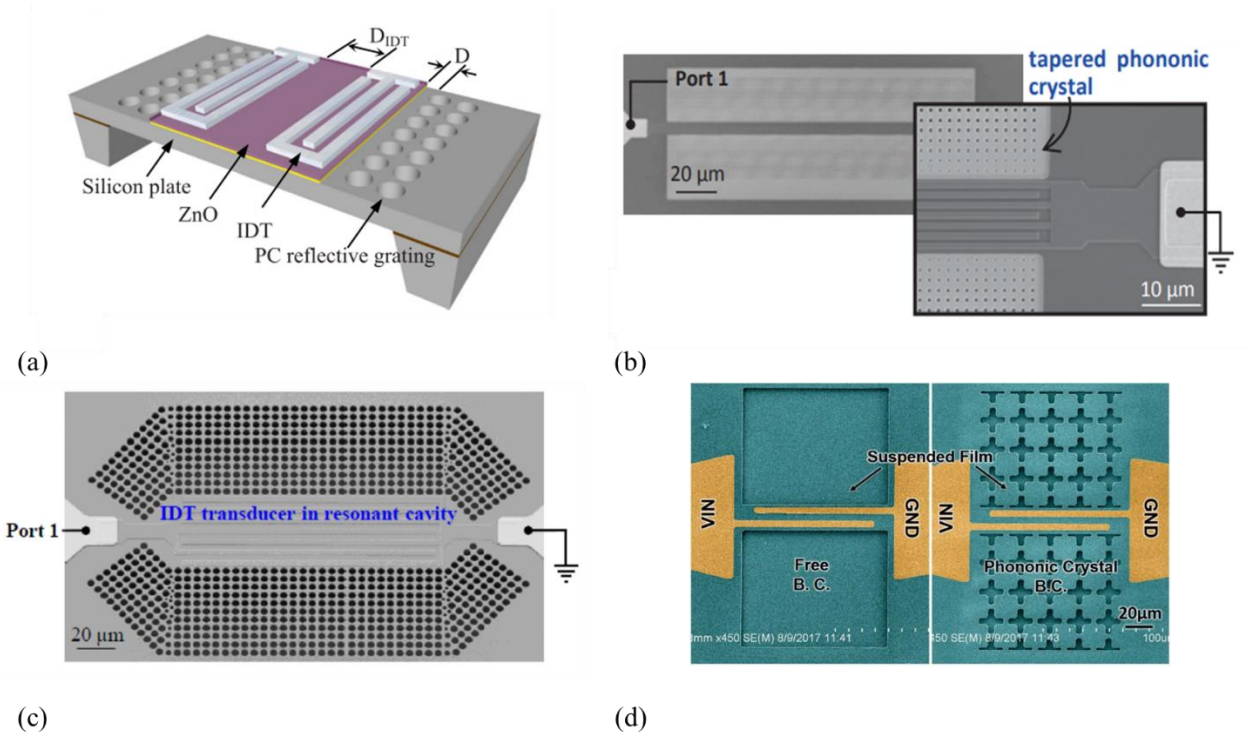

Figure 4.4 Examples of acoustic metamaterials integrated with (a) Lamb mode ZnO resonator [55] (b) Lamb mode GaN resonator [110] (c) SAW GaN resonator [111] (d) Lamb mode lithium niobate resonator [112] as reflective boundaries.

Shown in Fig. 4.4 are few successful examples of integrating 2D acoustic metamaterials as reflecting boundaries to confine in-plane waves in normal SAW or BAW resonators. Chao-Yi et. al. placed periodic cylinders as acoustic metamaterial reflective grating at the side of the ZnO lamb mode resonator. The maximum *Q* obtained is about 2200 at 158 kHz [55]. More recently, Siping et. al. pattern periodic cylinders across GaN lamb mode resonators. The maximum *Q* obtained is around 3079 [110]. Also, by placing periodically deep-etched holes along the surface wave propagating direction around GaN SAW resonators, the *Q* can be boosted by 10x from 246 to 2600 [111]. More recently, Ruochen et. al. demonstrated a similar design by putting cross-shaped deep-etched holes at the side of the $LiNbO_3$ resonator forming an acoustic metamaterial reflective boundary.

In addition to designing proper reflectors to boost the *Q*, there are also few works reporting the efforts of integrating AM as tethers for resonators. As anchor loss represents the mechanical energy leakage towards the supporting plane as well as the substrate and is regarded as one of the major loss mechanisms in MEMS resonators. The fundamental design process is analogous to AM

reflectors where the mechanical bandgap is designed with the center frequency at or around the resonant frequency. By replacing the more traditional quarter wavelength beam tether with AM strips, the corresponding *Q* can be boosted for around 50% - 100% [113]–[117].

4.2.2 AM Resonators

The previous section has illustrated efforts of utilizing AM as either reflectors or tethers to boost *Q* for traditional devices. The resonant frequency is typically designed within the Bragg scattering-induced bandgap. Yet, the mechanical resonance does not necessarily need to be induced by traditional SAW or BAW devices, as mentioned at the beginning of this section, mechanical resonance can also be introduced by AM itself. One of the effective approaches to generate AM resonance would be breaking the original periodicity of the matrix and introducing the "defect" mode. Shown in Fig. 4.5 are few examples of AM resonators. The mechanical resonance in these cases is induced by the "defects", namely, by breaking the original periodicity of the lattice.

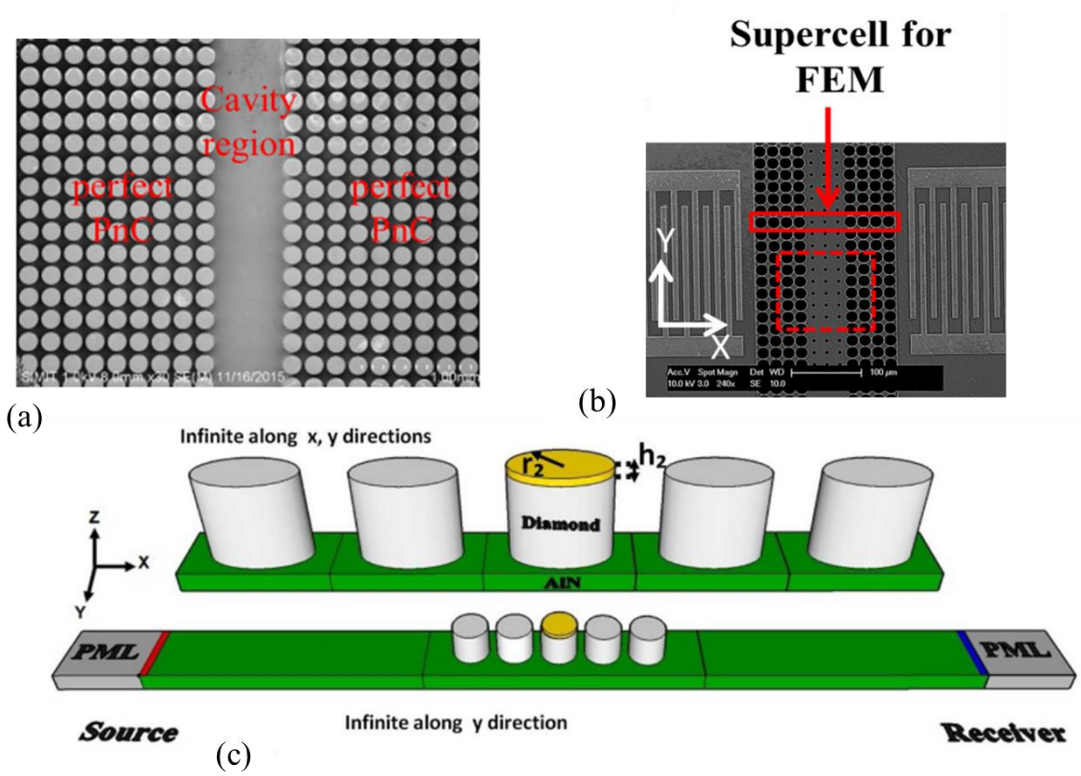

Figure 4.5 Example of AM resonators. The mechanical resonance is induced by introducing a "defect" within the AM matrix. The "defect" can be obtained by (a) removing few units inside the periodic structures [118] (b) adding few units but with different geometry [119] (c) adding few units but with different material [120].

Primarily, the "defect" can be introduced by removing one or few unit periods (Fig. 4.5(a)) [118]. The resonant frequency of the cavity region should be designed within the bandgap of the surrounding matrix. Moreover, the "defect" can also be introduced by replacing one or a few original metamaterial units with different geometry or materials (Fig. 4.5(b – c)) [119], [120]. The resonant frequency of the "defect" is directly related to the geometry and material of the bulk materials. The resonant frequency typically lies in the bandgap of the original AM. Therefore, the generated wave can be directly confined from the surrounding AM matrix.

4.3 Negative Refraction (NR)

In addition to the mechanical bandgap, another unusual physics induced by the AM would be the negative refraction (NR) effect [95], [121]–[124]. Generally, two approaches have been

reported to obtain the negative refraction effect, namely, by introducing local resonance or by multiple Bragg scattering.

One of the major applications for the NR effect of AM would be the lensing effect. The lens is widely used for either focusing or dispersing the electromagnetic or acoustic wave. When an acoustic wave propagates from one media to the other, under traditional Snell's law, the tangential component of the wave vector must be conserved as the wave propagate from one medium to another [97], [125].

As demonstrated by Fig. 4.6(a), if a wave is propagating from liquid to solid, due to different acoustic impedance, refraction will occur at the liquid/solid interface. The wave motion should satisfy the following equation [125]:

$$k_1 \sin(\theta_1) = k_2 \sin(\theta_2) = k_2^t \sin(\gamma_2) \tag{4-7}$$

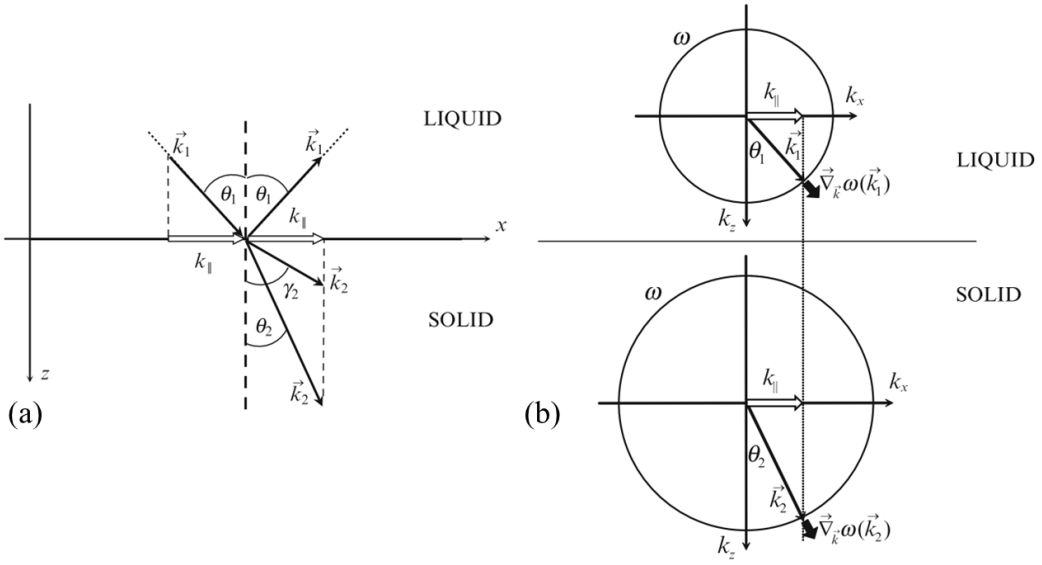

Figure 4.6 (a) Illustration of normal wave refraction (b) equifrequency contour in normal material in liquid and solid [97]

Thus the corresponding group velocity

$$v_g = \nabla_k \omega(\overrightarrow{k}) \tag{4-8}$$

which characterizes the energy flow direction is always in parallel with the wave propagating direction (characterized by $\vec{k}$), leading to a positive refractive index. As a result, the refractive wave and incident wave are on different sides of the normal axis with the incident wave angle

equal to the refractive wave angle. To focus or disperse an acoustic wave, the lens needs to be curved.

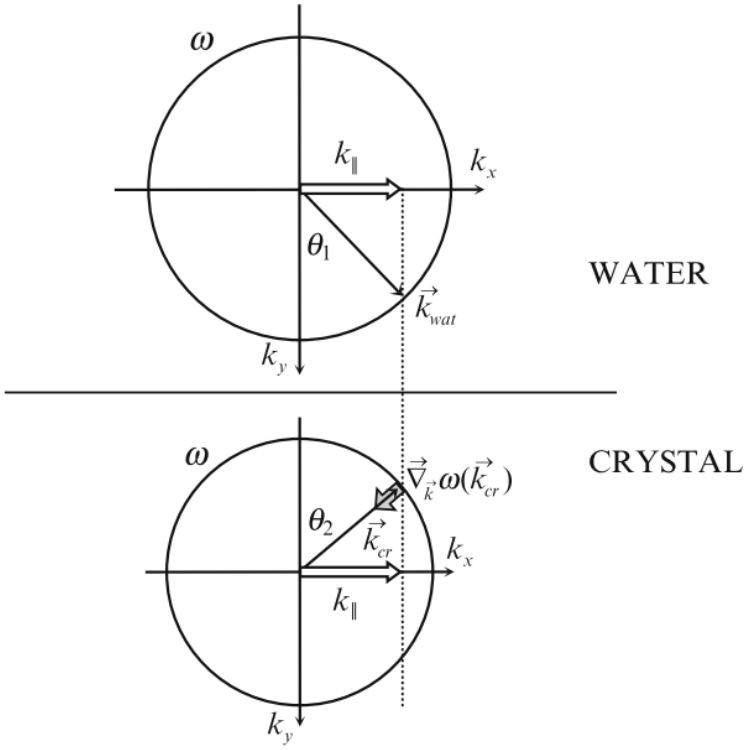

Figure 4.7 Schematic of negative refraction [97]

However, if under some circumstances, the refractive index can be negative, namely, the angle between the group velocity and wave vector is greater than 90°, as demonstrated by Fig. 4.7, according to Snell's law, the refractive wave could be obtained on the same side as the incident wave about the normal axis. As a result, the acoustic waves can be focused or dispersed using a flat lens.

4.3.1 NR Induced by Local Resonance

As already mentioned in the previous subsections, coating the hardcore with some soft shield is likely to introduce local resonance within the unit cell, leading to mechanical resonance induced bandgap. In addition, according to Newton's second law, a mechanical resonance would

induce a 180-degree phase shift between the stress and displacement vector, resulting in energy flow and wave propagation being anti-parallel with each other.

Over the past decade, there have been several successful demonstrations of negative refraction based on local resonance (examples shown in Fig. 4.8) [126]–[129]. Croenne et. al. presented a two-dimensional AM with steel rods embedded in epoxy forming a triangular lattice [127]. For the specific AM resonant mode, Fig. 4.8(a) illustrates the corresponding equivalent frequency contour (EFC) across the Brillouin zone. Interestingly, in this case, the thick black curve represents a higher frequency contour in *k*- space whereas the thin black curve indicates the low frequency, that is, the acoustic energy band is concave around Γ point ((0,0) in *k*- space). Also, the EFC presents an isotropic circular shape. This indicates that, in arbitrary wave propagation direction, the wave vector is always in anti-parallel with the energy flow direction. This has been served as a necessary condition for the negative refraction. Fig. 4.8(b) achieved negative refraction for longitudinal waves [127] and Fig. 4.8(c) presents the same effect but for shear-horizontal transverse wave [128].

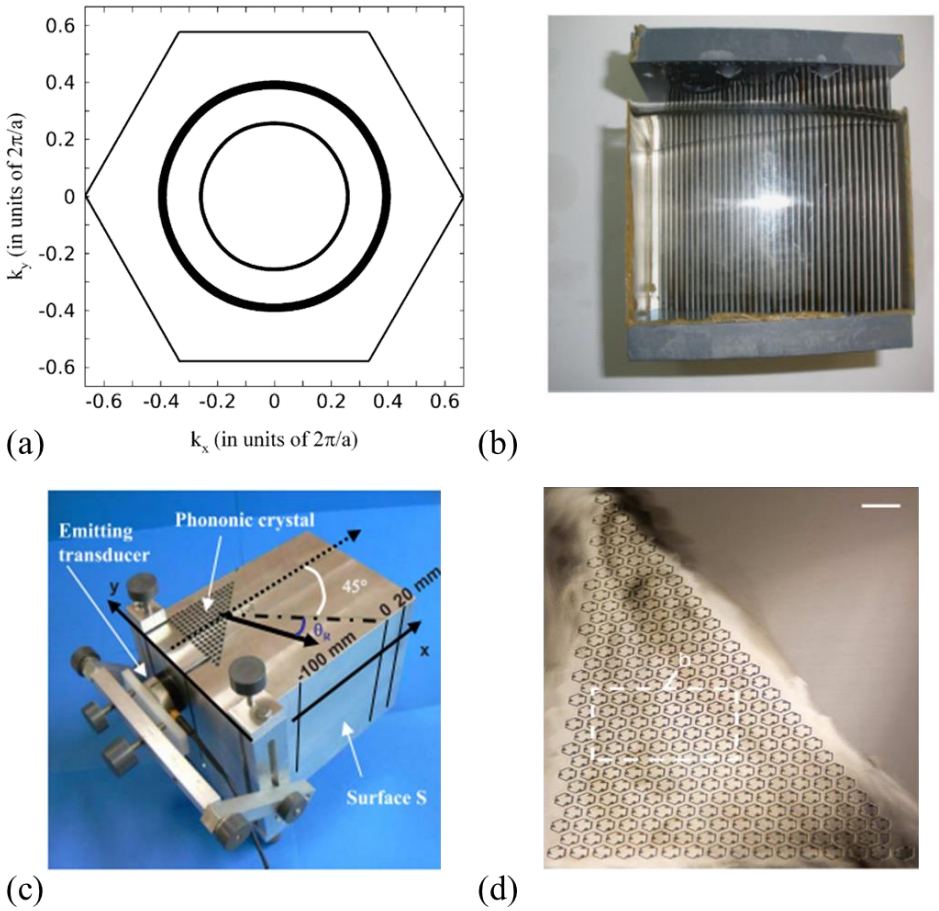

Figure 4.8 Examples of negative refraction induced by local resonance where (a) the group velocity is antiparallel with the wave-vector (thicker curve represents the higher frequency and thinner curve shows the lower frequency) [127]. The local resonant mode is associated with (b) longitudinal [127] (c) shear-horizontal [128] and (d) rotational mechanical motion [130].

While the local resonance can be achieved as a result of acoustic impedance mismatch among multiple components (hardcore with soft shells or soft cores with hard shells etc.), it can also be generated from the specifically designed single component [130]. After the etching part of the aluminum plate, a rotational motion can be induced from a central symmetrical chiral microstructure, leading to the negative refraction (Fig. 4.8(d)). The negative refraction obtained by local resonances in Fig. 4.8 all have corresponding frequency contour concaved at Γ point and satisfy the same condition between the wave vector ($\vec{k}$) and energy flow (characterized by Poynting vector $\vec{S}$):

$$\vec{k} \cdot \vec{S} < 0 \tag{4-9}$$

4.3.2 NR Induced by Multiple Bragg Scattering

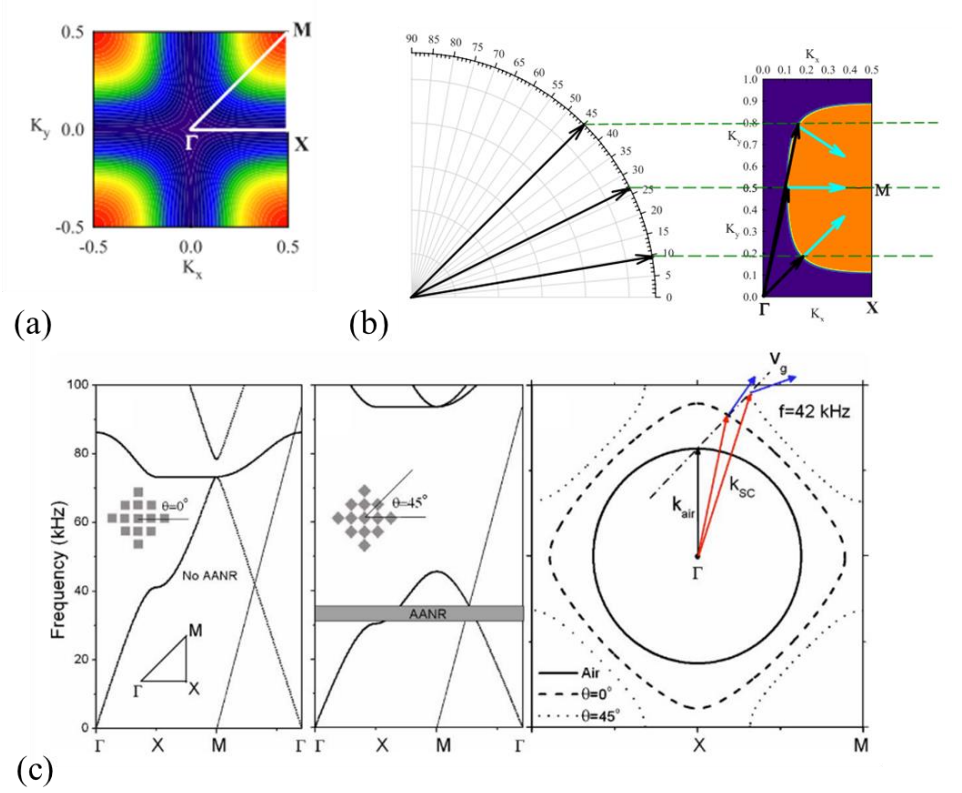

Figure 4.9 Examples of negative refraction induced by multiple Bragg scattering within the lattice (a) Corresponding EFC with energy band convex around M [131] (b) with different incident angle, the refracted wave can be switched between positive, zero, and negative index [131]. (c) the refractive index can be tuned by rotating non-circular scatterers [132].

However, Eqn. (4-9) does not necessarily need to be held. The negative refraction can also be achieved by multiple Bragg scattering amongst the periodic units with corresponding frequency contour concaved at points other than Γ in $\vec{k}$ space.

Fig. 4.9 illustrates few possibilities of obtaining negative refraction with circular (Fig. 4.9(b)) and non-circular (Fig. 4.9(c)) scatterers. However, in these cases, the corresponding EFCs are all maximized at the *M* point. While the wave is incident at Γ point with zero initial phases in either *x* or *y* directions, the Poynting vector always points towards a high energy point (*M* point in this case). With different incident angles around Γ, it is possible to vary the angle between $\vec{k}$ and $\vec{S}$ from 0 to 180 degrees (as shown in Fig. 4.9(b)). As a result, corresponding to the different

incident angle, the refracted index can be switched from positive, zero to negative values. Similarly, as demonstrated in Fig. 4.9(c), under the same incident angle but by rotating the non-circular scatterers, a tuned refractive index can be obtained.

4.4 Conclusion

Leveraging the low velocity and low propagation losses, signals superimposed on top of mechanical waves can be transmitted, confined, and finally processed in short distances on-chip. This chapter has mechanical signal processing approaches using acoustic metamaterials.

Compared with the traditional SAW or BAW approaches, acoustic metamaterial's unique physical properties such as mechanical bandgap and negative refractive index can offer unconventional measures for the manipulation of acoustic waves. The artificial composite material can break some conventional physical limits (e.g. diffraction limits) and achieve high resolution while greatly reducing the footprint of the devices[121], [123], [124], [133]. In the following chapters, simulation and implementation of acoustic metamaterials for acoustic wave manipulation will be presented.

5. LOCALIZED RESONANCE IN ALUMINUM NITRIDE BASED ACOUSTIC METAMATERIAL

A version of the chapter has been reprinted with permission from IEEE IFCS 2020
Y. He and D. Weinstein, "Localized Modes in Asymmetric Phononic Crystals," *2020 Joint Conference of the IEEE International Frequency Control Symposium and International Symposium on Applications of Ferroelectrics (IFCS-ISAF)*, Keystone, CO, USA, 2020, pp. 1-4, doi: 10.1109/IFCS-ISAF41089.2020.9234866.

Research in mechanical signal processing has blossomed due to its strong potential for simplifying and improving the efficiency of processing functions that would be otherwise computationally taxing using standard electronic-based analog or digital algorithms. Leveraging low wave velocity and low propagation loss in high-quality materials, mechanical signals can be transmitted, confined, or processed on-chip with short distances relative to their electrical counterparts. Some successful signal processing examples have been put forward in microelectromechanical system (MEMS) – in a variety of material platforms and a wide range of frequencies over which solutions have been developed [12], [20], [78].

One challenge of mechanical signal processing lies in the efficiency of conversion between the electrical and mechanical domains. Complex systems that require multiple processing elements typically use each electromechanical component independently, with input and output signals in the electrical domain, and those signals sent by metal wires to the next component. When the signal is transferred from one domain to the other, there is an inefficiency associate with the process, corresponding to energy loss. Instead, it is desired to reduce the number of conversions – keeping the signal in the mechanical domain for more signal processing steps. This necessitates a material that will effectively manipulate or transmit on-chip mechanical waves, with minimal propagation loss and effective control of dispersion and phase.

Chapter 4 has already described the unique property which acoustic metamaterials can induce in non-reciprocal wave propagation, elastic wave manipulation [77], and confinement[134]. Leveraging a Dirac-like cone developed under centrosymmetric AM matrix, physical phenomena such as negative refraction and flat-band resonance have recently been reported [135], [136].

Specifically, a flat-band mode within the dispersion relationship can provide dispersion and phase control. A flat band across the entire Brillouin zone indicates a zero group velocity whereas

a flat band across Γ point denotes infinite phase velocity, namely zero phase change across the structure. Unlike previous Dirac-like cone approaches where the structure must be centrosymmetric [136], [137], in this chapter, an asymmetric unit cell is considered to generate a flat-band mode. This is achieved by introducing an angled central beam within a square lattice cylinder matrix. The dispersion relationship of the resulting model is engineered to form a near-flat energy band within a bandgap. The desired mode is verified experimentally and studied first using AlN-based resonators. Effects of cavity size and AM unit cell geometry on resonator performance are investigated.

5.1 AM Based Resonator Design

5.1.1 Acoustic Metamaterial Design

The unit cell for the proposed asymmetric AM is shown in Fig. 5.1 (a). Dimensions of the structure are chosen based on practical considerations for fabrication. The lattice constant is a=33 μm. Each unit consists of four 90° circular sectors at the corners with a radius of 13.2 μm. The sectors are connected with three 2.64 μm wide beams - two horizontal beams connecting sectors left to right, and one diagonal bridging top left and bottom right sectors. Eigenmode analysis along the first Brillouin zone (Fig. 5.1(b)) in COMSOL Multiphysics Finite Element Analysis (FEA) reveals the function of the structure's constitutive components in forming the desired flat-band mode (Fig. 5.2). A vibrational mode is identified within a bandgap, in which the diagonal beam generates an isolated flexural resonance while the square lattice of sectors determines the width and position of the bandgap. The flexural beam mode is identified within the bandgap. The position of the flexural beam mode within the bandgap depends on the angle of the central diagonal beam. The dispersion relations for $\beta = 20°$, $\beta = 35°$ and $\beta = 45°$ are shown in Fig. 5.2. In all of these cases, a near-flat mode is observed inside the AM bandgap spanning 81 MHz and 149 MHz, characterized by the second harmonic flexural mode of the diagonal beam (Mode 1 in Fig. 5.2).

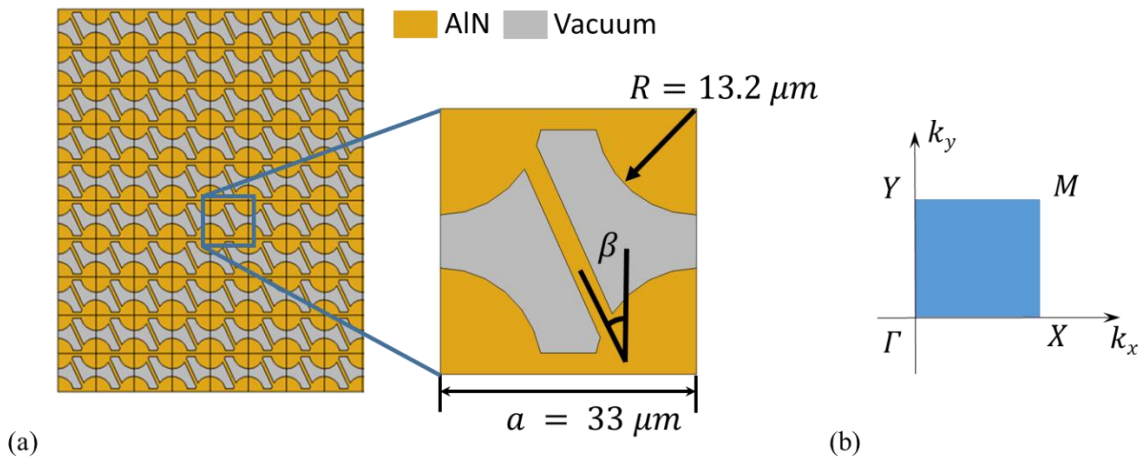

Figure 5.1 (a) Schematic of asymmetric AM unit cell where the yellow region represents the AlN stack and grey are the vacuumed places. (b) Reciprocal *k*-space and irreducible first Brillouin zone.

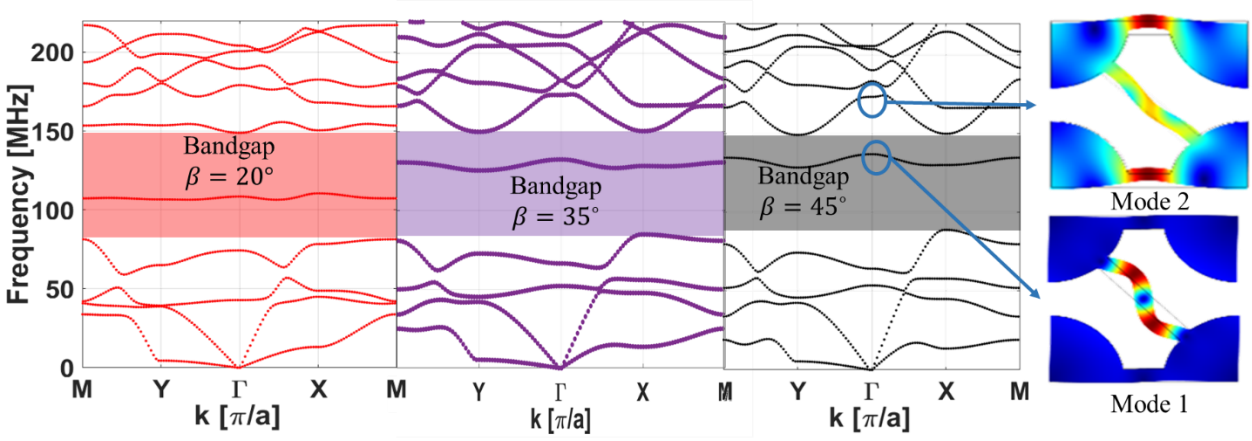

Figure 5.2 Dispersion relation along the first Brillouin zone with the diagonal bar rotation angle $\beta = 20°, 35°, 45°$ in red, purple and black, respectively. A near-flat flexural beam mode (Mode 1) is isolated within the bandgap.

Besides, the previous study only captures the characteristics of the AlN under the plane strain assumption that the third dimension is uniform and much larger than the in-plane dimension. However, in the actual device, a 200 nm Mo and a 100 nm AlN seed layer are below the main piezoelectric AlN film. Therefore, to accurately capture the corresponding mode shape, the unit cell eigenmode is studied in 3D analysis with the bottom Mo and AlN seed layers included. The top and bottom surfaces are kept as free boundaries whereas the rest of the boundaries remain under Floquet periodic boundary conditions.

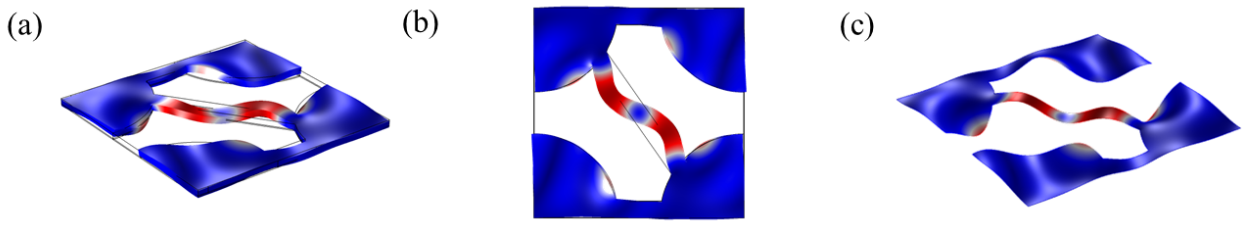

Figure 5.3 (a) Corresponding 3D mode shape with $\beta = 35°$ (b) Same mode shape with only in-plane displacement (c) Same mode shape with only out-of-plane displacement

Shown in Fig. 5.3 is the corresponding eigenmode shape for Mode 1 with the bottom metal and seed layers taken into consideration. In order to better understand the mechanical motion of the given mode, mechanical motion for mode 1 is split into in-plane motion as well as the out-of-plane motion. Fig. 5.3(b) illustrated the in-plane displacement field whereas Fig. 5.3(c) shows the out-of-plane displacement field. The in-plane motion agrees well with the previous 2D analysis (Fig. 5.2). Apart from the in-plane motion, under the Poisson's effect, the mechanical mode also generates the out-of-plane motion, of which the displacement field is plotted in Fig. 5.3(c). The out-of-plane displacement field is formed as an "M" shape with maximum energy localizing at about a quarter length from both ends of the central beam. Therefore, the corresponding mode can be driven by the uniform electrode at the top and bottom of the AlN thin film.

5.1.2 Fabrication Process

Devices were fabricated in Birck Nanotechnology Center at Purdue University. The microfabrication process flow is illustrated in Fig. 5.4. We start with a commercial p-doped Si wafer with 100 nm AlN seed layer, 200 nm Molybdenum serving as a bottom electrode, and 1um thick AlN layer (shown in Fig. 5.4(a)) from OEM Group. A 300 nm Ni layer is first deposited and patterned with lift-off, serving both as a hard mask as well as the top electrode (Fig. 5.4(b)).

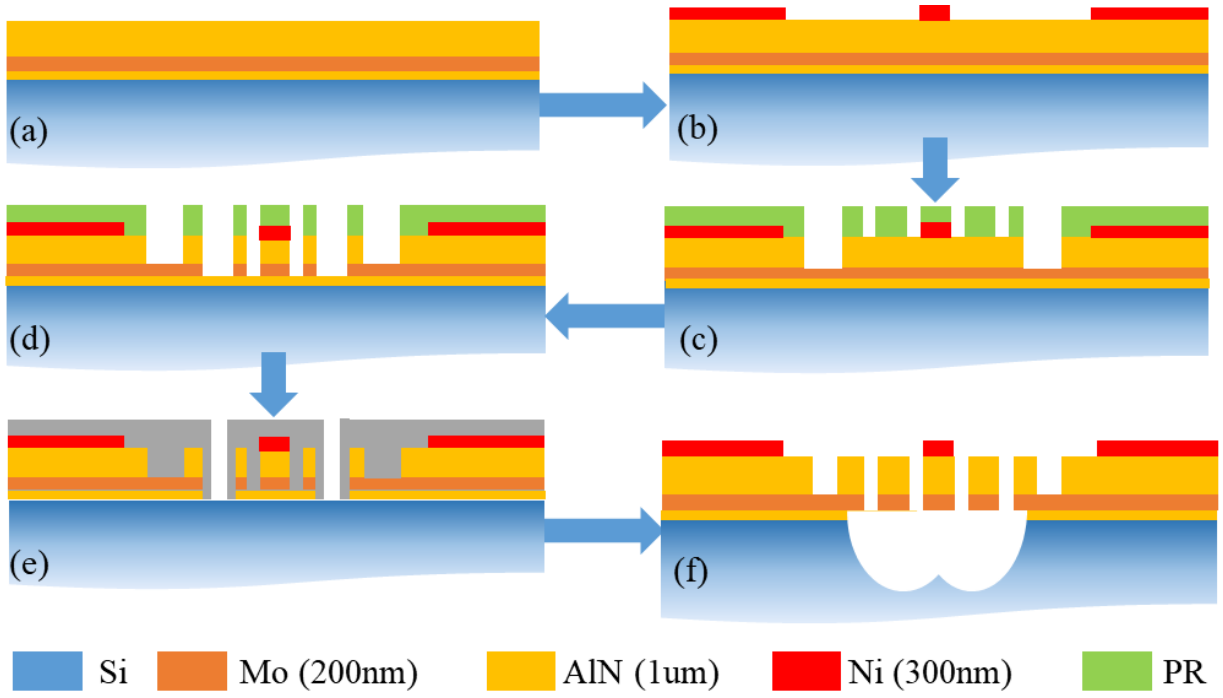

Figure 5.4 Cross-section of the fabrication process. (a) AlN (1 μm)/Mo (200 nm)/AlN (100nm) are deposited on p-type Si substrate (b) Lift-off of Ni as the top electrode and hard mask for the following steps (c) AlN etch to expose bottom electrode (d) AlN etch to define the AMs (e) Optical lithography to protect the edges of Mo and (f) XeF_2 isotropic etching to release the device.

Then, a BCl_3/Cl_2 ICP-RIE process is performed to etch through the AlN to access the Mo bottom electrode (Fig. 5.4(c)). After that, a second ICP-RIE is carried out to define the phononic crystal actuation/reflection matrix, where the etch extends through the bottom electrode and seed layer down to the Si substrate (Fig. 5.4(d)). Before the final release step, the Mo bottom electrode is protected against XeF_2 using an additional optical lithography step coating all sidewalls with resist (Fig. 5.4(e)) but exposing the bottom Si surface. Finally, a XeF_2 etch releases the AlN stack from the Si substrate, during which the Mo bottom electrode is protected by the thin AlN seed layer below and the photoresist on exposed edges (Fig. 5.4(f)). The protecting resist is ashed by a March Jupiter Etcher.

5.1.3 Experimental Results and Discussions

To experimentally validate the beam flexural mode, the AM matrix is implemented by a finite array of periodic units with the schematic design shown in Fig. 5.5.

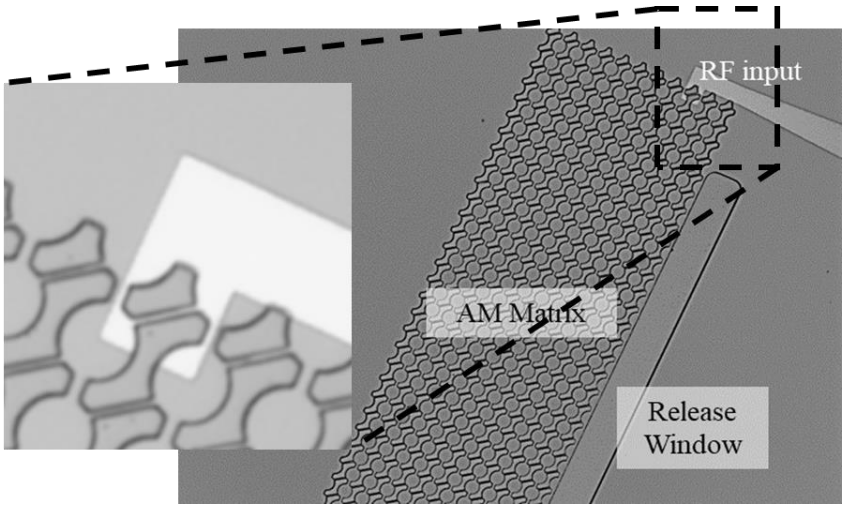

Figure 5.5 Optical image for the first type of resonant device with RF signals only applied on one of the unit cells

Fig. 5.5 demonstrates the optical image for the finite AM devices with 11×32 unit cells. In this case, the beam angle for all the units is kept as $\beta = 35°$. The top electrode is deposited on one unit of the matrix (in white) as RF input terminal. The RF signal is applied as sinusoidal waves with a peak-to-peak magnitude of 1V. The mechanical motion is then read out by the MSA – 600 Microsystem Analyzer at Polytec. Inc. in Irvine, CA. The measurement points are uniformly distributed across the entire unit cell.

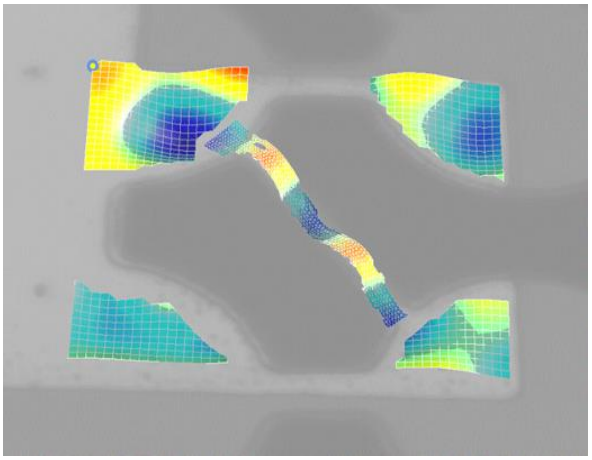

Figure 5.6 The out-of-plane velocity field for the corresponding mode shape measured from the LDV

Thanks to the state-of-the-art MSA-600 microsystem analyzer which can characterize the mechanical motion up to 2.5 GHz with up to 1 nm resolution, we can accurately capture the out-of-plane mechanical motion for the corresponding mode. The mechanical resonance is attained at 120 MHz which coincided with the targeted band frequency (132.4 MHz) predicted by Fig. 5.3(a).

As shown in Fig. 5.7, the obtained out-of-plane velocity field agrees very well with the 3D simulated out-of-plane motion (shown in Fig. 5.3(c)).

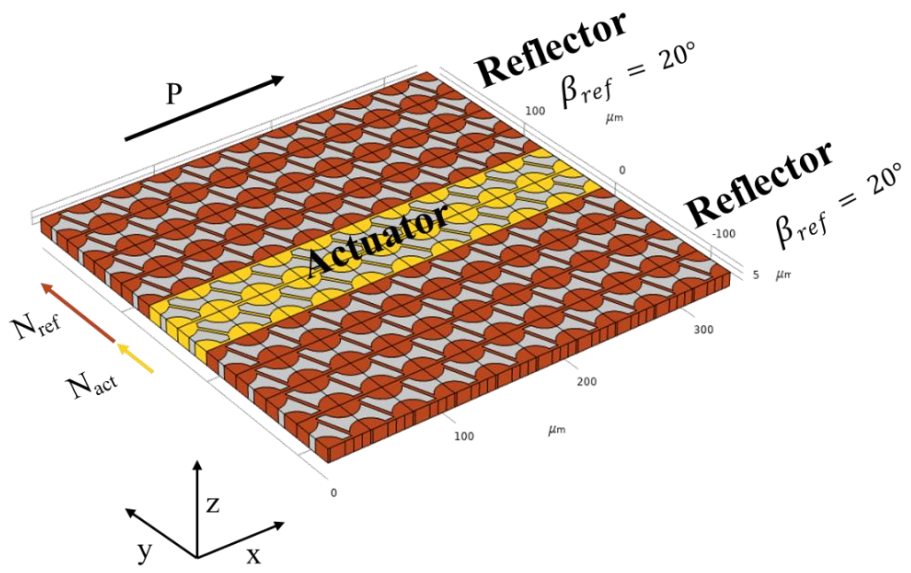

Figure 5.7 Schematic of resonator structure using asymmetric AMs. (a) Mechanical vibration is only induced at one unit cell. (b) The mechanical vibration is induced by the central actuation region (yellow) and is confined by the reflector regions (red) on either side along the y-direction.

Based on the previous LDV measurement and COMSOL simulation results, the near-flat characteristics of mode 1 indicate an almost-perfect confined standing wave, which can then be leveraged for an effective resonator.

Hence, an AM-based resonator is then designed and studied. As shown in Fig. 5.7, the designed resonator consists of an array of units in the center (actuation region) and at two sides (referred to as reflection region). The actuated region in the center (shown in yellow) generates mechanical vibrations while reflectors at the sides (shown in red) confine the energy in the y-direction toward the resonator center. The isolated beam resonance is configured within the bandgap of the reflection and actuation regions (shown in Fig. 5.2). To describe the varying geometry, the term "layer" is used here to indicate the number of repeated unit cells in the *y*-direction. The resonator's performance is then evaluated with varied diagonal central beam angle β, number of actuation layers N_{act} in the cavity in the direction of propagation (*y*-direction), number of cells *P* transverse to propagation, and number of AM reflector layers N_{ref} (shown in Fig. 5.7). To simplify the analysis, the diagonal beam rotation angle β_{ref} in the reflector is kept constant at $\beta_{ref} = 20°$ across all designs in this study.

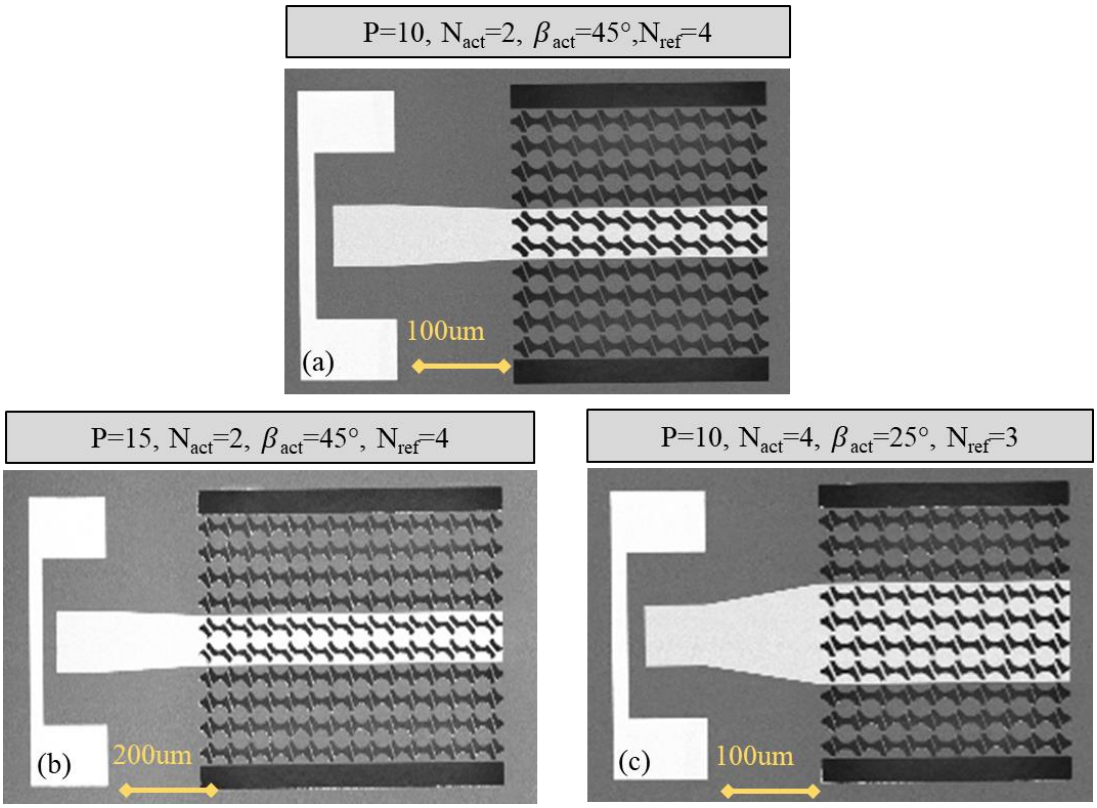

Figure 5.8 Scanning electron micrographs of AM resonators with varying central beam angle in the actuation layers β_{act}, number of actuation layers N_{act}, number of reflector layers N_{ref}, and number of cells along the transverse direction P.

Fig. 5.8 shows Scanning Electron Micrographs (SEMs) of three sample variations of the AlN AM resonators. As previously noted, the beam angle in reflector layers is kept as $\beta = 20°$ while actuator beams vary between 25° and 45°. The gray regions show the bare AlN while the black region indicates the etched area, with both AM matrix in the center and two rectangular release windows at the sides terminating the reflectors. The bright white region highlights the Ni top electrode, including one-port GSG pads. The Ground pads in the GSG extend down to contact the Mo bottom layer.

One-port RF measurements were performed under vacuum at room temperature using a PNA N5230A, with RF power of -10dBm and IF bandwidth of 300 Hz. Resonator parameters including electromechanical coupling coefficient k^2, motional resistance R_x and quality factor (Q) are extracted using a standard Butterworth-van-Dyke model [12] after de-embedding a pad capacitance of 2.34 pF and routing resistance of top and bottom electrodes (1 Ω and 5.6 Ω, respectively).

Fig. 5.9 shows a characteristic frequency response of Mode 1 in the AM resonators at 156 MHz. The reflection S_{11} is shown here on the left for two different actuation layer numbers (N_{act} of 2 and 4) with all other three parameters constant: lateral periods P of 10, actuation beam rotation angle is 45° and N_{ref}= 4. The measured frequency is 24 MHz lower than the COMSOL simulated results. This is due to the AlN sidewall slope which results in beam dimensions that are about 810 nm wider than designed. Fig. 5.9 represents the best performance for mode 1 in all designed structures.

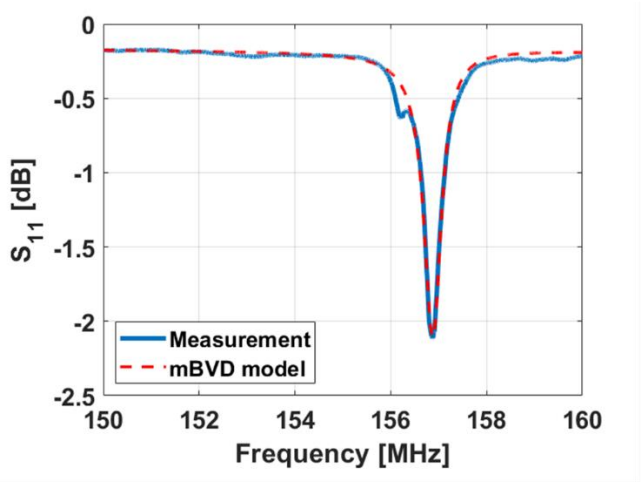

N_{act}	4
P	10
β_{act}	45
N_{ref}	3
f [MHz]	156.9
Q	360
$R_x[\Omega]$	125
k^2 [%]	1.05

Figure 5.9 AM resonator performance with varying N_{act}. An AM resonance is found at 156 MHz and Q increases with increasing N_{act}.

In this case, the corresponding resonance is found to be 156.9 MHz with the central beam rotation angle $\beta_{act} = 45°$. 3 reflection layers and 4 actuation layers are used in this design. The S_{11} is then fitted to the mBVD model to extract the equivalent circuit parameters. The extracted quality factor Q is about 360 and the electromechanical coupling coefficient is 1.05%.

Additionally, we report on Mode 2 resonance at 210 MHz at the higher band edge, shown in Fig.5.13 for β_{act} = 45°and varying P. Maximum Q of 1875 is obtained with R_x of 1.4 for P = 15.

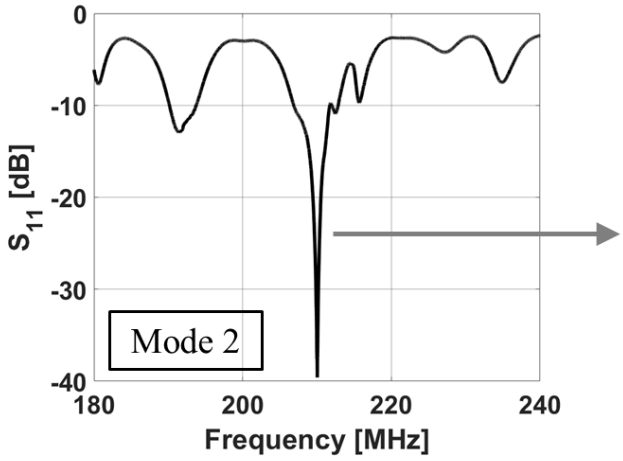

P	15
β_{act}	45°
N_{act}	4
f [MHz]	210
Q	1875
R_x [Ω]	1.4
k^2 [%]	1.13

Figure 5.10 Demonstration of the highest Q mode at 210 MHz. Maximum Q of 1875 can be obtained with R_x of 1.4 Ω for P = 15

Indeed, the quality factor presented by Mode 1 is limited. The main resources for the mode 1 loss could potentially come from mechanical wave scattering, electrical loading as well as insufficiency of resonant coupling among different units. Mechanical wave scattering losses mainly come from the non-ideality of the micro-fabrication process, including but not limited to, rough sidewall surface and non-straight sidewall angle. This can be further improved by re-optimization of the process flow, especially the BCl_3 and Cl_2 AlN etching process. Electrical loading losses refer to the losses from the electrical routing. This can be improved by increasing the number of actuation layers, reducing the overall motional impedance, and finally, increasing the Q. More importantly, as shown in Fig. 5.2, for mode 1, most of the energy is confined at the central flexural beam whereas, for mode 2, mechanical energy is more uniformly distributed across the whole lattice unit. The weak coupling between different lattice units leads to a reduced Q. This can be further proved by additional 2D finite element simulation

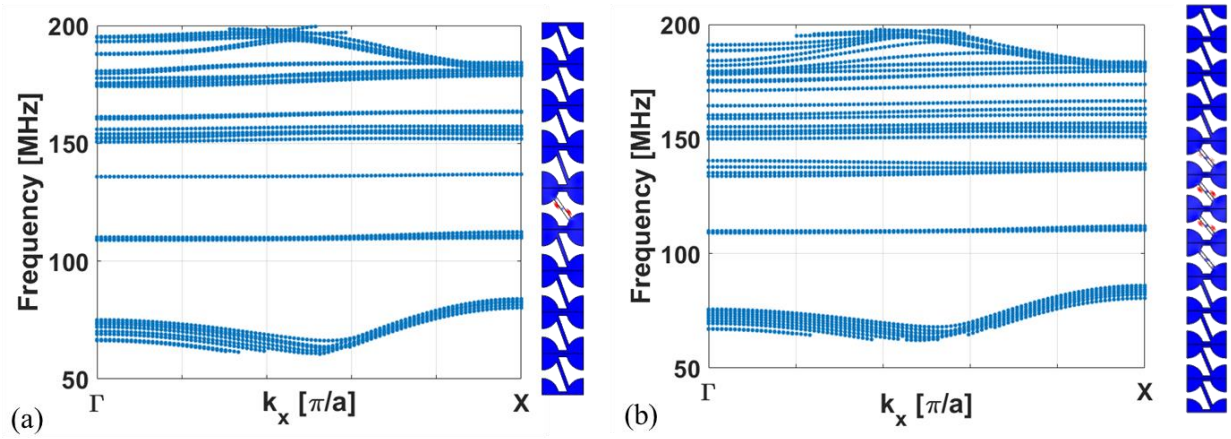

Figure 5.11 Dispersion relationship for the unit cell which includes four reflection layers and (a) one actuation layer and (b) four actuation layers.

As demonstrated by Fig. 5.11, the simulated unit consists of four reflector cells at the sides and varied number of actuation cells in the center. Same Floquet periodic boundary condition is applied at the left and right boundaries. The top and bottom is kept as free condition. As shown in Fig. 5.11 (a), only one band is observed at about 130 MHz. However, in Fig. 5.11(b), four bands are identified at about the same frequency corresponding to the four actuation layers at the center. Due to the weak coupling between each mode, the band frequency variation is tiny within about 3 MHz range. This supports the low-*Q* characteristics observed for Mode 1 from the RF measurements.

Piezoelectric coupling coefficient k^2 increases to 1.13%. Several spurious modes coexist with the target mode, though this can be improved with the optimized design of the reflector layers. This measurement demonstrates the presence of high *Q* modes alongside the low dispersive localized mode available in the same asymmetric AM. In future work, when engineered to line up in frequency, it is possible to use this platform to piece together both flat band transmission lines and high *Q* resonant elements to perform more complex signal processing in the mechanical domain.

5.2 Conclusions

In this chapter, a flat-band flexural beam mode in the bandgap of an asymmetric AM structure is designed and demonstrated as resonators with engineered parameters for both cavity and reflectors.

Resonators composed of these AMs were fabricated and characterized. Leveraging the laser doppler vibrometry technology, the shape of the flexural beam mode is captured and it coincided well with the finite element simulation results. Leveraging the flat-band characteristics of the flexural beam mode, resonators with varied central beam angles and dimensions are also studied. Both mode 1 and mode 2 are identified in simulation as well as the S parameter measurements. For mode 1, most of the elastic energy is localized within the central band whereas, for mode 2, the elastic energy is more uniformly distributed across the unit. This lack of resonance coupling between lattice units leads to the overall very limited *Q* for mode 1 compared to mode 2.

These measurements serve as an important first step toward near-zero velocity variation in a large-scale elastic medium at RF frequencies. This unique feature may have promising applications in acoustic cloaking, sub-wavelength imaging, and on-chip mechanical signal processing.

6. GUIDED NEGATIVE REFRACTION INDUCED BY ASYMMETRIC ELASTIC METAMATERIALS

Acoustic metamaterials are periodic composite materials or structures which have been explored extensively over the past few decades [124]. The spatial periodicity of metamaterials opens up new opportunities in the study of acoustic wave propagation, including transformation acoustics [96], [138] and topology acoustics [139], [140], resulting in unprecedented approaches of controlling and confining acoustic and elastic waves [141]–[145]. As already indicated in Chapter 4, the unique design of these metamaterials induces unusual physical phenomena including acoustic bandgaps [146] and negative [147], [148], which enable applications such as non-reciprocal wave propagation[149] and sub-wavelength super-lensing [150]–[152]. As demonstrated by Section 4.3, two mechanisms have been proved to generate the negative refraction effect, that is, the local resonance within the lattice unit and the multiple Bragg scattering between the lattice units. Pioneering work on local resonance acoustic metamaterial [103] has inspired a promising approach to achieve the NR property, that is, by integrating both negative density (ρ) and negative bulk modulus (B) to a single structure, forming a double negative index structure, or a left-handed structure [153]–[155], the Poynting vector is anti-parallel with the wavevector, leading to the NR effect. However, this condition does not have to hold. For the normal right-handed structures, the NR property could also be obtained under multiple Bragg scattering effects among different lattice units. However, previous demonstrations of these structures have not shown the NR properties induced as a combined effect of local resonance as well as multiple Bragg scattering. In this chapter, we designed and studied the asymmetric elastic metamaterial that is not only able to guide the elastic wave but is also capable of generating NR property as a result of these combined effects.

6.1.1 Unit Cell Design

The designed structure consists of a square array of unit cells (as shown in Fig. 6.1) where a membrane of AlN (yellow) is freely suspended in vacuum (grey). Four 90° circular sectors (radius R = 13.2 μm) at the corners are connected with three 2.64 μm wide beams - two lateral beams connecting adjacent columns and one bridging top left and bottom right sectors.

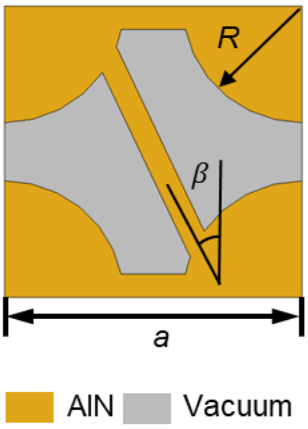

Figure 6.1 Unit cell of the proposed asymmetric elastic metamaterial investigated for guided negative refraction.

Same material stacks as reported in Chapter 5 are assumed here for all the numerical studies in this chapter. It should be noted that all the geometric parameters are chosen based on typical values seen in wafer-scale micro-fabrication using optical photolithography. However, the characteristics of the designed metamaterial can be generalized and scaled to any dimension. The central beam angle is denoted as β.

6.1.2 Dispersion Relationship and Negative Refraction

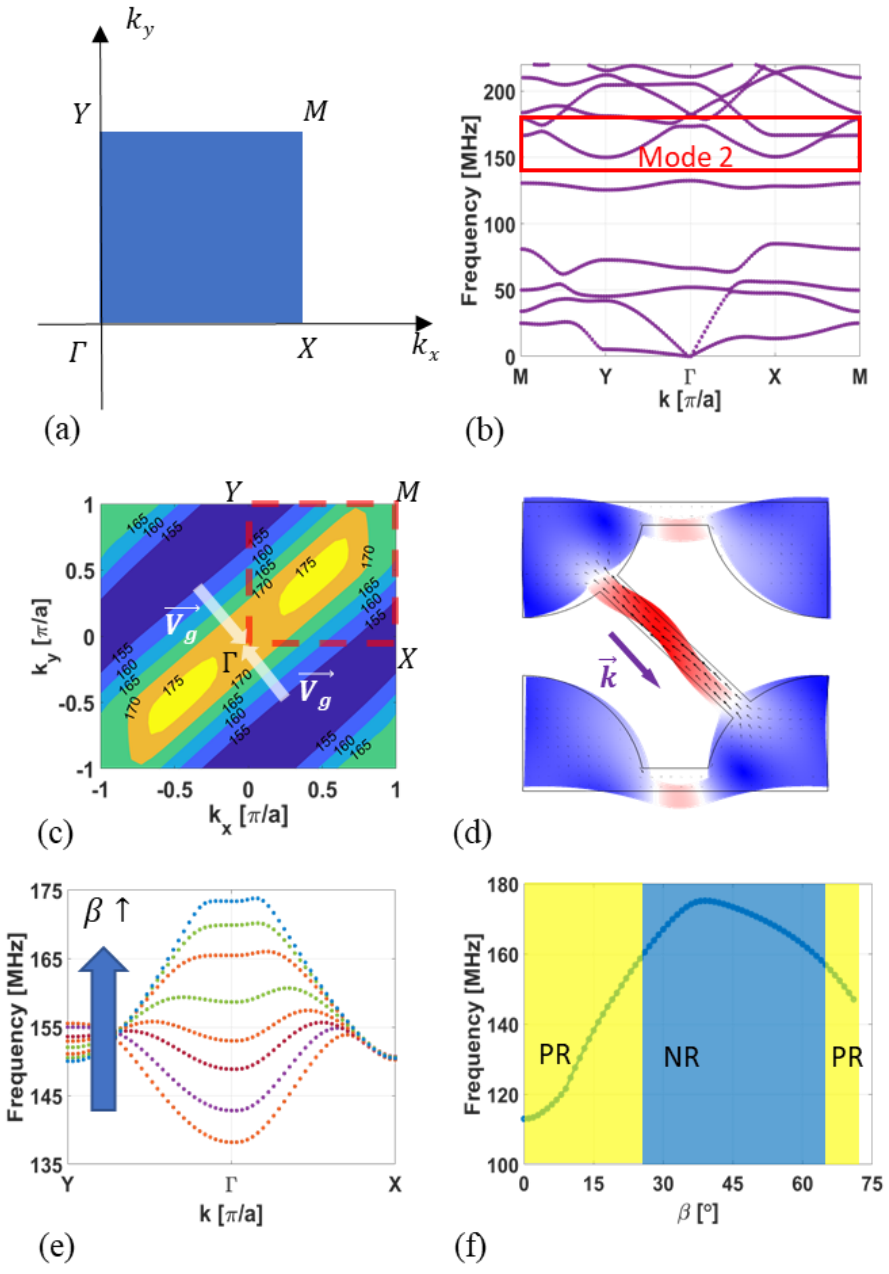

Figure 6.2 (a) Indication of the first Brillouin zone of a square lattice in 2D reciprocal space (b) Dispersion relationship for the designed structure with yellow rectangle indicating mode 2 (the sixth band). (c) The EFC for the sixth band with white arrows denoting the group velocity. The dotted red square indicates the first Brillouin zone. (d) Corresponding mode shape at 173 MHz. The black arrow indicates the energy flow direction whereas the purple arrow represents the phase velocity. (e) Variation of the sixth band with changing central beam rotation angle β. For simplicity, only band curvature with increased beam rotation angle is demonstrated here (f) Frequency of the sixth band at Γ point with β changing from 0° to 71°

For this periodic asymmetric structure, the first Brillouin zone is shown in Fig. 6.2(a). The dispersion relationship is calculated for the corresponding structure with $\beta = 35°$ (illustrated in Fig. 6.2(b)). In this case, the sixth band is concave, symmetric, and behaves as a plateau around the high-symmetry Γ point in reciprocal ($k-$) space. A corresponding equi-frequency contour (EFC) is plotted in Fig. 6.2(c). Due to the geometrical asymmetry of this design, the EFC is also anisotropic. The group velocity ($\overrightarrow{V_g}$) can be extracted as

$$\overrightarrow{V_g} = \nabla_{\vec{k}} \left(\omega(\vec{k}) \right) \tag{6-1}$$

As demonstrated by the EFC (Fig. 6.2(c)), the $\overrightarrow{V_g}$ should direct towards Γ point. The phase velocity is determined by the vector $\vec{k}$ and the energy flows (characterized by the Poynting vector $\vec{S}$) at the group velocity. Thus, in this case,

$$\vec{S} \cdot \vec{k} < 0 \tag{6-2}$$

which defines the sufficient condition for the NR property. The mode shape of the unit cell with periodic boundary conditions is found at 173 MHz in Fig. 6.2(d). The black arrow represents the energy flow direction. This mode shape is obtained adjacent to Γ point $\left(k_x = 0.1 \cdot \frac{\pi}{a}\right)$ to characterize the Poynting's vector and thus the direction of the traveling waves. The corresponding band curvature is defined by the central beam rotation angle, which can be verified by investigating the band shape variation in the dispersion relationship with β (Fig. 6.2(e)) changing from 0° to 71°. The maximum beam angle β is determined by the unit cell geometry wherein the central beam should not be isolated from the surrounding sectors. The dispersion relationship around the Γ point is derived across the range of central beam angles, showing a transition from convex to concave back to convex shape for the 6th band's dispersion (Fig. 6.2(e)). Fig. 6.2(f) summarizes this band's frequency at Γ. Below 25° and above 65°, the band is convex about the Γ point, that $\vec{S} \cdot \vec{k} > 0$, indicating positive refraction (PF). On the other hand, between 25° and 65°, the band is concave, implying negative refraction.

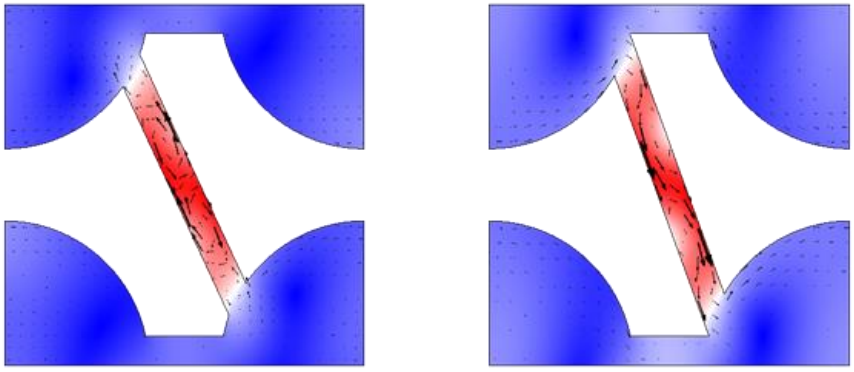

Figure 6.3 Resonance mode shapes of the 6th band with (a) $\beta = 25°$ and (b) $\beta = 20°$. The white arrows represent the Poynting vector.

Fig. 6.3 provides the resonant mode shapes for the same structure but three different central beam rotation cases. One in transition region when $\beta = 25°$ (Fig. 6.3 (a)) and the other in positive refraction region when $\beta = 20°$ (Fig. 6.3(b)).

When $\beta = 35°$, the Poynting vector is pointing towards to upper sectors - anti-parallel with the wavevector (shown in Fig. 6.2(d)). When $\beta = 25°$, both upward and downward Poynting vectors coexist, resulting in the cancellation of the overall energy flow (shown in Fig. 6.3(a)). Hence, we expect zero refraction to occur. When $\beta = 20°$, the Poynting vector is in parallel with the wavevector, corresponding to positive refraction (shown in Fig. 6.3(b)).

6.2 Implementation of guided negative refraction

6.2.1 Full-Wave Simulation with AM Matrix

To further illustrate the aforementioned findings, a finite 18 × 12 structure is simulated using finite element method (FEM) in COMSOL Multiphysics (Fig. 6.4). To avoid possible reflections, for this and the following full-wave simulation examples, all boundaries are set as low-reflecting boundary conditions (highlighted by dark blue boundary along the perimeter of the simulation structure). A uniform wave is incident on one of the unit cells on the left interface of the metamaterial. The elastic wave propagation within the metamaterial is governed by the gradient at the instantaneous EFC ($\overrightarrow{V_g}$ illustrated by Fig. 6.2(c)) [156], the wave is guided at 45°

towards the lower boundary (as shown in the von Mises stress field in Fig. 6.3). The saddle point in the EFC at the Γ point indicates that two group velocity vectors co-exist. As such, both forward and backward propagating waves should be obtained.

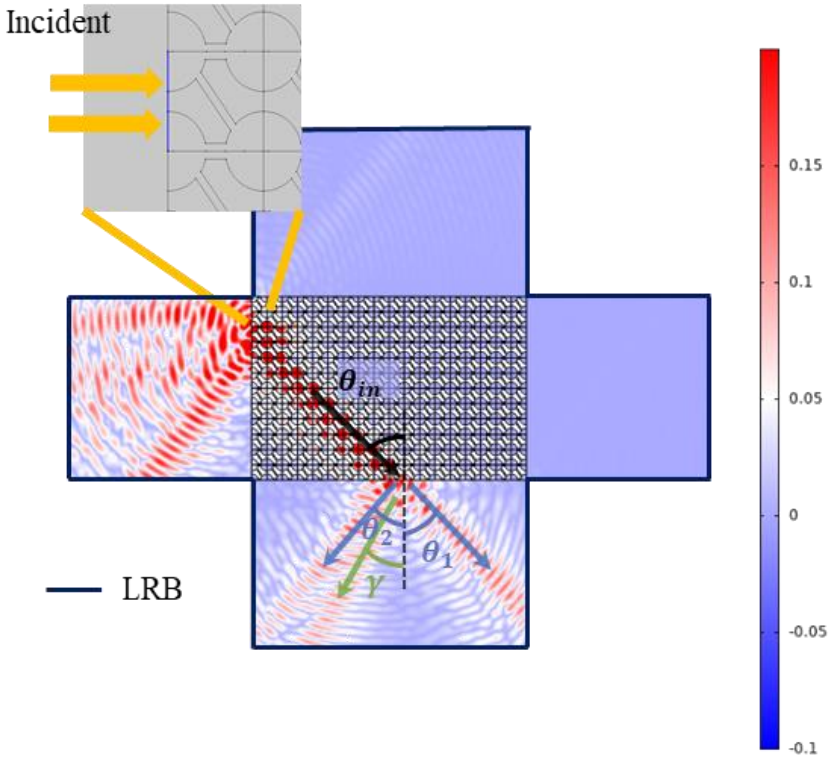

Figure 6.4 Demonstration of wave propagation across the elastic metamaterial with uniform wave incident on one of the unit cells. The wave was guided 45° inside the metamaterial towards the bottom boundary and then split into three branches.

At the metamaterial/AlN interface, the incident wave is split into three refracted branches with $\theta_{in} = \theta_1 = \theta_2 = 45°$ and γ = 30°. The orthogonal blue-arrow waves are generated as a result of the translational periodicity of the structure in reciprocal space [131] whereas the green-arrow wave results from the opposing direction between energy flow and wavefront (Eqn. (6-2)). Refraction angle $\gamma = 30°$ indicates the incident wave undergoes refraction at the interface and the corresponding refractive index of the metamaterial can be calculated as $n_{meta} = -1.52$.

6.2.2 Split Waves at Elastic Metamaterial/Bulk AlN Interface

It should be noted in Fig. 6.4, at the elastic metamaterial/bulk AlN interface at the bottom, the incident wave is split into three branches. The green arrowed wave is believed to be the result of the negative refraction. However, two additional blue waves coexist.

To study the root cause of the blue-arrowed wave, a different central beam rotation angle is first investigated.

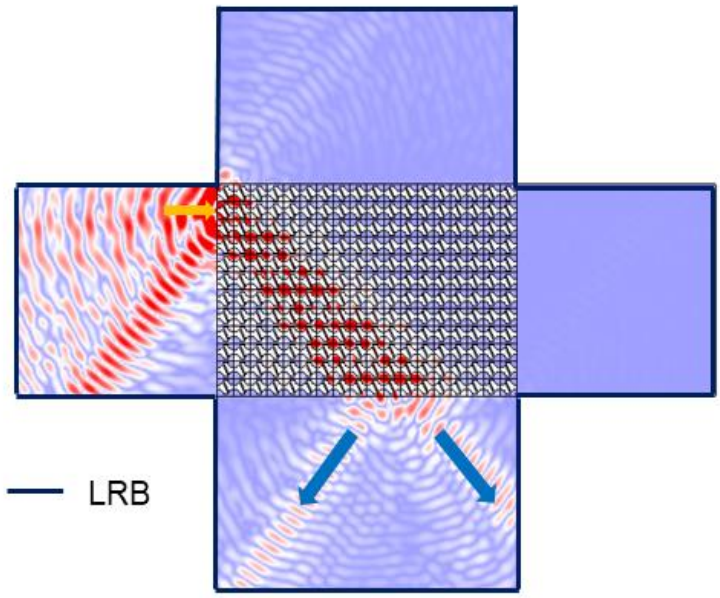

Figure 6.5 Schematic of the full-wave field at Γ point of the sixth band with central beam rotation angle $\beta = 25°$

As demonstrated by Fig. 6.5, a uniform was incident at the same location. Yet, this time, the green-arrowed wave disappeared. This reveals that the refracted wave is directly related to the central beam and is generated under the specific relationship between the energy flow and wave propagation direction (characterized by Eqn. (6-2)). The effect of the mechanical resonant mode shape under different β on the corresponding energy flow direction has been illustrated in Sec. 5.1.

The existence of the two radiated waves indicated by blue-arrows can be explained by the beam splitting theory.

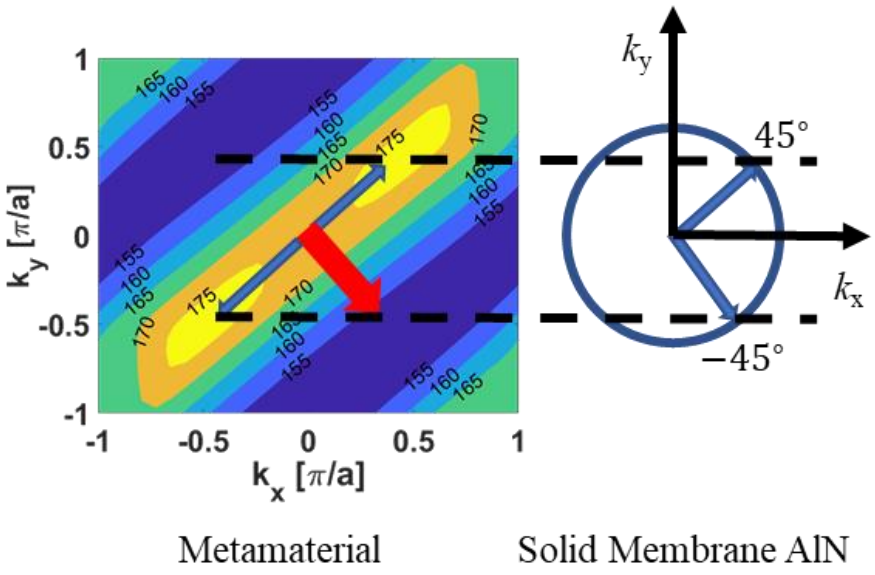

Figure 6.6 EFCs for both the elastic metamaterial and solid AlN membrane. Inside the metamaterial regime, the red arrow indicates the forward propagating energy flow as a result of the 6th band mechanical resonance. Leveraging the translational periodicity of the structure, two identical group velocity vectors coexists(± 45°)within the metamaterial regime. As such, two split waves are obtained at solid membrane AlN.

Fig. 6.6 has shown the EFCs for the elastic metamaterial as well as the solid AlN membrane. Due to the translational periodicity of the designed elastic metamaterial, the incident wavefront propagates both forward and backward within the metamaterial. Following analysis similar to [131], EFCs for both the metamaterial and the solid AlN membrane are plotted in Figure 8. When the entire structure is excited at resonance, according to the wave field shown by Figure 3, the elastic wave is "forced" to propagate 45° South-East (indicated by the red arrow). According to Snell's law, the tangential component of the wavevector must be conserved as a wave propagates from one medium to the other. A split wave is therefore obtained at the metamaterial/bulk AlN interface with each 45° to k_x .

Initial experimental results are also obtained from LDV measurements. The same acoustic metamaterial structure (optical image was shown in Fig. 5.5) was driven from a single unit cell (at X = 3, Y = 1) in the time domain at f = 131 MHz with the same peak-to-peak driving voltage. The corresponding mechanical motion of the same structure was measured again under the LDV.

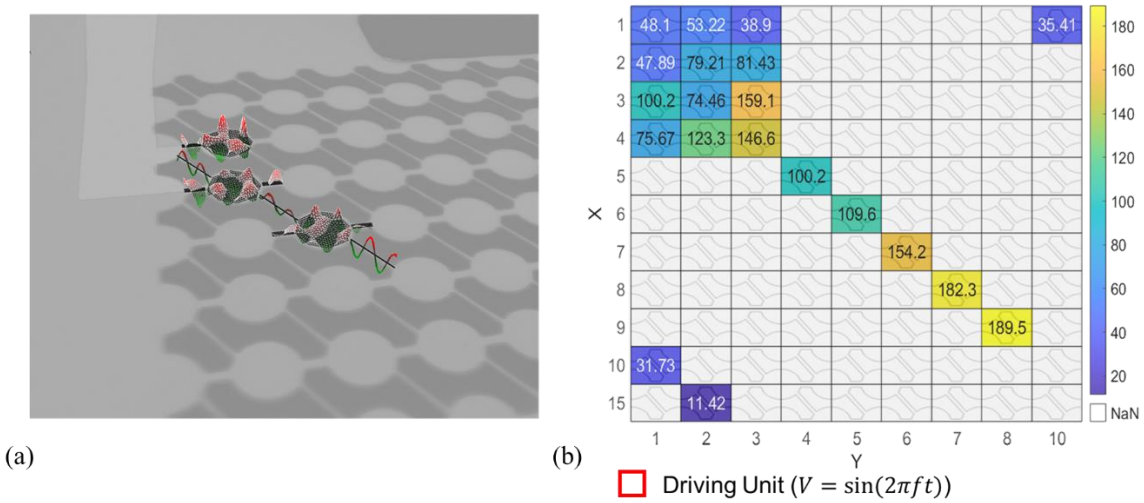

Figure 6.7 Initial absolute displacement amplitude measurement at Mode 2. The mechanical motion is driven at X = 3 and Y = 1. (a) corresponding mechanical motion for three units (b) The number in each unit represents the maximum absolute displacement magnitude (in pm) of each unit

However, in this case, characterizing the entire structure becomes very challenging. In order to measure the entire matrix with all the units at once, the structure needs to be focused on low magnification. But unfortunately, there is +10 MPa of internal stress built within the thin film AlN. Once the membrane is released from XeF_2, the whole structure deforms and becomes wavy at the surface with beams either bending ups or downs. Hence, in this case, they do not share any confocal points. As a result, the actual mechanical motion will be immersed within the noise.

Instead, the LDV focuses and characterizes one unit each time. Fig. 6.7(a) shows the corresponding mechanical motion for the given mode and Fig 6.7(b) demonstrates the energy flow direction with each number represents the maximum absolute displacement in the picometer. Units with color represent a high signal-to-noise ratio. In this case, mechanical energy is confined in the 45-degree NW-SE direction.

In order to fully capture the wave propagation through and after the acoustic metamaterial, the re-optimization of the dimension and geometry of the entire matrix becomes necessary. AlN fabrication process needs to be re-developed so that the AM can be scaled down to the nanometer range with fewer periods of unit cells in both X and Y directions. This will ensure the LDV captures the mechanical motion for the entire structure with minimum distortions from the thin film deformation.

6.2.3 Implementation of The Symmetric Wavefield

Inspired by the discoveries in Figure 6.4, we consider two implementations of this guided NR material for the manipulation of mechanical signals. The first structure, shown in Figure 6.8, consists of a finite 16 × 32 structure.

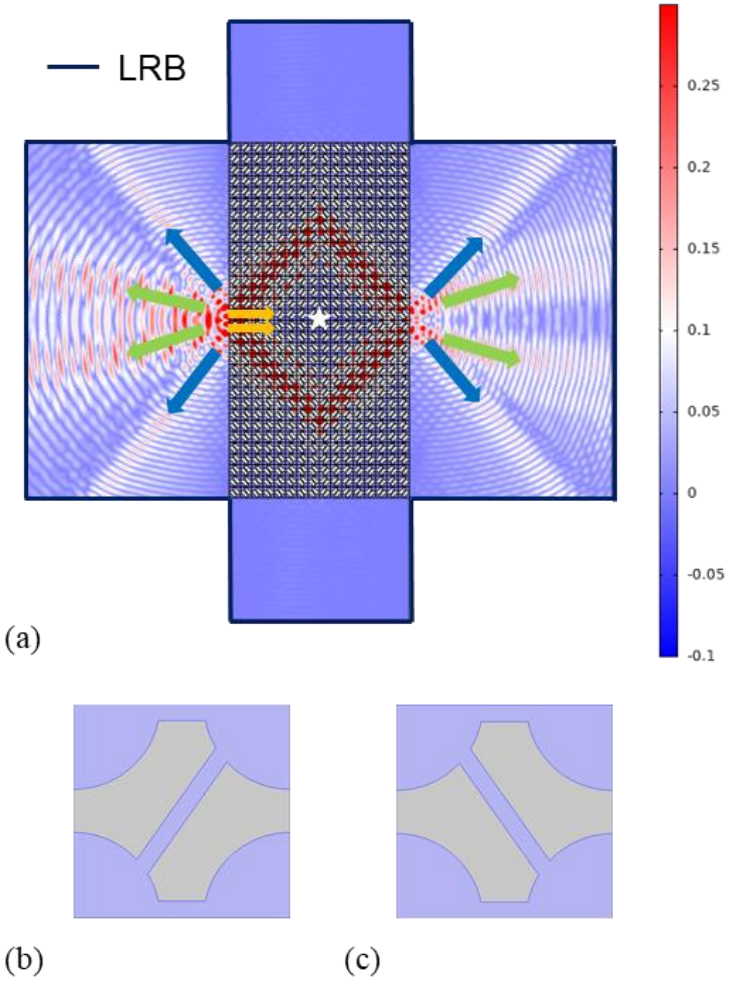

Figure 6.8 (a) Schematic of the full-wave field at 173 MHz with a whole structure consisting of four groups of unit cells, specifically, unit cells with central beam connecting (b) top right and bottom left sectors (c) top left and bottom right sectors.

This time, instead of complete translational invariance across the metamaterial, this new finite structure contains four different groups of cells with each group 8 × 16 units. Fig. 6.8 (b)-(c) illustrates the unit of each group at top left, bottom right (Fig.6.8(b)) and top-right, bottom-left

(Fig.6.8(c)), respectively. As demonstrated in Fig.6.8(a), all groups are centrosymmetric about the center (marked by a white star). A uniform wave is an incident on one of the units on the left boundary (yellow arrows). As illustrated by the von Mises stress field in Fig.6.8(a), at the resonance frequency, the elastic wave is guided along the central diagonal beamforming a 'diamond' wave propagation path within the metamaterial. Meanwhile, at the metamaterial/AlN interfaces at the left and right, the waves are split into four branches. Per our previous analysis, blue arrows represent the wave propagation induced by the translational periodicity of the structure whereas the central two green arrows represent the refracted wave induced by the opposite direction between the energy flow and the wave vector.

6.2.4 Implementation of The Fully Trapped Wavefield

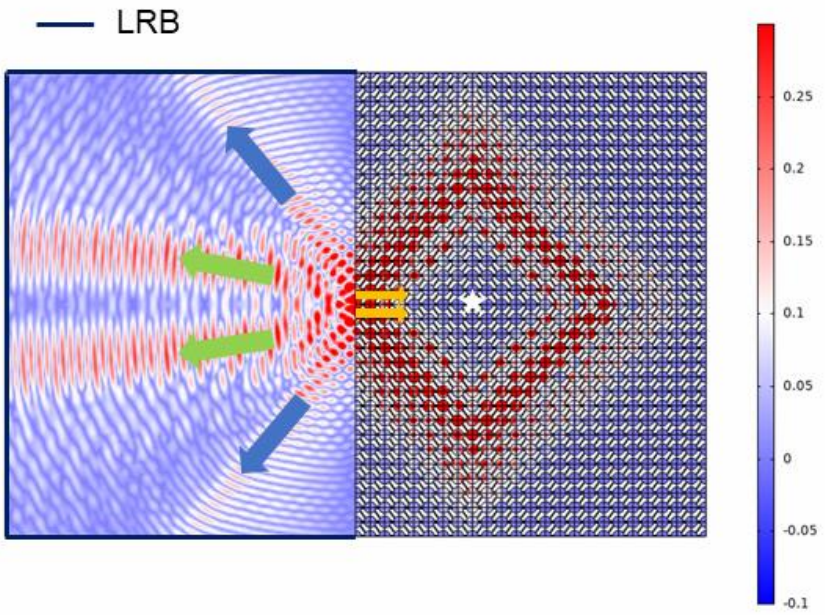

Figure 6.9 Schematic of the full-wave field at 173MHz with whole structure same as Fig.6.7(a) but the right half duplicated along the lateral direction.

Another example is illustrated by Fig. 6.9. This is a 24 × 32 finite structure consisting of the same groups as Fig.6.8 (b)-(c). All groups are centrosymmetric about the white star. However, this time, the right half of the structure is duplicated along the lateral direction, extending the metamaterial boundary towards the far-right. As a consequence of the specific mechanical

resonance, the elastic wave is unidirectionally guided along the central diagonal beam, forming a ’diamond’ shape inside the metamaterial. The guided mode exhibits the same four-wave split at the left interface with the AlN membrane. Otherwise, the elastic energy is fully confined within the metamaterial. All waves return to the original incident point with no transmission through the right boundary.

6.3 Conclusions

In summary, this chapter reports for the first time on guided negative refraction induced by an asymmetric elastic metamaterial. Leveraging a mechanical resonance band unique to this material, the elastic wave is guided inside the metamaterial. Due to the translational periodicity of the designed structure in reciprocal space, a wave incident from the metamaterial into a solid membrane is shown to split into three refracted waves at the metmaterial/bulk AlN interface under the combined effect of local resonance within the lattice unit and multiple Bragg scattering among different units. The demonstration of two implementations shows the ability to guide, trap, and split elastic waves with low dispersion.

These unique features could have the potential in applications including acoustic lenses, acoustic tweezers, and micro-particle splitters.

7. CONCLUSION

7.1 Summary of The Results

Leveraging the low wave speed and low loss in high-quality materials, mechanical waves have been widely used in the recent development of communication, actuation, and sensing systems. This thesis has reported new designs for both traditional and novel approaches to manipulating mechanical waves.

First, we put forward a new class of RF resonators which is seamlessly integrated within Texas Instruments' 350nm ferroelectric RAM process. The central PZT layer is sandwiched by the top and bottom Ir electrode, forming a metal-ferroelectric-metal (MFM) capacitor. Upon operation, all the FeCAPs are poled at the saturation poling condition, due to the piezoelectrical effect of the PZT, electric signals can be converted to mechanical signals and vice versa. Based on the corresponding dispersion relationship, most of the mechanical energy is designed to be confined within the PZT layer. Same structure but grounding FeCAPs are designed at two sides, pushing the boundaries far from the main resonant cavity, further boosting the energy confinement. A record-breaking $f \cdot Q$ of 7.11×10^{11} is obtained. A corresponding TCF of -58.1 ppm/℃ is attained.

Then, due to the hysteretic effect of the ferroelectric PZTs, the designed resonator is shown to be switched between pole, off, and zero states. A corresponding mBVD model is developed to understand the switching effect. With one port fixed at maximum poling condition while sweeping the other port, a "butterfly-shaped" transmission S_{21} can be obtained. This type of fully integrated switchable MEMS-CMOS resonator can provide platforms for switchable RF filtering, timing, actuating, and sensing applications.

Apart from new designs in traditional mechanical signal processing approaches, this thesis also reports approaches using acoustic metamaterials. An acoustic metamaterial-induced mechanical resonance is designed in the AlN platform. The flexural beam mode is first found in finite element analysis simulation and is then confirmed in experiments. Most of the elastic energy is confined within the central flexural beam, leading to an almost flat band in the dispersion relationship. This indicates near-zero group velocity and infinite phase velocity at Γ point. This unique feature may have promising applications in acoustic cloaking, sub-wavelength imaging.

Finally, with the same structure but for the band in the dispersion relationship at a higher frequency, geometrically, it is concave and almost flat in the vicinity of Γ point. An expanded dispersion relationship – the equi-frequency contour (EFC) is plotted and studied. It is analytically demonstrated that the wave is propagated under a combined effect of local resonance within the lattice units and multiple Bragg scattering among different lattice units. The anti-parallel direction of wave and energy propagation indicates negative refraction. Meanwhile, the maximum energy localized in *k*-space points other than Γ indicates the multiple Bragg scattering effect. As a result, two additional split waves are attained at the metamaterial-bulk interface. Two possible implementations are also demonstrated to guide or fully confined and reflect the incident mechanical waves. These features would have potential applications in fields including but not limited to acoustic lensing, acoustic tweezing as well as particle splitting.

7.2 Future Directions

7.2.1 Integrate FeCAP Resonators in RF Building Blocks

Except for the outstanding performance of the demonstrated resonator, the major advantage of the fully integrated resonator would include but not limited to the greatly reduced footprint, the significantly relaxed requirement for impedance matching with the surrounding circuitry as well as the dramatically reduced cost for large-array manufacturing. Therefore, a major future direction would be to integrate the designed resonant structure within a real system, including filters, oscillators, and sensors.

With high *Q* at the high resonant frequency, replacing the FeCAP based resonator with LC lumped resonator in traditional CMOS oscillating circuitry would be the most promising and would serve as a major extension of this thesis. With strong output signal amplitude, the FeCAP based oscillator would require less amplification gain to close the oscillation loop and are expected to have low power consumption and low phase noise.

7.2.2 New Ferroelectric Materials

Even though the ferroelectric capacitor-based fully integrated RF resonator reported in this thesis achieved high $f \cdot Q$, the corresponding k^2 is limited. This is directly related to the actuation

and sensing of PZT thin films. Specifically, the deposited PZT film is too thin and the material itself has been optimized for the pyroelectric hysteresis effect but not fully optimized for its piezoelectricity.

Alternatively, a heavily Sc doped AlN has also demonstrated ferroelectric effects. Not only could AlScN be fully integrated within the standard CMOS process but it also has a much higher k_{eff}^2, which would translate to higher bandwidth RF filters. In addition, materials like Si-doped HfO_2 and HZO have also been released as relatively new piezoelectric materials and have been reported to be compatible with the standard CMOS process[66], [157]. With fully established wave-guiding concepts and methodology, studying and implementing high *Q* AlScN based waveguided mechanical resonance would be a natural extension of this thesis.

APPENDIX A. FERROELECTRIC RESONATOR DESIGN PROCESS

Two-dimensional finite element analysis is performed by COMSOL Multiphysics® to investigate and optimize resonance modes in the FeRAM CMOS stack. As noted in the article, Floquet periodic boundary conditions are applied at the left and right boundaries, while perfectly matched layers (PMLs) are applied at the top and the bottom of the device to eliminate the elastic wave reflections from there. By searching the eigenmodes along the first Brillouin zone, we can obtain the dispersion relations of acoustic waves in the CMOS stack.

Limited by the technology, a maximum of 5 metal layers are used in the process. While lithographic dimensions can be changed within the constraints of the design rules, materials and thicknesses of the layers are predetermined by the technology. Practically speaking, the first metal layer must be reserved for electrical routing to the transducers, and must therefore be omitted from the BEOL reflector design. Based on these design constraints, we optimize the following parameters to maximize energy confinement in the resonance cavity:

- Number of metal layers used in the BEOL reflector
- Width of each metal layer in the x-direction
- Lattice constant a in the x-direction

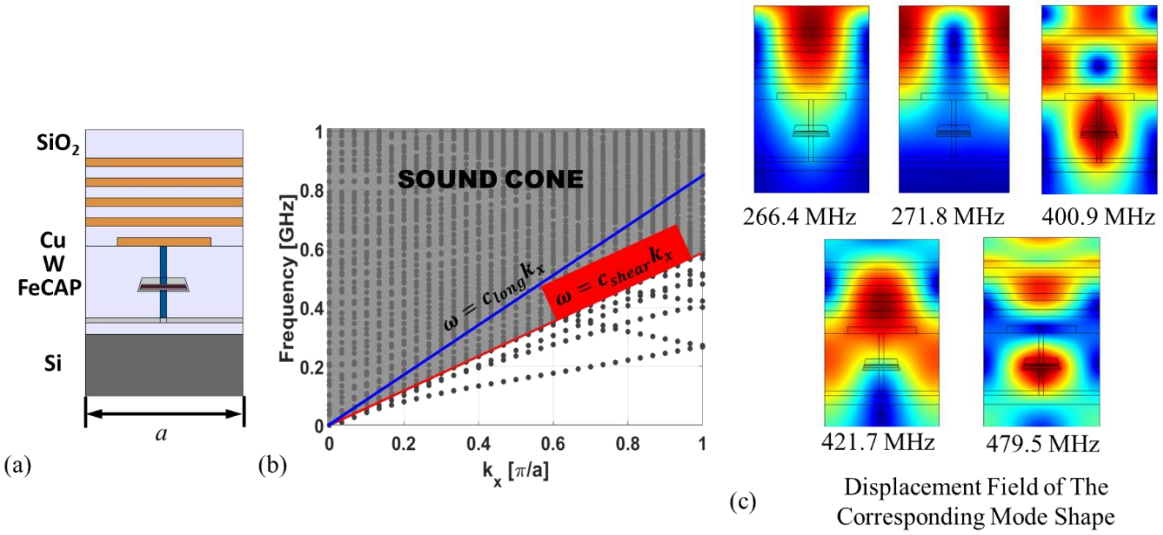

Figure A.1 (a) Schematic of FeCAP acoustic waveguide unit cell with 5 metal layers.(b) Dispersion relation for the device. (c) The mode shapes of localized modes found along $k_x = \pi/a$.

Mode optimization begins with a range of devices using 5 metal layers at the BEOL. Apart from the first metal layer, all the other layers are continuous across the FeCAP area (Figure S1(a)). It is assumed that the length of the trapezoidal FeCAP is 1.4 μm and the length of the lattice constant a is 5 μm. The dispersion relation, obtained through eigenmode analysis in COMSOL, is shown in Fig. S1(b). The blue and red lines present the longitudinal and shear sound lines, respectively. Several discrete modes exist below the shear sound line, indicating modes that are slow enough to be guided laterally in the CMOS stack. However, according to the stress distribution of these guided modes along $k_x = \pi/a$, only the modes at 400.9 MHz and 479.5MHz are coupled efficiently to the FeCAP transducer. These mode shapes also indicate the energy confined in the FeCAP is coupled with the metal layers above it, corresponding to acoustic loss. Additionally, the localized modes are very close to the shear sound line, indicating an opportunity for scattering into the bulk Si corresponding to a lower quality factor.

To push the strain energy downwards closer to the FeCAP, the number of metal layers is reduced to two. The schematic of the device is shown in Fig. S2(a), with corresponding dispersion relation in Fig. S2(b). Five localized modes are visible along $k_x = \pi/a$ below the shear sound line. Their displacement field is plotted in Fig. S2(c). In this case, only the mode at 433.4 MHz results in a large overlap between the strain energy and the transducer area. This is a necessary

characteristic for high-efficient electromechanical coupling for drive and sense. However, the energy is still coupled with part of the SiO_2 layers and it is not fully confined within the FeCAP area. To simplify the optimization process taking into account technology limits, the length of the FeCAP is fixed at 1.4 μm. Sweeping the geometry of the metal layers, it is found that a metal length of 600 nm provides the best confinement.

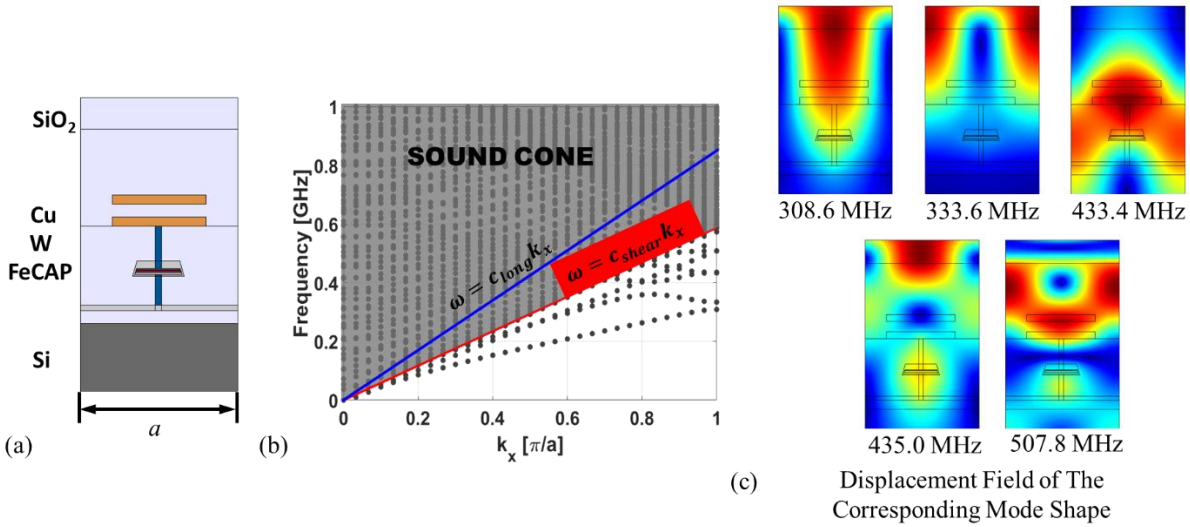

Figure A.2 (a) Schematic of FeCAP unit cell with two metal layers. (b) Dispersion relation for the device with two metal layers. (c) The mode shape of localized modes found along $k_x = \pi/a$.

To further enhance the energy confinement, the authors investigated the effect of decreasing the unit cell length a. This is because, the sound line is expressed as $\omega = c \cdot k$, where c is the acoustic wave velocity of a given material and k is the wavenumber. Normalizing k with $\frac{\pi}{a}$ and we obtain

$$f = \frac{\omega}{2\pi} = \frac{c}{2a}k\,.$$

Thus, the slope of the sound line is inversely proportional with a. By decreasing a, the resonance mode frequency is increased, and when a=2 um (lithographic limit of the technology), and the distance between the confined mode and the sound line reaches maximum. This provides a lower probability of mode scattering into the bulk Si and indicates the highest energy confinement.

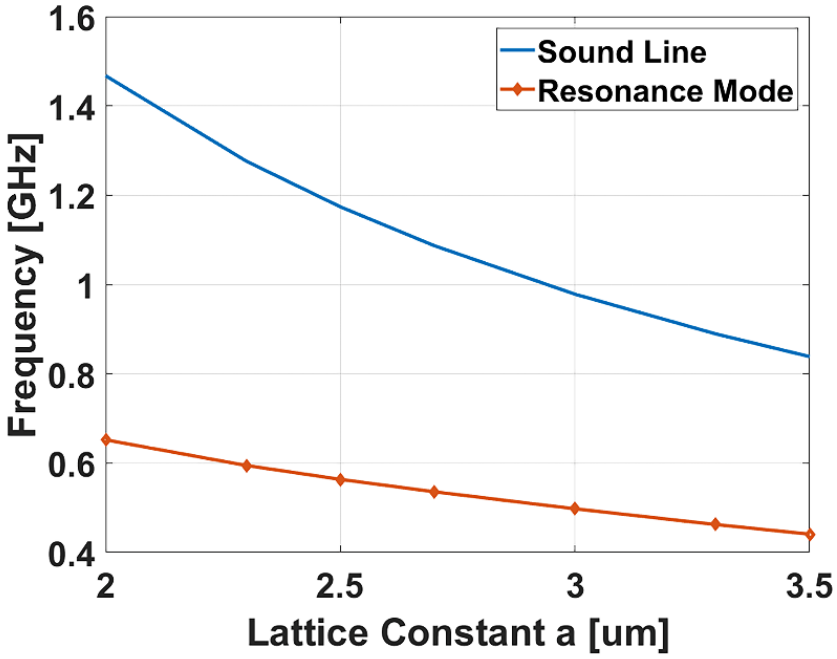

Figure A.3 Dependence of the acoustic mode frequency on the changing lattice constant *a*. As the lattice constant reduces, the distance between the localized mode and the sound line increases.

To conclude, the metal width of 600 nm for metals 1 and 2, with the lattice constant a = 2 um provides a combination of large acoustic confinement with the maximum overlap of elastic energy in the FeCAP transducer, within the lithography constraints of the TI E035 technology. The corresponding dispersion relation is shown in Fig. 2 of the manuscript.

REFERENCES

[1] J. Lianghai, B. Han, M. Liu, and H. D. Schotten, "Applying device-to-device communication to enhance IoT services," *arXiv*, no. June, pp. 85–91, 2017.

[2] L. Militano, G. Araniti, M. Condoluci, I. Farris, and A. Iera, "Device-to-Device Communications for 5G Internet of Things," *EAI Endorsed Trans. Internet Things*, vol. 1, no. 1, p. 150598, 2015.

[3] H. Campanella, Y. Qian, C. O. Romero, J. S. Wong, J. Giner, and R. Kumar, "Monolithic Multiband MEMS RF Front-End Module for 5G Mobile," *J. Microelectromechanical Syst.*, vol. 30, no. 1, pp. 72–80, 2020.

[4] R. Marathe, W. Wang, Z. Mahmood, L. Daniel, and D. Weinstein, "Resonant body transistors in standard CMOS technology," *IEEE Int. Ultrason. Symp. IUS*, no. 617, pp. 289–294, 2012.

[5] S. Trolier-Mckinstry and P. Muralt, "Thin film piezoelectrics for MEMS," *J. Electroceramics*, vol. 12, no. 1–2, pp. 7–17, 2004.

[6] G. Pillai, A. A. Zope, J. M. L. Tsai, and S. S. Li, "An apodized 3-GHz thin film piezoelectric on substrate FBAR," *2017 Jt. Conf. Eur. Freq. Time Forum IEEE Int. Freq. Control Symp. EFTF/IFC 2017 - Proc.*, no. 2, pp. 551–553, 2017.

[7] M. F. Su, R. H. Olsson, Z. C. Leseman, and I. El-Kady, "Realization of a phononic crystal operating at gigahertz frequencies," *Appl. Phys. Lett.*, vol. 96, no. 5, pp. 2008–2011, 2010.

[8] W. Gautier, V. Ziegler, A. Stehle, B. Schoenlinner, U. Prechtel, and W. Menzel, "Ku-band 3D LTCC filter and BST-Varactor based temperature compensated resonator," *Ger. Microw. Conf. GeMIC 2009*, vol. 49, no. 0, pp. 15–18, 2009.

[9] Z. Schaffer and A. D. Considerations, "Investigation of Damping and Ladder Filter Synthesis for 3 GHz 20 % Scandium-Doped Aluminum Nitride Cross-Sectional Lamé Mode Resonators," *Ius 2020*, pp. 3–6, 2020.

[10] G. R. Kline, "Thin Film Bulk Acoustic Wave Filters for GPS," pp. 471–476, 1992.

[11] H. P. Löbl *et al.*, "Piezoelectric materials for BAW resonators and filters," *Proc. IEEE Ultrason. Symp.*, vol. 1, pp. 807–810, 2001.

[12] M. M. Torunbalci, T. J. Odelberg, S. Sridaran, R. C. Ruby, and S. A. Bhave, "An FBAR Circulator," *IEEE Microw. Wirel. Components Lett.*, vol. 28, no. 5, pp. 395–397, 2018.

[13] R. Fleury, D. L. Sounas, C. F. Sieck, M. R. Haberman, and A. Alù, "Sound Isolation and Giant Linear Nonreciprocity in a Compact Acoustic Circulator," *Science (80-.).*, vol. 343, no. January, pp. 516–519, 2014.

[14] T. Manzaneque, R. Lu, Y. Yang, and S. Gong, "An SH0 lithium niobate correlator for orthogonal frequency coded spread spectrum communications," *2017 Jt. Conf. Eur. Freq. Time Forum IEEE Int. Freq. Control Symp. EFTF/IFC 2017 - Proc.*, pp. 143–147, 2017.

[15] G. Wu, J. Xu, E. J. Ng, and W. Chen, "MEMS Resonators for Frequency Reference and Timing Applications," *J. Microelectromechanical Syst.*, vol. 29, no. 5, pp. 1137–1166, 2020.

[16] C. T. C. Nguyen, "MEMS technology for timing and frequency control," *IEEE Transactions on Ultrasonics, Ferroelectrics, and Frequency Control*, vol. 54, no. 2. Institute of Electrical and Electronics Engineers Inc., pp. 251–270, 01-Feb-2007.

[17] C. Zuo, J. Van Der Spiegel, and G. Piazza, "1.05-GHz CMOS oscillator based on lateral-field-excited piezoelectric AlN contour- mode MEMS resonators," *IEEE Trans. Ultrason. Ferroelectr. Freq. Control*, vol. 57, no. 1, pp. 82–87, 2010.

[18] B. W. Bahr, L. C. Popa, and D. Weinstein, "1GHz GaN-MMIC monolithically integrated MEMS-based oscillators," *Dig. Tech. Pap. - IEEE Int. Solid-State Circuits Conf.*, vol. 58, pp. 304–305, 2015.

[19] T. Manzaneque, R. Lu, Y. Yang, and S. Gong, "Lithium niobate MEMS chirp compressors for near Zero power wake-up radios," *J. Microelectromechanical Syst.*, vol. 26, no. 6, pp. 1204–1215, 2017.

[20] R. Lu, Y. Yang, M. H. Li, T. Manzaneque, and S. Gong, "GHz Broadband SH0 Mode Lithium Niobate Acoustic Delay Lines," *IEEE Trans. Ultrason. Ferroelectr. Freq. Control*, vol. 67, no. 2, pp. 402–412, 2020.

[21] T. Manzaneque, R. Lu, Y. Yang, and S. Gong, "Low-loss and wideband acoustic delay lines," *IEEE Trans. Microw. Theory Tech.*, vol. 67, no. 4, pp. 1379–1391, 2019.

[22] R. Lu, T. Manzaneque, Y. Yang, M. H. Li, and S. Gong, "Gigahertz low-loss and wideband S0 mode lithium niobate acoustic delay lines," *IEEE Trans. Ultrason. Ferroelectr. Freq. Control*, vol. 66, no. 8, pp. 1373–1386, 2019.

[23] S. Gong, Y. H. Song, T. Manzaneque, R. Lu, Y. Yang, and A. Kourani, "Lithium niobate MEMS devices and subsystems for radio frequency signal processing," *Midwest Symp. Circuits Syst.*, vol. 2017-Augus, pp. 45–48, 2017.

[24] Y. Q. Fu *et al.*, "Advances in piezoelectric thin films for acoustic biosensors, acoustofluidics and lab-on-chip applications," *Prog. Mater. Sci.*, vol. 89, pp. 31–91, 2017.

[25] R. . White and F. . Voltmer, "Direct Piezoelectric Coupling To Surface Elastic Waves," *Appl. Phys. Lett.*, vol. 314, no. November, pp. 10–13, 2004.

[26] W. Wang, "Solid State MEMS Resonators in Silicon," Massachusetts Institute of Technology, 2014.

[27] A. K. Namdeo and H. B. Nemade, "Simulation on effects of electrical loading due to interdigital transducers in surface acoustic wave resonator," *Procedia Eng.*, vol. 64, pp. 322–330, 2013.

[28] C. C. W. Ruppel, "Acoustic Wave Filter Technology-A Review," *IEEE Trans. Ultrason. Ferroelectr. Freq. Control*, vol. 64, no. 9, pp. 1390–1400, 2017.

[29] T. Matsuda, H. Uchishiba, O. Ikata, T. Nishihara, and Y. Satoh, "L and S band low-loss filters using SAW resonators," *Proc. IEEE Ultrason. Symp.*, vol. 1, pp. 163–167, 1994.

[30] M. H. Hamzah, J. Karim, A. A. M. Ralib, and A. N. Nordin, "Design and analysis of a boosted pierce oscillator using MEMS SAW resonators," *Microsyst. Technol.*, vol. 24, no. 1, pp. 587–594, 2018.

[31] M. A. Y. Ixx and P. S. S. A. W. Oscillators, "Precision Surface-Acoustic-Wave (SAW) Oscillators," *IEEE Trans. Ultrason. Ferroelectr. Freq. Control*, vol. 35, no. 3, pp. 342–364, 1988.

[32] H. S. Hong, D. T. Phan, and G. S. Chung, "High-sensitivity humidity sensors with ZnO nanorods based two-port surface acoustic wave delay line," *Sensors Actuators, B Chem.*, vol. 171–172, no. 1, pp. 1283–1287, 2012.

[33] J. Tsutsumi, T. Matsuda, O. Ikata, and Y. Satoh, "A novel reflector-filter using a SAW waveguide directional coupler," *IEEE Trans. Ultrason. Ferroelectr. Freq. Control*, vol. 47, no. 5, pp. 1228–1234, 2000.

[34] L. C. Popa, "Gallium Nitrid MEMS Resonators," 2014.

[35] S. Mahon and R. Aigner, "Bulk acoustic wave devices - Why, how, and where they are going," *2007 Int. Conf. Compd. Semicond. Manuf. Technol. CS MANTECH 2007*, pp. 15–18, 2007.

[36] G. Pillai and S.-S. Li, "Piezoelectric MEMS Resonators: A Review," *IEEE Sens. J.*, vol. XX, no. XX, pp. 1–1, 2020.

[37] A. Meredov, K. Klionovski, and A. Shamim, “77 GHz Screen Printed , Flexible , Beam-Switching Antenna Array for Wearable Radar Applications,” pp. 867–868, 2019.

[38] J. C. Kuo, J. T. Hoople, M. Abdelmejeed, M. Abdel-Moneum, and A. Lal, “64-Pixel solid state CMOS compatible ultrasonic fingerprint reader,” in *Proceedings of the IEEE International Conference on Micro Electro Mechanical Systems (MEMS)*, 2017, pp. 9–12.

[39] M. U. Memon, H. Jeong, and S. Lim, “Metamaterial-Inspired Radio Frequency Based Touchpad Sensor System,” *IEEE Trans. Instrum. Meas.*, vol. PP, no. c, pp. 1–1, 2019.

[40] J. K. Park *et al.*, “Noncontact RF Vital Sign Sensor for Continuous Monitoring of Driver Status,” *IEEE Trans. Biomed. Circuits Syst.*, vol. 13, no. 3, pp. 493–502, 2019.

[41] H. Bhugra and G. Piazza, *Piezoelectric MEMS Resonators*. 2017.

[42] V. Shih *et al.*, “Highly Reliable Piezoelectric Process Technology in Volume Foundry for Emerging Mems Applications,” *2019 20th Int. Conf. Solid-State Sensors, Actuators Microsystems Eurosensors XXXIII, TRANSDUCERS 2019 EUROSENSORS XXXIII*, no. June, pp. 190–193, 2019.

[43] C. Y. Chen, M. H. Li, C. S. Li, and S. S. Li, “Design and characterization of mechanically coupled CMOS-MEMS filters for channel-select applications,” in *Sensors and Actuators, A: Physical*, 2014, vol. 216, pp. 394–404.

[44] M. H. Li, W. C. Chen, and S. S. Li, “Mechanically coupled CMOS-MEMS free-free beam resonator arrays with enhanced power handling capability,” *IEEE Trans. Ultrason. Ferroelectr. Freq. Control*, vol. 59, no. 3, pp. 346–357, 2012.

[45] M. G. Guney, X. Li, V. P. J. Chung, J. Paramesh, T. Mukherjee, and G. K. Fedder, “High dynamic range CMOS-MEMS capacitive accelerometer array,” *Proc. IEEE Int. Conf. Micro Electro Mech. Syst.*, vol. 2018-Janua, no. January, pp. 992–995, 2018.

[46] B. Bahr and D. Weinstein, “Vertical Acoustic Confinement for High-Q FULLY-DIFFERENTIAL CMOS-RBTS,” in *Solid-State Sensors, Actuators, and Microsystems Workshop*, 2016, pp. 88–91.

[47] B. Bahr, Y. He, Z. Krivokapic, S. Banna, and D. Weinstein, “32GHz resonant-fin transistors in 14nm FinFET technology,” in *Digest of Technical Papers - IEEE International Solid-State Circuits Conference*, 2018, vol. 61, pp. 348–350.

[48] Bahr Bichoy, “Monolithically Integrated MEMS Resonators and Oscillators in Standard IC Technology Bichoy Waguih Azmy Bahr,” 2016.

[49] J. Curie and P. Curie, “Development by Pressure of Polar Electricity in Hemihedral Crystals with Inclined Faces,” *Bull. la Société minéralogique Fr.*, vol. 3, no. 4, pp. 90–93, 1880.

[50] G. Piazza, P. J. Stephanou, and A. P. Pisano, “AlN contour-mode vibrating RF MEMS for next generation wireless communications,” *ESSCIRC 2006 - Proc. 32nd Eur. Solid-State Circuits Conf.*, pp. 62–65, 2006.

[51] S. Gong, N. Kuo, and G. Piazza, “GHz AlN Lateral Overmoded Bulk Acoustic Wave,” pp. 2–6.

[52] Y. Hou, M. Zhang, G. Han, C. Si, Y. Zhao, and J. Ning, “A review: Aluminum nitride MEMS contour-mode resonator,” *J. Semicond.*, vol. 37, no. 10, 2016.

[53] L. C. Popa and D. Weinstein, “L-band Lamb mode resonators in Gallium Nitride MMIC technology,” in *IFCS 2014 - 2014 IEEE International Frequency Control Symposium, Proceedings*, 2014.

[54] V. J. Gokhale and M. Rais-Zadeh, “Uncooled infrared detectors using gallium nitride on silicon micromechanical resonators,” *J. Microelectromechanical Syst.*, vol. 23, no. 4, pp. 803–810, 2014.

[55] C. Y. Huang, J. H. Sun, and T. T. Wu, “A two-port ZnO/silicon Lamb wave resonator using phononic crystals,” *Appl. Phys. Lett.*, vol. 97, no. 3, pp. 2008–2011, 2010.

[56] N. M. Shorrocks, “The Influence of ZnO and Electrode Thickness on the Performance of,” pp. 911–914, 1999.

[57] S. Gong and G. Piazza, “Design and analysis of lithium-niobate-based high electromechanical coupling RF-MEMS resonators for wideband filtering,” *IEEE Trans. Microw. Theory Tech.*, vol. 61, no. 1, pp. 403–414, 2013.

[58] J. Valasek, “Piezo-electric and allied phenomena in Rochelle salt,” *Phys. Rev.*, vol. 17, no. 4, pp. 475–481, 1921.

[59] N. Setter, “What is a ferroelectric–a materials designer perspective,” *Ferroelectrics*, vol. 500, no. 1, pp. 164–182, 2016.

[60] I. A. Parinov, “Piezoelectric materials and devices,” *Piezoelectric Mater. Devices*, pp. 1–328, 2011.

[61] Y. Liao, *Practical electron microscopy and database*. An Online Book, 2006.

[62] K. H. Sano, R. Karasawa, and T. Yanagitani, "High electromechanical coefficient kt2=19% thick ScAlN piezoelectric films for ultrasonic transducer in low frequency of 80 MHz," *IEEE Int. Ultrason. Symp. IUS*, pp. 7–10, 2017.

[63] J. Wang *et al.*, "A Film Bulk Acoustic Resonator Based on Ferroelectric Aluminum Scandium Nitride Films," *J. Microelectromechanical Syst.*, vol. 29, no. 5, pp. 741–747, 2020.

[64] S. Fichtner, N. Wolff, F. Lofink, L. Kienle, and B. Wagner, "AlScN: A III-V semiconductor based ferroelectric," *J. Appl. Phys.*, vol. 125, no. 11, 2019.

[65] T. S. Böscke, J. Müller, D. Bräuhaus, U. Schröder, and U. Böttger, "Ferroelectricity in hafnium oxide thin films," *Appl. Phys. Lett.*, vol. 99, no. 10, pp. 0–3, 2011.

[66] S. J. Kim, J. Mohan, S. R. Summerfelt, and J. Kim, "Ferroelectric Hf0.5Zr0.5O2 Thin Films: A Review of Recent Advances," *ACS Appl. Electron. Mater.*, vol. 71, no. 1, pp. 246–255, 2019.

[67] J. Müller, P. Polakowski, S. Mueller, and T. Mikolajick, "Ferroelectric Hafnium Oxide Based Materials and Devices: Assessment of Current Status and Future Prospects," *ECS J. Solid State Sci. Technol.*, vol. 4, no. 5, pp. N30–N35, 2015.

[68] M. Ramezani, M. Ghatge, and R. Tabrizian, "High kt2.Q silicon Fin Bulk Acoustic Resonators (FinBAR) for chip-scale multi-band spectrum analysis," *Proc. IEEE Int. Conf. Micro Electro Mech. Syst.*, vol. 2018-Janua, no. January, pp. 158–161, 2018.

[69] M. Ghatge, G. Walters, T. Nishida, and R. Tabrizian, "A High-Q 30nm-Thick MFM Resonator Using Ferroelectric Hafnium Zirconium Oxide," *Proc. IEEE Int. Conf. Micro Electro Mech. Syst.*, vol. 2020-Janua, pp. 953–956, 2020.

[70] M. Ghatge, G. Walters, T. Nishida, and R. Tabrizian, "A Nano-Mechanical Resonator with 10nm Hafnium-Zirconium Oxide Ferroelectric Transducer," *Tech. Dig. - Int. Electron Devices Meet. IEDM*, vol. 2018-Decem, pp. 4.6.1-4.6.4, 2019.

[71] H. Jaffe and D. A. Berlincourt, "Piezoelectric Transducer Materials," *Proc. IEEE*, vol. 53, no. 10, pp. 1372–1386, 1965.

[72] Y. Qiu *et al.*, "Piezoelectric micromachined ultrasound transducer (PMUT) arrays for integrated sensing, actuation and imaging," *Sensors (Switzerland)*, vol. 15, no. 4, pp. 8020–8041, 2015.

[73] E. E. Aktakka, R. L. Peterson, and K. Najafi, “High stroke and high deflection bulk-PZT diaphragm and cantilever micro actuators and effect of pre-stress on device performance,” *J. Microelectromechanical Syst.*, vol. 23, no. 2, pp. 438–451, 2014.

[74] C. Zinck, D. Emmanuel, A. Volatier, G. Caruyer, D. P. Tanon, and L. Figuiere, “Design, integration and characterization of PZT tunable FBAR,” *IEEE Int. Symp. Appl. Ferroelectr.*, vol. 00, no. c, pp. 29–32, 2005.

[75] J. D. Larson, S. R. Gilbert, and B. Xu, “PZT Material properties at UHF and microwave frequencies derived from FBAR measurements,” *Proc. - IEEE Ultrason. Symp.*, vol. 1, no. c, pp. 173–177, 2004.

[76] G. L. Smith *et al.*, “PZT-based piezoelectric MEMS technology,” *J. Am. Ceram. Soc.*, vol. 95, no. 6, pp. 1777–1792, 2012.

[77] Y. He, B. Bahr, M. Si, P. Ye, and D. Weinstein, “A tunable ferroelectric based unreleased RF resonator,” *Microsystems Nanoeng.*, vol. 6, no. 1, pp. 1–7, Dec. 2020.

[78] Y. He, B. Bahr, M. Si, P. Ye, and D. Weinstein, “Switchable Mechanical Resonance Induced by Hysteretic Piezoelectricity in Ferroelectric Capacitors,” *2019 20th Int. Conf. Solid-State Sensors, Actuators Microsystems Eurosensors XXXIII (TRANSDUCERS EUROSENSORS XXXIII)*, no. June, pp. 717–720, 2019.

[79] T. S. T. Moise *et al.*, “Demonstration of a 4Mb, High Density Ferroelectric Memory Embedded within a 130nm, 5LM Cu/FSG Logic Process,” *Tech. Dig. - Int. Electron Devices Meet.*, pp. 535–538, 1850.

[80] K. R. Udayakumar *et al.*, “Manufacturable high-density 8 Mbit one transistor-one capacitor embedded ferroelectric random access memory,” *Jpn. J. Appl. Phys.*, vol. 47, no. 4 PART 2, pp. 2710–2713, 2008.

[81] J. D. Larson, P. D. Bradley, S. Wartenberg, and R. C. Ruby, “Modified Butterworth-Van Dyke circuit for FBAR resonators and automated measurement system,” *Proc. IEEE Ultrason. Symp.*, vol. 1, pp. 863–868, 2000.

[82] G. Piazza, P. J. Stephanou, and A. P. Al Pisano, “Piezoelectric aluminum nitride vibrating contour-mode MEMS resonators,” *J. Microelectromechanical Syst.*, vol. 15, no. 6, pp. 1406–1418, 2006.

[83] M. Schreiter, R. Gabl, D. Pitzer, R. Primig, and W. Wersing, “Electro-acoustic hysteresis behaviour of PZT thin film bulk acoustic resonators,” *J. Eur. Ceram. Soc.*, vol. 24, no. 6, pp. 1589–1592, 2004.

[84] H. Chandrahalim, S. A. Bhave, R. G. Polcawich, J. S. Pulskamp, and R. Kaul, “PZT transduced high-overtone width-extensional resonators above 1 GHz,” *Proc. - IEEE Ultrason. Symp.*, pp. 2145–2148, 2009.

[85] N. Hanajima, S. Tsutsumi, T. Yonezawa, K. Hashimoto, R. Nanjo, and M. Yamaguchi, “Ultrasonic properties of lead zirconate titanate thin films in UHF-SHF range,” *Jpn. J. Appl. Phys.*, vol. 36, no. 9S, p. 6069, 1997.

[86] R. Baldemair *et al.*, “Future wireless communications,” *IEEE Veh. Technol. Conf.*, 2013.

[87] L. C. Popa and D. Weinstein, “Switchable piezoelectric transduction in AlGaN/GaN MEMS resonators,” *2013 Transducers Eurosensors XXVII 17th Int. Conf. Solid-State Sensors, Actuators Microsystems, TRANSDUCERS EUROSENSORS 2013*, pp. 2461–2464, 2013.

[88] Wei Pang, Hao Zhang, Hongyu Yu, and Eun Sok Kim, “Electrically tunable and switchable film bulk acousitc resonator,” *Proc. 2004 IEEE Int. Freq. Control Symp. Expo. 2004.*, vol. 00, no. c, pp. 22–26, 2005.

[89] G. N. Saddik, D. S. Boescht, S. Stemmert, and R. A. York, “Strontium Titanate DC Electric Field Switchable and Tunable Bulk Acoustic Wave Solidly Mounted Resonator,” *Nonlinearity*, vol. 93106, pp. 1263–1266, 2008.

[90] X. Zhu, J. D. Phillips, and A. Mortazawi, “A DC voltage dependant switchable thin film bulk wave acoustic resonator using ferroelectric thin film,” *IEEE MTT-S Int. Microw. Symp. Dig.*, pp. 671–674, 2007.

[91] H. Takasu, “The ferroelectric memory and its application,” *j. Electroceram*, vol. 4, pp. 327–338, 2000.

[92] D. Damjanovic, “Hysteresis in piezoelectric and ferroelectric materials,” in *The Science of Hysteresis*, 2006.

[93] Y. He, B. Bahr, and D. Weinstein, “a Ferroelectric Capacitor (Fecap) Based Unreleased Resonator,” in *Solid-State Sensors, Actuators, and Microsystems Workshop*, 2018, vol. 4, no. 2008, pp. 5–6.

[94] S. S. Bedair *et al.*, “High rejection, tunable parallel resonance in micromachined lead zirconate titanate on silicon resonators,” *Appl. Phys. Lett.*, vol. 99, no. 10, pp. 10–12, 2011.

[95] W. S. Gan, *New acoustics based on metamaterial*, vol. 15. 2012.

[96] L. Fok, M. Ambati, and X. Zhang, "Acoustic Metamaterials," *MRS Bull.*, vol. 33, no. October, pp. 7–9, 2008.

[97] P. A. Deymier, *Acoustic Metamaterials and Phononic Crystals*. Springer, 2013.

[98] E. N. Economou and M. M. Sigalas, "Classical Wave Propagation In Periodic Structures: Cermet Versus Network Topology," *Phys. Rev. B*, vol. 48, no. 18, pp. 13434–13438, 1993.

[99] Martínez-Sala, J. S. Rosa, J. V. Sánchez, V. Gómez, J. Llinares, and F. Meseguer, "Sound Attenuation by Sculpture," *Nature*, vol. 378, no. November, p. 241, 1995.

[100] M. I. Hussein, M. J. Leamy, and M. Ruzzene, "Dynamics of phononic materials and structures: Historical origins, recent progress, and future outlook," *Appl. Mech. Rev.*, vol. 66, no. 4, 2014.

[101] M. I. Hussein, M. J. Leamy, and M. Ruzzene, "Dynamics of phononic materials and structures: Historical origins, recent progress, and future outlook," *Appl. Mech. Rev.*, vol. 66, no. 4, pp. 1–38, 2014.

[102] S. Chen *et al.*, "A Review of Tunable Acoustic Metamaterials," *Appl. Sci.*, vol. 8, no. 9, p. 1480, 2018.

[103] Z. Liu *et al.*, "Locally resonant sonic materials," *Science (80-.).*, vol. 289, no. 5485, pp. 1734–1736, 2000.

[104] J. Galipeau and R. E. Chang, "Design considerations for high power BAW duplexers for base station applications," *2015 IEEE Int. Ultrason. Symp. IUS 2015*, pp. 34–37, 2015.

[105] E. T. T. Yen *et al.*, "Integrated High-frequency Reference Clock Systems Utilizing Mirror-encapsulated BAW Resonators," *IEEE Int. Ultrason. Symp. IUS*, vol. 2019-Octob, pp. 2174–2177, 2019.

[106] F. Z. Bi and B. P. Barber, "Bulk Acoustic Wave RF Technology," *IEEE Microw. Mag.*, no. October, pp. 65–80, 2008.

[107] I. A. Veres, T. Berer, R. Rothemund, and A. Tajic, "Finite Element Analysis of BAW resonators: A matter of model dimensionality?," *IEEE Int. Ultrason. Symp. IUS*, vol. 2019-Octob, pp. 1711–1713, 2019.

[108] R. K. Thalhammer and J. D. Larson, "Finite-Element Analysis of Bulk-Acoustic-Wave Devices: A Review of Model Setup and Applications," *IEEE Trans. Ultrason. Ferroelectr. Freq. Control*, vol. 63, no. 10, pp. 1624–1635, 2016.

[109] S. Mahon, "The 5G Effect on RF Filter Technologies," *IEEE Trans. Semicond. Manuf.*, vol. 30, no. 4, pp. 494–499, 2017.

[110] S. Wang, L. C. Popa, and D. Weinstein, "GaN MEMS resonator using a folded phononic crystal structure," in *Solid-State Sensors, Actuators, and Microsystems Workshop*, 2014, pp. 72–75.

[111] S. Wang, L. C. Popa, and D. Weinstein, "Tapered Phononic Crystal saw resonator in GaN," *Proc. IEEE Int. Conf. Micro Electro Mech. Syst.*, vol. 2015-Febru, no. February, pp. 1028–1031, 2015.

[112] R. Lu, T. Manzaneque, Y. Yang, and S. Gong, "Lithium Niobate Phononic Crystals for Tailoring Performance of RF Laterally Vibrating Devices," *IEEE Trans. Ultrason. Ferroelectr. Freq. Control*, vol. 65, no. 6, pp. 934–944, 2018.

[113] G. Wu, Y. Zhu, S. Merugu, N. Wang, C. Sun, and Y. Gu, "GHz spurious mode free AlN lamb wave resonator with high figure of merit using one dimensional phononic crystal tethers," *Appl. Phys. Lett.*, vol. 109, no. 1, pp. 1–5, 2016.

[114] L. Binci, C. Tu, H. Zhu, and J. E. Y. Lee, "Planar ring-shaped phononic crystal anchoring boundaries for enhancing the quality factor of Lamb mode resonators," *Appl. Phys. Lett.*, vol. 109, no. 20, Nov. 2016.

[115] H. Zhu and J. E. Y. Lee, "AlN piezoelectric on silicon MEMS resonator with boosted Q using planar patterned phononic crystals on anchors," *Proc. IEEE Int. Conf. Micro Electro Mech. Syst.*, vol. 2015-Febru, no. February, pp. 797–800, 2015.

[116] M. W. U. Siddiqi and J. E. Y. Lee, "AlN-on-Si MEMS resonator bounded by wide acoustic bandgap two-dimensional phononic crystal anchors," *Proc. IEEE Int. Conf. Micro Electro Mech. Syst.*, vol. 2018-Janua, no. January, pp. 727–730, 2018.

[117] Y. Y. Chen, Y. R. Lin, T. T. Wu, and S. Y. Pao, "Anchor loss reduction of quartz resonators utilizing phononic crystals," *2015 IEEE Int. Ultrason. Symp. IUS 2015*, pp. 1–4, Nov. 2015.

[118] W. Jiang, D. Feng, D. Xu, B. Xiong, and Y. Wang, "Experimental investigation of energy localization in line-defect resonator based on silicon locally resonant phononic crystal," *Appl. Phys. Lett.*, vol. 109, no. 16, 2016.

[119] N. Wang, F. L. Hsiao, J. M. Tsai, M. Palaniapan, D. L. Kwong, and C. Lee, "Numerical and experimental study on silicon microresonators based on phononic crystal slabs with reduced central-hole radii," *J. Micromechanics Microengineering*, vol. 23, no. 6, Jun. 2013.

[120] M. Moutaouekkil *et al.*, "Highly confined radial contour modes in phononic crystal plate based on pillars with cap layers," *J. Appl. Phys.*, vol. 126, no. 5, 2019.

[121] J. Liu, H. Guo, and T. Wang, "A Review of Acoustic Metamaterials and Phononic Crystals," *Crystals*, vol. 10, no. 305, 2020.

[122] H. Ge *et al.*, "Breaking the barriers: Advances in acoustic functional materials," *Natl. Sci. Rev.*, vol. 5, no. 2, pp. 159–182, 2018.

[123] Y. F. Wang, Y. Z. Wang, B. Wu, W. Chen, and Y. S. Wang, "Tunable and Active Phononic Crystals and Metamaterials," *Appl. Mech. Rev.*, vol. 72, no. 4, 2020.

[124]S. A. Cummer, J. Christensen, and A. Alù, "Controlling sound with acoustic metamaterials," *Nat. Rev. Mater.*, vol. 1, no. 16001, Feb. 2016.

[125] P. Mihas, "Developing ideas of refraction, lenses and rainbow through the use of historical resources," *Sci. Educ.*, vol. 17, no. 7, pp. 751–777, 2008.

[126] Z. Liang and J. Li, "Extreme acoustic metamaterial by coiling up space," *Phys. Rev. Lett.*, vol. 108, no. 11, Mar. 2012.

[127] C. Cro *et al.*, "Negative refraction of longitudinal waves in a two-dimensional solid-solid phononic crystal," *Phys. Rev. B - Condens. Matter Mater. Phys.*, vol. 83, no. 5, pp. 3–7, Feb. 2011.

[128] B. Morvan, A. Tinel, A. C. Hladky-Hennion, J. Vasseur, and B. Dubus, "Experimental demonstration of the negative refraction of a transverse elastic wave in a two-dimensional solid phononic crystal," *Appl. Phys. Lett.*, vol. 96, no. 10, pp. 10–13, 2010.

[129] X. Zhang and Z. Liu, "Negative refraction of acoustic waves in two-dimensional phononic crystals," *Appl. Phys. Lett.*, vol. 85, no. 2, pp. 341–343, Jul. 2004.

[130] R. Zhu, X. N. Liu, G. K. Hu, C. T. Sun, and G. L. Huang, "Negative refraction of elastic waves at the deep-subwavelength scale in a single-phase metamaterial," *Nat. Commun.*, vol. 5, no. May, pp. 1–8, 2014.

[131] J. Bucay *et al.*, "Positive, negative, zero refraction, and beam splitting in a solid/air phononic crystal: Theoretical and experimental study," *Phys. Rev. B - Condens. Matter Mater. Phys.*, vol. 79, no. 21, pp. 1–7, 2009.

[132] L. Feng *et al.*, "Refraction control of acoustic waves in a square-rod-constructed tunable sonic crystal," *Phys. Rev. B - Condens. Matter Mater. Phys.*, vol. 73, no. 19, pp. 2–5, 2006.

[133] Z. Chen, B. Guo, Y. Yang, and C. Cheng, "Metamaterials-based enhanced energy harvesting: A review," *Phys. B Condens. Matter*, vol. 438, pp. 1–8, 2014.

[134] N. K. Kuo and G. Piazza, "Fractal phononic crystals in aluminum nitride: An approach to ultra high frequency bandgaps," *Appl. Phys. Lett.*, vol. 99, no. 16, pp. 2009–2012, 2011.

[135] Z. Tian *et al.*, "Dispersion tuning and route reconfiguration of acoustic waves in valley topological phononic crystals," *Nat. Commun.*, vol. 11, no. 1, pp. 1–10, Dec. 2020.

[136] H. Zhu and F. Semperlotti, "Double-Zero-Index Structural Phononic Waveguides," *Phys. Rev. Appl.*, vol. 8, no. 6, pp. 1–11, 2017.

[137] R. Kumar, D. Das, E. Muñoz, and A. K. Singh, "Critical Sublattice Symmetry Breaking: A Universal Criterion for Dirac Cone Splitting," *J. Phys. Chem. C*, vol. 123, no. 37, pp. 23082–23088, 2019.

[138] H. Chen and C. T. Chan, "Acoustic cloaking and transformation acoustics," *J. Phys. D. Appl. Phys.*, vol. 43, no. 11, 2010.

[139] J. Lu, C. Qiu, M. Ke, and Z. Liu, "Valley Vortex States in Sonic Crystals," *Phys. Rev. Lett.*, vol. 116, no. 9, pp. 1–6, Feb. 2016.

[140] V. Peri *et al.*, "Experimental characterization of fragile topology in an acoustic metamaterial," *Science (80-.).*, vol. 367, no. 6479, pp. 797–800, 2020.

[141] B. I. Popa, L. Zigoneanu, and S. A. Cummer, "Experimental acoustic ground cloak in air," *Phys. Rev. Lett.*, vol. 106, no. 25, pp. 1–4, 2011.

[142] S. Zhang, C. Xia, and N. Fang, "Broadband acoustic cloak for ultrasound waves," *Phys. Rev. Lett.*, vol. 106, no. 2, pp. 1–4, 2011.

[143] J. Lu *et al.*, "Observation of topological valley transport of sound in sonic crystals," *Nat. Phys.*, vol. 13, no. 4, pp. 369–374, 2017.

[144] M. Weiner, X. Ni, M. Li, A. Alù, and A. B. Khanikaev, "Demonstration of a third-order hierarchy of topological states in a three-dimensional acoustic metamaterial," *Sci. Adv.*, vol. 6, no. 13, p. eaay4166, 2020.

[145] Y. He, B. Bahr, M. Si, P. Ye, and D. Weinstein, "A tunable ferroelectric based unreleased RF resonator," *Microsystems Nanoeng.*, vol. 6, no. 1, Dec. 2020.

[146] A. Sukhovich *et al.*, "Experimental and theoretical evidence for subwavelength imaging in phononic crystals," *Phys. Rev. Lett.*, vol. 102, no. 15, pp. 1–4, Apr. 2009.

[147] N. Kaina, F. Lemoult, M. Fink, and G. Lerosey, “Negative refractive index and acoustic superlens from multiple scattering in single negative metamaterials,” *Nature*, vol. 525, no. 7567, pp. 77–81, Sep. 2015.

[148] Y. Ding, Z. Liu, C. Qiu, and J. Shi, “Metamaterial with simultaneously negative bulk modulus and mass density,” *Phys. Rev. Lett.*, vol. 99, no. 9, Aug. 2007.

[149] C. Coulais, D. Sounas, and A. Alù, “Static non-reciprocity in mechanical metamaterials,” *Nature*, vol. 542, no. 7642, pp. 461–464, 2017.

[150] X. Ao and C. T. Chan, “Far-field image magnification for acoustic waves using anisotropic acoustic metamaterials,” *Phys. Rev. E - Stat. Nonlinear, Soft Matter Phys.*, vol. 77, no. 2, pp. 1–4, Feb. 2008.

[151] S. Yang, J. H. Page, Z. Liu, M. L. Cowan, C. T. Chan, and P. Sheng, “Focusing of Sound in a 3D Phononic Crystal,” *Phys. Rev. Lett.*, vol. 93, no. 2, pp. 2–5, 2004.

[152] A. Sukhovich, L. Jing, and J. H. Page, “Negative refraction and focusing of ultrasound in two-dimensional phononic crystals,” *Phys. Rev. B - Condens. Matter Mater. Phys.*, vol. 77, no. 1, pp. 1–9, Jan. 2008.

[153] Y. Ding, Z. Liu, C. Qiu, and J. Shi, “Metamaterial with simultaneously negative bulk modulus and mass density,” *Phys. Rev. Lett.*, vol. 99, no. 9, pp. 2–5, Aug. 2007.

[154] H. He *et al.*, “Topological negative refraction of surface acoustic waves in a Weyl phononic crystal,” *Nature*, vol. 560, no. 7716. Nature Publishing Group, pp. 61–64, 02-Aug-2018.

[155] M. Chen, H. Jiang, H. Zhang, D. Li, and Y. Wang, “Design of an acoustic superlens using single-phase metamaterials with a star-shaped lattice structure,” *Sci. Rep.*, vol. 8, no. 1, pp. 2–9, 2018.

[156] Y. Guo, D. Brick, M. Großmann, M. Hettich, and T. Dekorsy, “Acoustic beam splitting at low GHz frequencies in a defect-free phononic crystal,” *Appl. Phys. Lett.*, vol. 110, no. 3, pp. 1–5, Jan. 2017.

[157] J. Müller *et al.*, “Ferroelectricity in HfO2enables nonvolatile data storage in 28 nm HKMG,” in *Digest of Technical Papers - Symposium on VLSI Technology*, 2012, pp. 25–26.

VITA

Yanbo He was born on July 18th, 1992 in Deyang, China. He received his Bachelor of Science degree in Thermal Energy and Power Engineering from Harbin Engineering University, then moved to the University of Pittsburgh, where he completed his Master of Science in Mechanical Engineering. In 2016, he joined the school of Electrical and Computer Engineering at Purdue University for his Ph.D. study.